DEVELOPMENT OF A NEAR-FIELD MICROWAVE IMAGING SYSTEM

By

DENYS S. SHUMAKOV, M.Sc, B.Sc.

A Thesis

Submitted to the School of Graduate Studies

in Partial Fulfillment of the Requirements

of the Degree

Doctor of Philosophy

McMaster University

DOCTOR OF PHILOSOPHY (2017) McMaster University

(Electrical and Computer Engineering) Hamilton, Ontario

TITLE: Development of a Near-Field Microwave Imaging System

AUTHOR: Denys S. Shumakov, M.Sc. (National Technical University of Ukraine), B.Sc. (National Technical University of Ukraine)

SUPERVISOR: Natalia K. Nikolova, Professor

CO-SUPERVISOR: John W. Bandler, Professor Emeritus

NUMBER OF PAGES: CLXXXVI, 186

ABSTRACT

This thesis presents the results of an ongoing development of a near-field microwave imaging system. The thesis mainly focuses on the image reconstruction algorithms and data processing. Two linear-inversion methods, block circulant with circulant blocks (BCCB) scattered-power mapping (SPM) and convolution-based SPM, have been proposed. Both methods are general and efficient in solving the linear inverse problem. The images are reconstructed in quasi-real time with the BCCB SPM and in real time with the convolution-based SPM. A new method of building the SPM system matrix formed by the calibration object power maps is proposed. It allows for a reduced number of calibration measurements. BCCB SPM and convolution-based SPM are intended as a tool to solve weak-scattering problems or as a linear-inversion module within nonlinear iterative reconstruction.

An algorithm has been developed for the de-noising of *S*-parameter data used in microwave imaging. It enables the efficient estimation of the noise-free signal component and its separation from the noise component in 2D-scan data sets. The proposed algorithm offers several benefits in imaging. First, it can suppress noise and uncertainties in the data used as input to the reconstruction algorithms. Such noise and uncertainties lead to image artifacts and errors. Second, the condition number of the BCCB system matrix improves as a result of the de-noising preprocessing of the raw data. The algorithm can also be used to quantify the imaging system's dynamic range. Finally, it allows estimating the signal-to-noise ratio of a particular data set.

Another development is concerned with a novel calibration strategy for near-field quantitative linear-inversion methods. It employs a metallic scattering probe embedded in the background. The biggest advantage of the calibration with metallic scattering probe is the target-independent quantitative accuracy. Also, full polarimetric information about the incident field can be readily obtained.

An axial-null illumination has also been proposed to simplify the calibration of microwave imaging systems. Such illumination also enhances the spatial resolution. It can be achieved with various array configurations but a minimum of two transmitting antennas are required. Due to the intrinsic antisymmetry of the axial-null illumination, the baseline signals are suppressed down to the noise level of the measurement system. Therefore, the most important advantage of the proposed imaging setup is that it eliminates the need for background (or baseline) measurements. The discussed improvements are expected to occur for any imaging technique that exploits wave-like physical fields.

ACKNOWLEDGEMENTS

During the course of my PhD studies at McMaster University, I have benefited greatly from the assistance and support of many people to whom I am deeply indebted.

I am sincerely thankful to my supervisor, Dr. Natalia Nikolova, who believed in my potential and invited me to join her research group. Her invaluable guidance and support throughout all years of the PhD research made this thesis possible. Commitment to research, communication skills, problem-solving strategies and easy-going attitude to life are some of the things I was able to learn from Dr. Natalia Nikolova.

I would like to express my deep appreciation to Dr. John Bandler for many informative discussions, suggestions and advice on professional development. During the summer of 2015 we collaborated closely on further developing interactive “games” based on aggressive space mapping. This was a memorable experience of working with a multidisciplinary team.

Dr. Mohamed Bakr and Dr. Aleksandar Jeremic deserve special mention for their excellent work in teaching the graduate courses which proved to be extremely valuable for my research.

At last but not least, I would like to thank all my friends including Justin McCombe, Alexander Beaverstone and Daniel Tajik who have made my time in the office an enjoyable experience.

DEVELOPMENT OF A NEAR-FIELD MICROWAVE IMAGING SYSTEM

Contents

List of Figures

List of Acronyms

2D	Two Dimensional
3D	Three Dimensional
ANI	Axial-Null Illumination
BCCB	Block Circulant with Circulant Blocks
CO	Calibration Object
CSI	Contrast Source Inversion
EM	Electromagnetic
FFT	Fast Fourier Transform
GPS	Global Positioning System
LQL	Localized Quasi-Linear
LQLR	Localized Quasi-Linear Rytov
NSA	Null Steering Antennas
OUT	Object Under Test
PSF	Point-Spread Function
RO	Reference Object
SNR	Signal-to-Noise Ratio
SPM	Scattered-Power Mapping
TEM	Transverse Electromagnetic
UWB	Ultra-Wide Band
VNA	Vector Network Analyzer

Chapter 1

Introduction

1.1 Background

Microwave imaging is at the center of attention for many researchers around the world. It has a wide breadth of short-range applications in areas such as through-the-wall imaging [1], concealed weapon detection [2][3], non-destructive testing and evaluation [4][5] and biomedical imaging [6]. Within biomedical imaging, early-stage breast cancer detection has gained much attention [7]. Microwaves are nonionizing and they can be emitted and received with relatively cheap and compact components. However, when it comes to microwave tissue imaging, fundamental problems such as penetration depth, coupling power into the tissue, resolution limits, tissue heterogeneity, etc., impose a significant challenge to the progress toward commercial and clinical applications [8].

Microwave imaging aims at reconstructing the electrical and magnetic properties of objects as functions of position. Qualitative approaches produce the location and shape of objects which exhibit property contrast with respect to the background medium. The quantitative approaches, on the other hand, yield an estimate of the target's electrical properties at each spatial point. Qualitative methods are widely used for detection of abnormalities even though there is no quantitative feedback. These methods often employ

a linearized model of scattering allowing for quick inversion. Thus, an image is reconstructed practically in real time. However, the results may not be satisfactory if the linearized forward model is an inadequate representation of the actual scattering processes. Qualitative methods include holographic [9]-[12], sensitivity-based [13][14], confocal [15]-[17], time-reversal [18][19] methods, and others.

Quantitative techniques that are widely used in microwave imaging are the Born iterative methods [20]-[22], the stochastic optimization methods [23]-[25] and the deterministic iterative procedures [26]-[28]. These methods explicitly (or implicitly) update the forward model in an iterative manner to match the measured data. The quantitative reconstruction solves the nonlinear scattering problem which takes into account multiple-scattering effects and is valid for scatterers of any electrical size and dielectric contrast. The inverse-scattering problem is intrinsically ill-posed and is tackled by time-consuming iteration loops aided by appropriate regularization strategies. The convergence of the quantitative methods depends critically on the fidelity of the forward model.

In microwave imaging, the scanning hardware usually employs acquisition surfaces of canonical shapes: planar, cylindrical, or hemispherical, which simplifies the reconstruction process. The data (back-scattered and/or forward-scattered signals) can be acquired either through mechanical scanning or through electronically-switched arrays. The transmitting antennas are designed to conform to the respective surface shape and to have the radiation maximum more or less along boresight and aiming at the center of the examined volume. This design choice achieves stronger scattering signals from possible

targets – the stronger the illumination is, the stronger the scattered field. Further, in forward-scattered (transmission coefficient) data acquisition, it is customary to align at least one of the receiving antennas (the sensors) along the transmitters' boresight in order to minimize the signal path, thereby maximizing the signal strength. In back-scattered (reflection coefficient) data acquisition, it is customary to use the same antenna as a transmitter and a receiver along with a duplexing device that separates the incoming (reflected) signal from the outgoing (transmitted) one.

Multi-illumination configurations, also known as illumination-diversity techniques, have been used widely in microwave imaging [17][27][29]-[32]. At the expense of increased hardware complexity, such configurations allow for more accurate target shape reconstruction and localization. This is a consequence of collecting data from multiple perspectives. Illumination diversity along with frequency diversity can drastically improve the performance of microwave imaging provided the design of the system is optimal.

The physical assessment of the imaging system aims at determining the quality of the data before they are processed to produce an image. The raw-data quality is critical for the final image fidelity and it can be assessed independently from the reconstruction. The medical imaging community has adopted objective metrics unified across various modalities [33]-[35]. The metrics for the physical assessment of microwave and millimeter-wave imaging systems exist but there appears to be no unified system of definitions and assessment methods.

1.2 Motivation

Recently, a method has been proposed offering the benefits of both quantitative reconstruction and fast performance, while not being nonlinear and/or iterative [36][37]. The key lies in the experimentally acquired resolvent kernel which properly scales the inversion problem thereby enabling quantitative imaging. Similar to other direct-inversion methods, the applicability of the work in [36] and [37] is rather limited since its forward model is linearized with the Born model of scattering. It is well known that the Rytov approximation outperforms Born approximation when electrically large low-contrast objects are imaged since the accuracy of the Rytov approximation does not depend on the scatterer's size [38][39]. Therefore, employing the linear Rytov model in addition to also being capable of employing the linear Born model would significantly expand the method's applicability.

In [36] and [37], calibration measurements are used to quantify the resolvent kernel, thus providing a high-fidelity forward model. For that, the calibration object, or CO has to be scanned. The CO response constitutes a point-spread function (PSF) which in turn provides the respective resolvent kernel of the data equation. By definition, the calibration object is comprised of a scattering probe embedded in the background medium. For the case of planar acquisition surfaces and when the background is homogeneous or layered (translationally-invariant systems), it is required to have a four-time larger scanning area for the CO measurement as per [36] or [37]. Also, for accurate quantitative results, the relative permittivity of a voxel in the inspected object must be close to that of the

dielectric scattering probe of the CO [36][37]. Since the permittivity of the scattering probe is fixed, the quantitative reconstruction of objects with widely varying permittivity distribution, such as living tissue, is not likely to be accurate. Consequently, a four-time larger scanning area for the CO measurement and a fixed permittivity of the dielectric scattering probe make the system-calibration time-consuming.

Another important part of the microwave system calibration is concerned with background de-embedding. In both transmission and reflection measurements, the single-source illumination scheme results in relatively strong received signals even when the scatterer-free background is measured. These signals are referred to as the baseline signals, which are representative of the incident-field component in the scattering equations. The simplest approach to background de-embedding is based on the assumption that the mutual coupling between the acquisition hardware and the target can be neglected and the signal of the object under test is simply a superposition of the baseline and the scattered signals [10][36][37]. Two main problems ensue due to the need to estimate the baseline signal. First, the respective calibration measurements are needed – often performed before each measurement of an object under test. Second, the baseline signal contains systematic and stochastic noise as well as positioning uncertainties at levels comparable to those contained in the signal of the object under test. Provided the baseline measurement is performed under exactly the same circumstances as those of the object under test – a challenging requirement on its own – the systematic errors should cancel. Unfortunately, stochastic noise and uncertainties in the positioning do not cancel.

In signal processing, the extraction of the signal from noisy data is a long-standing problem [40]-[42]. The signals are usually dependent on a single variable, e.g., time. In the case of microwave imaging, raw frequency-sweep data are usually comprised of *S*-parameters that depend on the frequency and the sampling location, e.g., (x, y) in planar scanning. Also, the *S*-parameters are complex. Separating the signal from the noise and positioning uncertainties in complex-valued 2D data at each sampled frequency would be beneficial in image reconstruction [6][43] minimising the need to employ case-specific filtering and regularization.

1.3 Contributions

The author has contributed to the development of a near-field microwave imaging system in the following ways:

a) Developed two linear-inversion methods, block circulant with circulant blocks (BCCB) scattered-power mapping (SPM) and convolution-based SPM, reconstructing images in quasi-real time and in real time, respectively. Both methods exploit the key idea of the work in [36], but are more general and far more efficient in solving the linear inverse problem. Also, a reduced number of calibration measurements are required in comparison with the previous work. The methods are intended as a tool to solve weak-scattering problems or as a linear-inversion module within nonlinear iterative reconstruction.

b) Developed an axial-null illumination (ANI) to simplify the calibration of microwave imaging systems. Such illumination also enhances the spatial

resolution. It can be achieved with various array configurations but a minimum of two transmitting antennas are required, which is a well-known form of differential illumination. The most important advantage of the proposed imaging setup is that it eliminates the need for background (or baseline) measurements.

c) Developed a novel calibration strategy for near-field quantitative linear-inversion methods. It employs a metallic scattering probe embedded in the background. The advantages include an ability to obtain full polarimetric information as well as a target-independent quantitative accuracy. The proposed calibration strategy uses an *S*-parameter model of scattering reported in [45].

d) Developed an algorithm for the de-noising of *S*-parameter data used in microwave imaging. The complex *S*-parameter frequency-sweep data are collected through scans over an acquisition surface and the algorithm separates efficiently the resultant 2D responses (one frequency at a time) into a signal and a noise component. No a priori knowledge of the scanned object is required. The signal component estimates the noise-free data whereas the remaining data content estimates the noise and uncertainty in the measurement. The algorithm can also be used to quantify the imaging system's dynamic range and to estimate the signal-to-noise ratio (SNR) of a particular data set.

Parts of this work have been published in [36][44]-[48].

1.4 Outline of the Thesis

This thesis presents the results of an ongoing development of a near-field microwave imaging system. The thesis mainly focuses on the image reconstruction algorithms and data processing. Special attention is paid to such aspects of the electromagnetic (EM) inverse scattering theory as the forward model formulation, the resolvent kernel in the integral equation of scattering as well as the Born and Rytov scalar models of scattering. In terms of the hardware part, the multi-illumination schemes along with spatial resolution limits are studied in order to propose optimal illumination schemes for near-field microwave imaging. Calibration of the near-field microwave imaging systems is discussed as well, with a novel calibration strategy for the quantitative imaging being proposed.

Chapter 2 introduces the data equation of EM scattering cast in the form of *S*-parameter responses. The data equation is central to the developments in the subsequent chapters as it serves as the forward model, on which the direct inversion methods are based. This is followed by a discussion of the different strategies for the estimation of the resolvent kernel in the forward model of scattering. In addition to the well-known calibration with a dielectric scattering probe, a novel calibration with a metallic scattering probe for near-field quantitative imaging is introduced. The chapter ends with a detailed discussion of the linearized forward models of scattering used in this thesis.

Chapter 3 is dedicated to the reconstruction theory of two linear inversion methods, BCCB SPM and convolution-based SPM, as applied to the frequency-domain measurement data. Both qualitative and quantitative reconstruction is discussed. A new method of building the SPM system matrix formed by the CO power maps is proposed.

For the case of planar acquisition surfaces and when the background is homogeneous or layered (translationally-invariant systems), the coordinate translation in Fourier space is presented. It leads to the system matrix being BCCB in the case of 2D imaging or block circulant with BCCB blocks in 3D imaging. Pros and cons of the proposed linear inversion methods are discussed in detail.

Chapter 4 presents the de-noising algorithm for enhancing microwave imaging. The extraction of the signal from noisy data is performed with an iterative procedure similar to the empirical mode decomposition. The algorithm's description is followed by the validation examples. De-noising raw data before reconstruction and quantifying the performance of an acquisition system are two possible applications of the algorithm in microwave imaging.

In Chapter 5, SPM validation examples are presented. Both the 2D and 3D imaging cases are considered with the calibration strategies employing a dielectric scattering probe and a metallic scattering probe. The apodization function applied in the real space as a pre-processing step is studied. It is also shown that the reconstruction fidelity improves when the de-noising algorithm is applied to the raw data.

Chapter 6 is concerned with illumination-diversity techniques widely used in microwave imaging. This chapter starts with the presentation of a rigorous theory of the spatial resolution in the case of multi-illumination schemes. The cross-range resolution limits with planar scanning are derived analytically in the far zone allowing for a comparison between the conventional single-source illumination and the double-source

illumination. Next, the ANI for near-field microwave imaging is introduced. In addition to the improved cross-range resolution, the proposed illumination scheme simplifies the imaging system calibration.

The concluding Chapter 7 reviews the main points of the thesis and elaborates on the importance of the proposed work. Recommendations for future research are discussed as well.

References

[1] M. G. Amin. *Through-the-Wall Radar Imaging*. Boca Raton, FL: CRC Press, 2011.

[2] J. Nanzer. *Microwave and Millimeter-wave Remote Sensing for Security Applications*. Norwood, MA: Artech House, 2012.

[3] D. J. Daniels, *EM Detection of Concealed Targets*. Hoboken, NJ: Wiley-IEEE Press, 2009.

[4] R. Zoughi. *Microwave Non-destructive Testing and Evaluation*. Dordrecht, The Netherlands: Kluwer Academic, 2000.

[5] D. M. Sheen, D. L. McMakin, and T. E. Hall, "Near-field three-dimensional radar imaging techniques and applications," *Applied Optics*, vol. 49, no. 19, pp. E83–E93, July 2010.

[6] N. K. Nikolova, "Microwave biomedical imaging," *Wiley Encyclopedia of Electrical and Electronics Engineering*, pp. 1–22. (published online Apr. 25, 2014).

[7] A. Rosen, M. A. Stuchly, and A. V. Vorst, "Applications of RF/microwaves in medicine," *IEEE Trans. Microw. Theory Techn.*, vol. 50, no. 3, pp. 963–974, Mar. 2002.

[8] A. V. Vorst, A. Rosen, and Y. Kotsuka. *RF/Microwave Interaction with Biological Tissues*. Hoboken, NJ: Wiley, 2006.

[9] M. Ravan, R. K. Amineh, and N. K. Nikolova, "Two-dimensional near-field microwave holography," *Inverse Problems*, vol. 26, no. 5, 055011, 21 pp., Apr. 2010.

[10] R. K. Amineh, A. Khalatpour, H. Xu, Y. Baskharoun, and N. K. Nikolova, "Three-dimensional near-field microwave holography for tissue imaging," *Int. J. Biomed. Imaging*, vol. 2012, Article ID 291494, 11 pp., 2012.

[11] M. Elsdon, D. Smith, M. Leach, and S. J. Foti, "Experimental investigation of breast tumor imaging using indirect microwave holography," *Microw. Opt. Technol. Lett*., vol. 48, pp. 480–482, Jan. 2006.

[12] D. M. Sheen, D. L. McMakin, and T. E. Hall, "Three-dimensional millimeter-wave imaging for concealed weapon detection," *IEEE Trans. Microw. Theory Techn.*, vol. 49, no. 9, pp. 1581–1592, Sep. 2001.

[13] L. Liu, A. Trehan, and N. K. Nikolova, "Near-field detection at microwave frequencies based on self-adjoint response sensitivity analysis," *Inverse Problems*, vol. 26, no. 10, 105001, 28 pp., Aug. 2010.

[14] Y. Zhang, S. Tu, R. K. Amineh, and N. K. Nikolova, "Resolution and robustness to noise of the sensitivity-based method for microwave imaging with data acquired on cylindrical surfaces," *Inverse Problems*, vol. 28, no. 11, 115006, 15 pp., Oct. 2012.

[15] E. C. Fear, X. Li, S. C. Hagness, and M. A. Stuchly, "Confocal microwave imaging for breast cancer detection: localization of tumors in three dimensions," *IEEE Trans. Biomed. Eng.*, vol. 49, no. 8, pp. 812–822, Aug. 2002.

[16] H. B. Lim, N. T. T. Nhung, E. P. Li, and N. D. Thang, "Confocal microwave imaging for breast cancer detection: delay-multiply-and-sum image reconstruction algorithm," *IEEE Trans. Biomed. Eng.*, vol. 55, no. 6, pp. 1697–1704, Jun. 2008.

[17] P. M. Meaney, M. W. Fanning, D. Li, S. P. Poplack, and K. D. Paulsen, "A clinical prototype for active microwave imaging of the breast," *IEEE Trans. Microw. Theory Techn.*, vol. 48, no. 11, pp. 1841–1853, Nov. 2000.

[18] P. Kosmas and C. M. Rappaport, "Time reversal with the FDTD method for microwave breast cancer detection," *IEEE Trans. Microw. Theory Techn.*, vol. 53, no. 7, pp. 2317–2323, Jul. 2005.

[19] A. J. Devaney, *Mathematical Foundations of Imaging, Tomography and Wavefield Inversion*. Cambridge, UK: Cambridge University Press, 2012.

[20] W. C. Chew and Y. M. Wang, "Reconstruction of two-dimensional permittivity distribution using the distorted Born iterative method," *IEEE Trans. Med. Imag.*, vol. 9, no. 2, pp. 218–225, Jun. 1990.

[21] T. J. Cui, W. C. Chew, A. A. Aydiner, and S. Chen, "Inverse scattering of two-dimensional dielectric objects buried in lossy earth using the distorted Born iterative method," *IEEE Trans. Geosci. Remote Sens.*, vol. 39, no. 2, pp. 339–346, Feb. 2001.

[22] A. G. Tijhuis, K. Belkebir, A. C. S. Litman, and B. P. de Hon, "Multiple-frequency distorted-wave Born approach to 2D inverse profiling," *Inverse Problems*, vol. 17, no. 6, pp. 1635–1644, Nov. 2001.

[23] M. Pastorino, "Stochastic optimization methods applied to microwave imaging: a review," *IEEE Trans. Antennas Propag.*, vol. 55, no. 3, pp. 538–548, Mar. 2007.

[24] P. Rocca, M. Benedetti, M. Donelli, D. Franceschini, and A. Massa, "Evolutionary optimization as applied to inverse scattering problems," *Inverse Problems*, vol. 25, no. 12, pp. 1–41, Nov. 2009.

[25] M. Donelli, G. Franceschini, A. Martini, and A. Massa, "An integrated multiscaling strategy based on a particle swarm algorithm for inverse scattering problems," *IEEE Trans. Geosci. Remote Sens.*, vol. 44, no. 2, pp. 298–312, Feb. 2006.

[26] H. Harada, D. J. N. Wall, T. Takenaka, and M. Tanaka, "Conjugate gradient method applied to inverse scattering problem," *IEEE Trans. Antennas Propag.*, vol. 43, no. 8, pp. 784–792, Aug. 1995.

[27] C. Estatico, M. Pastorino, and A. Randazzo, "An inexact-Newton method for short-range microwave imaging within the second-order Born approximation," *IEEE Trans. Geosci. Remote Sens.*, vol. 43, no. 11, pp. 2593–2605, Nov. 2005.

[28] A. Abubakar, P. M. van den Berg, and J. J. Mallorqui, "Imaging of biomedical data using a multiplicative regularized contrast source inversion method," *IEEE Trans. Microw. Theory Techn.*, vol. 50, no. 7, pp. 1761–1771, Jul. 2002.

[29] S. Caorsi, G. L. Gragnani, and M. Pastorino, "An electromagnetic approach using a multi-illumination technique," *IEEE Trans. Biomed. Eng.*, vol. 41, no. 4, pp. 406–409, Apr. 1994.

[30] C.-H. Tseng and T.-H. Chu, "Improvement of quasi-monostatic frequency-swept microwave imaging of conducting objects using illumination diversity technique," *IEEE Trans. Antennas Propag.*, vol. 53, no. 1, pp. 305–312, Jan. 2005.

[31] A. Zakaria, C. Gilmore, and J. LoVetri, "Finite-element contrast source inversion method for microwave imaging," *Inverse Problems*, vol. 26, no. 11, 115010, 21 pp., Sep. 2010.

[32] P. Mojabi, M. Ostadrahimi, L. Shafai, and J. LoVetri, "Microwave tomography techniques and algorithms: a review," *Antenna Technology and Applied Electromagnetics (ANTEM)*, pp. 1–4, Toulouse, France, Jun. 2012.

[33] R. F. Wagner and D. G. Brown, "Unified SNR analysis of medical imaging systems," *Physics in Medicine and Biology*, vol. 30, no. 6, pp. 489–518, 1985.

[34] M. Tapiovaara and R. Wagner, "SNR and noise measurements for medical imaging: I. A practical approach based on statistical decision theory," *Physics in Medicine and Biology*, vol. 38, no. 1, p. 71, 1993.

[35] R. F. Wagner, M. F. Insana, and D. G. Brown, "Statistical properties of radio-frequency and envelope-detected signals with applications to medical ultrasound," *JOSA A*, vol. 4, no. 5, pp. 910–922, May 1987.

[36] S. Tu, J. J. McCombe, D. S. Shumakov, and N. K. Nikolova, "Fast quantitative microwave imaging with resolvent kernel extracted from measurements," *Inverse Problems*, vol. 31, no. 4, 33 pp., Mar. 2015.

[37] D. S. Shumakov, S. Tu, and N. K. Nikolova, "Fast quantitative microwave imaging based on measured point spread functions and inversion in real space," *IEEE AP-S/URSI Int. Symp. Antennas Propag.*, pp. 687–688, Jul. 2015.

[38] T. M. Habashy, R. W. Groom, and B. Spies, "Beyond the Born and Rytov approximations: a nonlinear approach to electromagnetic scattering," *J. Geophys. Res.*, vol. 98, no. B2, pp. 1759–1775, Feb. 1993.

[39] B. Chen and J. J. Stamnes, "Validity of diffraction tomography based on the first Born and the first Rytov approximations," *Applied Optics*, vol. 37, no. 14, pp. 2996–3006, May 1998.

[40] J. G. Proakis and D. G. Manolakis. *Digital Signal Processing: Principles, Algorithms, and Applications*. 3rd ed. Englewood Cliffs, NJ: Prentice-Hall, 1996.

[41] D. L. Donoho, "De-noising by soft-thresholding," *IEEE Trans. Inf. Theory*, vol. 41, no. 3, pp. 613–627, May 1995.

[42] C. Eyraud, J.-M. Geffrin, A. Litman, P. Sabouroux, and H. Giovannini, "Drift correction for scattering measurements," *Applied Physics Lett.*, vol. 89, no. 24, 244104, 3 pp., Dec. 2006.

[43] C. Eyraud, A. Litman, A. Herique, and W. Kofman, "Microwave imaging from experimental data within a Bayesian framework with realistic random noise," *Inverse Problems*, vol. 25, no. 2, 024005, 16 pp., Feb. 2009.

[44] D. S. Shumakov, A. S. Beaverstone, and N. K. Nikolova, "Optimal illumination schemes for near-field microwave imaging," *Progress In Electromagnetics Research*, vol. 157, pp. 93–110, 2016.

[45] A. S. Beaverstone, D. S. Shumakov, and N. K. Nikolova, "Frequency-domain integral equations of scattering for complex scalar responses," *IEEE Trans. Microw. Theory Techn.*, vol. 65, no. 4, pp. 1120–1132, Apr. 2017.

[46] D. S. Shumakov, A. S. Beaverstone, and N. K. Nikolova, "De-noising algorithm for enhancing microwave imaging," *IET J. Eng.*, vol. Mar. 2017, 5 pp., Mar. 2017.

[47] D. S. Shumakov, D. Tajik, A. S. Beaverstone, and N. K. Nikolova, "Real-time quantitative reconstruction methods in microwave imaging," Chapter 17 in *The World of Applied Electromagnetics*, Springer Int. Pub. AG 2017, pp. 415–442.

[48] D. S. Shumakov and N. K. Nikolova, "Fast quantitative microwave imaging with scattered-power maps," *IEEE Trans. Microw. Theory Techn.*, Early Access, pp. 1–11, May 2017.

Chapter 2

Forward Model of Scattering for *S*-parameters

2.1 Introduction

In the models of EM scattering and in microwave imaging in particular, it is customary to use the integral equation of scattering where the response is the electric field vector **E**. However, in practice, the measurements provide a scalar response as a function of frequency or time. The frequency-domain measurements are typically *S*-parameter frequency sweeps in a wide band. In prototypes, these measurements are often performed with a vector network analyzer (VNA). Both magnitude and phase information are used in the reconstruction process [1].

Consequently, the **E**-field at the location of the antenna needs to be linked to the measured responses. This link is not straightforward and it complicates the calibration of the microwave imaging systems. Oversimplifying the relationship between field and response deteriorates the accuracy of the forward model and the quality of the image reconstruction.

In view of the above, microwave imaging can benefit from a forward model of scattering that leads to a data equation where the data are the actual responses, not the **E**-field. The problem of relating the **E**-field model of scattering to the voltage at the antenna

terminals has been addressed before in the context of imaging [2]-[4]. In [2], Green's function is derived for the volume integral equation of scattering where the response is in the form of the *S*-parameters of the network formed by the transmitting (Tx) and receiving (Rx) antennas together with the imaged volume. The derivation adopts the common-impedance definition of the *S*-parameters. Green's function is termed "Green's vector function" as it appears in the form of a vector – it is proportional to the incident field produced by the Rx antenna when this antenna operates in a Tx regime. The derivation of Green's vector in [2] has been conducted for a free-space background using an expansion in spherical modes. It is argued that in principle the result should also hold in the case of heterogeneities.

Recently, an integral equation of scattering for the *S*-parameters or the voltages at the antenna terminals has been proposed in [5]. The novelty and the advantage of this equation is that it is general with regard to the medium and the antennas used in the measurement setup. It is shown rigorously that: (i) a form of Green's vector function exists for any complex-valued scalar response defined as a functional of the field distribution; (ii) the so found Green's function is valid in any reciprocal medium bounded by any type of boundary conditions. Note that the derivation in [5] confirms the common-impedance formula reported in [2] for the case of heterogeneous media.

The reconstruction theory presented in this thesis is cast in the frequency domain, however it can accommodate time-domain measurements as well. Note that all frequency-

domain quantities incorporate the $\exp(\mathrm{i}\omega t)$ time-harmonic factor, where $\mathrm{i}=\sqrt{-1}$, ω is angular frequency, and *t* is time.

In frequency-swept measurements, a network of N_r receivers and N_t transmitters acquires the data at N_f frequencies $f^{(m)}$ ($m=1,...,N_f$), one frequency at a time. Here, we assume that the data are in the form of *S*-parameters $S_{ij}^{(m)}$ ($i=1,...,N_\mathrm{r}$ and $j=1,...,N_\mathrm{t}$). The data equation is obtained as [5]

$$S_{\mathrm{OBJ},n}^{(m)}(\mathbf{r})=S_{\mathrm{RO},n}^{(m)}(\mathbf{r})+\kappa_n^{(m)}\int_{V'}\Delta\varepsilon_{\mathrm{OBJ}}(\mathbf{r}')\left[\mathbf{E}_{\mathrm{RO},i}^{(m)}(\mathbf{r}';\mathbf{r})\cdot\mathbf{E}_{\mathrm{OBJ},j}^{(m)}(\mathbf{r}';\mathbf{r})\right]d\mathbf{r}', \qquad (2.1)$$

where $n=1,...,N_\mathrm{t}\cdot N_\mathrm{r}$ is the response index, $m=1,...,N_f$ is the frequency sample index, $\mathbf{r}'$ is the position inside the inspected volume V', whereas $\mathbf{r}$ is the observation position. Each *n*th experiment corresponds to a unique (*ij*) antenna pair, where the position of the *i*th (Rx) antenna is uniquely defined by $\mathbf{r}$. Figure 2.1 illustrates a planar raster-scanning arrangement where the positions of the Tx and Rx antennas are denoted as $\mathbf{r}_\mathrm{Tx}$ and $\mathbf{r}_\mathrm{Rx}$, respectively. Since the mutual position of the antenna couple remains the same during the scan, one position-vector $\mathbf{r}$ suffices to describe the positions of both antennas. For example, in Figure 2.1 we can define the position of the Rx antenna as $\mathbf{r}_\mathrm{Rx}\equiv\mathbf{r}$, which also defines uniquely the position of the Tx antenna as $\mathbf{r}_\mathrm{Tx}\equiv\mathbf{r}+D\hat{\mathbf{z}}$, where $\hat{\mathbf{z}}$ is the unit vector along *z*.

Note that throughout the thesis, position vectors and vectors of physical fields are in upright bold, whereas matrices are in italic bold. The complex constant at the *m*th

frequency $\kappa_n^{(m)} = -\mathrm{i}\,\omega^{(m)}\varepsilon_0 / 2a_i a_j$ is known. It depends on two quantities: (i) the root-power wave a_i ($\mathrm{W}^{1/2}$) exciting the *i*th port when the *i*th antenna operates in a transmitting mode; (ii) the root-power wave a_j ($\mathrm{W}^{1/2}$) exciting the *j*th port that feeds the Tx antenna. The physical meaning of the root-power waves is explained in [6]. As an example, if the field phasors in (2.1) are root-mean-square (RMS) phasors, then a_i is the square root of the power injected into port i. Note that an *S*-parameter is associated with a particular mode of the *i*th port and a_i relates to the power of that mode only. Further, $\Delta\varepsilon_{\mathrm{OBJ}}(\mathbf{r}')$ is the *relative* permittivity contrast,

$$\Delta\varepsilon_{\mathrm{OBJ}}(\mathbf{r}') = \varepsilon_{\mathrm{OBJ}}(\mathbf{r}') - \varepsilon_{\mathrm{RO}}(\mathbf{r}')\,. \tag{2.2}$$

In (2.1) and (2.2), OBJ (object) stands for CO (calibration object) or OUT (object under test). The scatterer-free measurement setup is referred to as the reference object (RO). Here, the permittivity contrast is assumed frequency-independent. However, if the dispersion relation is known and separable from the spatial dependence, it can be easily incorporated in the resolvent kernel [7].

It is seen that the data equation (2.1) eliminates the need to approximate Green's dyadic, which is now reduced to Green's vector function, $\mathbf{E}^{(m)}_{\mathrm{RO},i}(\mathbf{r}';\mathbf{r})$. In this form, Green's function can be accurately obtained via simulations or measurements.

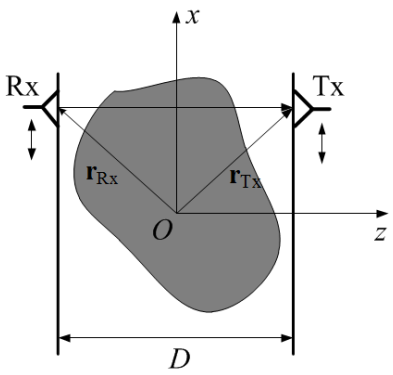

Figure 2.1 Schematic configuration of the planar scanning setup with the Tx and Rx antennas aligned along each other's boresight. *O* denotes the origin of the coordinate system whereas *D* is the distance between the acquisition surfaces. Double headed arrows show the direction of the scan. Since the mutual position between the antennas remains the same during the scan, one position-vector **r** suffices to describe the positions of both antennas.

The kernel in (2.1) consists of two field distributions. The first, $\mathbf{E}^{(m)}_{\mathrm{RO},i}$, represents the incident field that would be generated by the *i*th Rx antenna in the *n*th experiment if this antenna operated in a Tx mode. On the other hand, $\mathbf{E}^{(m)}_{\mathrm{OBJ},j}$ is the total internal field produced by the *j*th Tx antenna in the *n*th experiment. Note that the ordered pair $(\mathbf{r}';\mathbf{r})$ indicates that the internal field distribution is a function of $\mathbf{r}' \in V'$, whereas the position of the respective transmitting antenna is at **r** (see Figure 2.1). It is consistent with the existing convention $(\mathbf{r}_{\mathrm{o}};\mathbf{r}_{\mathrm{s}})$, in which the first position vector is that of the observation point, while the second position vector is that of the source point.

2.2 Strategies for Estimation of the Linearized Resolvent Kernel

Under the Born approximation, (2.1) becomes linear with respect to the unknown permittivity contrast and the *n*th response at the *m*th frequency:

$$S_{\mathrm{OBJ},n}^{(m)}(\mathbf{r}) = S_{\mathrm{RO},n}^{(m)}(\mathbf{r}) + \kappa_n^{(m)} \int_{V'} \Delta\varepsilon_{\mathrm{OBJ}}(\mathbf{r}') \left[\mathbf{E}_{\mathrm{RO},i}(\mathbf{r}';\mathbf{r}) \cdot \mathbf{E}_{\mathrm{RO},j}(\mathbf{r}';\mathbf{r}) \right]^{(m)} d\mathbf{r}' . \qquad (2.3)$$

The field dot-product distribution in the square brackets in (2.3) is referred to as the linearized resolvent kernel and its acquisition is part of the system calibration. We next examine different strategies of estimating the resolvent kernel.

2.2.1 Acquiring the Resolvent Kernel Analytically

In far-zone microwave imaging, the incident fields can be approximated analytically, which is computationally inexpensive and does not require any specific hardware or simulation software. The far field of an antenna in an open space can be approximated using: (a) the plane-wave approximation, or $\sim \exp\left(-\mathrm{i}\mathbf{k}_\mathrm{b} \cdot \mathbf{r}\right)$, (b) locally plane-wave approximation, or $\sim \exp\left(-\mathrm{i}k_\mathrm{b} r\right)$, (c) the spherical-wave (also known as isotropic-wave) approximation, or $\sim \dfrac{\exp(-\mathrm{i}k_\mathrm{b} r)}{r}$, (d) the cylindrical-wave approximation, or $\sim H_0^{(2)}(k_\mathrm{b}\rho)$. Here, k_b represents the background wave number, $\mathbf{k}_\mathrm{b}$ is the background wave vector, r is the distance from the antenna to the observation point, and $\mathbf{r}$ is the position vector of the observation point relative to the antenna. Note that the cylindrical-wave approximation is used in the 2D case of microwave tomography with ρ being the distance from the antenna to the observation point.

The locally plane-wave approximation is extensively used in millimeter-wave reflection holography [8][9]. This approximation is sufficiently accurate when the following conditions are met: (i) the target is in the far zone of the transmitting and receiving antennas, (ii) the distance between the target and the scanned aperture is larger than the biggest dimension of the scanned aperture, and (iii) this distance is at least an order of magnitude larger than the wavelength. However, in near-field imaging some or all of these conditions may not hold, which deteriorates the fidelity of the forward model used in the reconstruction.

The linearized model of scattering (2.3) can be improved by taking the radiation pattern of the antenna into account [10]. This is beneficial when high-gain antennas are used because their radiated power is significantly smaller off boresight. Besides, the phaseless radiation pattern of antennas is always known. It should be noted that in microwave imaging, it is customary to use wide-beam antennas so that the target is interrogated from wider viewing angles, thereby improving the spatial resolution.

Most importantly, the analytical approximations of the resolvent kernel yield only a qualitative outcome. This is because they lack the proper scaling that depends on: (i) the power and phase of the actual excitation and (ii) the volume and contrast of an actual small scatterer. Also, note that analytically obtained resolvent kernels are not valid in near-field imaging applications.

2.2.2 Acquiring the Resolvent Kernel with Simulations

In this case, the field dot-product distribution is estimated by simulating the measurements in the background medium for all N_D responses at all N_f frequencies. Two simulations have to be done at each response – one for the excitation with a transmitter and one for the excitation with a receiver set to operate in a transmitting mode. Keeping in mind that the complexity of an imaging setup is fairly high, the computational time may exceed even a week.

The major advantage of using simulations is in obtaining both vectorial distributions, $\mathbf{E}^{(m)}_{\mathrm{RO},i}(\mathbf{r}';\mathbf{r})$ and $\mathbf{E}^{(m)}_{\mathrm{RO},j}(\mathbf{r}';\mathbf{r})$ in (2.3). Note that one represents Green's function whereas the other approximates the total internal field. Knowing these quantities enables quantitative imaging via nonlinear iterative reconstruction which involves updating the two field distributions separately. Also, simulations are advantageous due to the absence of stochastic noise.

On the other hand, numerical errors such as mesh-convergence errors or imperfect absorbing boundary conditions are present. They can be reduced, however, by performing a mesh convergence study and using a refined mesh in the subsequent simulations. Unfortunately, this refinement may also lead to a prohibitive computational burden.

The main disadvantage of the simulated resolvent kernels is that they are often incapable of properly modeling the actual setup due to modeling errors [11][12]. Unlike numerical errors, modeling errors are much more difficult to eliminate. They arise from the inability to account for errors within the fabrication tolerances of the antennas and the imaging setup, uncertainties in the constitutive parameters of the materials used in the

measurement enclosure, deformations caused by temperature or humidity, aging of the materials, etc. Moreover, the complexities in the cables, connectors, screws, supporting plates and so on are often ignored. Finally, the electromagnetic interference and positioning errors in the acquisition setup as well as the measurement errors are difficult to predict. All these factors corrupt the forward model fidelity, thereby making the quantitative results obtained with a simulated resolvent kernel not reliable, especially in near-field imaging.

2.2.3 Acquiring the Resolvent Kernel Experimentally

The experimental acquisition of the resolvent kernel $\mathbf{E}^{(m)}_{\mathrm{RO},i}(\mathbf{r}';\mathbf{r})\cdot\mathbf{E}^{(m)}_{\mathrm{RO},j}(\mathbf{r}';\mathbf{r})$ offers the best fidelity [7][12]. For that, an electrically small scattering probe is placed in the RO and is measured. Together with the RO, this scattering probe forms the CO. We next examine two calibration strategies that can be used in near-field quantitative linear inversion: the one employing a dielectric scattering probe and the second one employing a metallic scattering probe.

2.2.3.1 Calibration with Dielectric Scattering Probe

Calibration with a scattering probe has been widely used in optical, acoustic and microwave imaging [12]-[19]. Here, it is discussed within the framework of linear-inversion methods in near-field microwave imaging [12][13][19]. The concept is simple – an electrically small cube or a sphere with a known relative permittivity contrast is used as a scattering probe within the RO. Its maximum dimension has to be equal to or smaller

than $\lambda_{\mathrm{CO}}/4$, where λ_{CO} is the shortest wavelength in the CO. This ensures that the scattering probe is illuminated by a relatively uniform wave field. As a whole, the volume of a scattering probe and its relative permittivity must satisfy the limits of Born's approximation [20]. We emphasize that since the CO response represents the resolvent kernel of each particular imaging system, the rule of thumb is that if the CO cannot be imaged, the OUT cannot be reconstructed either. Thus, this calibration measurement also provides information about the system sensitivity.

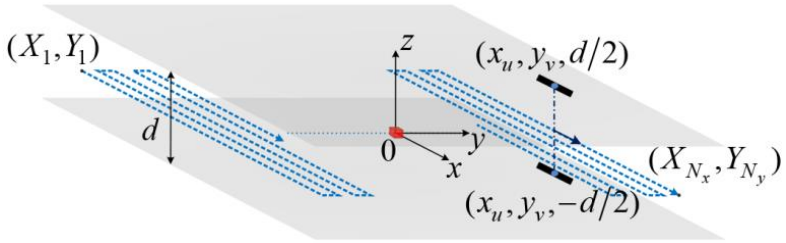

Figure 2.2 Schematic configuration of the planar scanning setup for the calibration object measurements: two aligned antennas (shown with thick black lines) separated by a distance *d* are moving together along the scanning route (shown with blue dash lines) in a raster fashion. A scattering probe (red cube) is placed at the origin. The sampling position is $\mathbf{r}_{uv} = (x_u, y_v \,|\, z)$. The sampling involves N_x samples along *x* and N_y samples along *y*.

The scattering probe is positioned at the center of the inspected domain ($\mathbf{r}_0' = 0$) and the sensors scan over the whole acquisition surface (Figure 2.2). For a single voxel-size scattering probe of known relative permittivity contrast $\delta\varepsilon_{\mathrm{CO}}$ embedded in the RO, the resolvent kernel at $\mathbf{r}_0' = 0$ can be obtained from (2.3) as

$$\left[\mathbf{E}_{\mathrm{RO},i} \cdot \mathbf{E}_{\mathrm{RO},j}\right]^{(m)}_{(\mathbf{r}'=0;\mathbf{r})} \approx \frac{\Delta S^{(m)}_{\mathrm{CO},n}(\mathbf{r})}{\kappa_n^{(m)} \delta\varepsilon_{\mathrm{CO}} \Omega_{\mathrm{v}}}, \tag{2.4}$$

where Ω_{v} is the volume of the scatterer and $\Delta S_{\mathrm{CO},n}^{(m)}(\mathbf{r}) = S_{\mathrm{CO},n}^{(m)}(\mathbf{r}) - S_{\mathrm{RO},n}^{(m)}(\mathbf{r})$ are the scattered CO responses. These responses form the PSF of the imaging system.

In a uniform RO, measuring the PSF with a scattering probe at the center of an imaged domain is sufficient since the CO responses at all other lateral locations $\mathbf{r}'_p \in V'$, $p = 1,...,N_{\mathrm{v}}$, can be obtained from it by coordinate translation. Let the CO responses acquired on a planar surface with a scattering probe at the center, $\mathbf{r}'_0 = (x'_0, y'_0 \,|\, z')$, be denoted as $\Delta S_{\mathrm{CO},n,\mathbf{r}'_0}^{(m)}(\mathbf{r}_{uv})$, $u = 1,...,N_x$, $v = 1,...,N_y$. Let the CO responses due to a scattering probe at $\mathbf{r}'_p = (x'_p, y'_p \,|\, z')$ be denoted as $\Delta S_{\mathrm{CO},n,\mathbf{r}'_p}^{(m)}(\mathbf{r}_{uv})$. Then, the following holds

$$\Delta S_{\mathrm{CO},n,\mathbf{r}'_p}^{(m)}(\mathbf{r}_{uv}) = \Delta S_{\mathrm{CO},n,\mathbf{r}'_0}^{(m)}(\mathbf{r}_{uv} - \Delta\mathbf{r}), \tag{2.5}$$

where $\Delta\mathbf{r} = \mathbf{r}'_p - \mathbf{r}'_0 = (x'_p - x'_0, y'_p - y'_0 \,|\, 0)$.

Obtaining the CO responses from the PSFs at various range locations of the scattering probe is not as straightforward since the planar system scans only laterally and translations along range do not apply. The simplest and most reliable approach is to acquire the PSFs at several range locations of the scattering probe inside the volume of interest. By interpolating the acquired PSFs with respect to *z*, images at other range locations can be obtained.

2.2.3.2 Calibration with Metallic Scattering Probe

Calibration strategy employing a metallic scattering probe has been recently proposed in [5]. It uses the theoretical model of scattering from an electrically short perfectly conducting wire [21].

Under the linear Born approximation, the CO scattered response $\Delta S_{\mathrm{CO},n}^{(m)}(\mathbf{r})$ can be obtained from (2.3) as

$$\Delta S_{\mathrm{CO},n}^{(m)}(\mathbf{r}) = \kappa_n^{(m)} \int_{V'} \Delta\varepsilon_{\mathrm{CO}}(\mathbf{r}') \left[\mathbf{E}_{\mathrm{RO},i}(\mathbf{r}';\mathbf{r}) \cdot \mathbf{E}_{\mathrm{RO},j}(\mathbf{r}';\mathbf{r}) \right]^{(m)} d\mathbf{r}' , \tag{2.6}$$

where $\Delta\varepsilon_{\mathrm{CO}}$ is the CO relative permittivity contrast as per (2.2). Measuring the system PSF allows for a straightforward extraction of the kernel $\left[\mathbf{E}_{\mathrm{RO},i}(\mathbf{r}';\mathbf{r}) \cdot \mathbf{E}_{\mathrm{RO},j}(\mathbf{r}';\mathbf{r}) \right]^{(m)}$ in (2.6) similarly to (2.4). Next, it is shown that each of the field distributions comprising this kernel can be obtained separately from the *S*-parameter measurements.

Assume that the scattering is due to an electrically short perfectly conducting straight very thin piece of wire. This scattering problem is well known (see [21]). Surface current density $\mathbf{J}_{\mathrm{s},j}^{\mathrm{ind}(m)}$ is induced at the wire's surface s_{w} upon illumination by the *j*th antenna. The CO scattered response can then be expressed in terms of this induced source as [5]:

$$\Delta S_{\mathrm{CO},n}^{(m)}(\mathbf{r}) = \frac{1}{a_i a_j} \iint_{s_{\mathrm{w}}} \mathbf{E}_{\mathrm{RO},i}^{(m)}(\mathbf{r}';\mathbf{r}) \cdot \mathbf{J}_{\mathrm{s},j}^{\mathrm{ind}(m)}(\mathbf{r}') ds' . \tag{2.7}$$

As shown in [21], the surface current can be replaced by a current along the wire $I_j^{\mathrm{ind}(m)}$ provided the wire's radius *a* is much smaller than its length $2h$, $a \ll h$. In this case, (2.7) reduces to

$$\Delta S_{\mathrm{CO},n}^{(m)}(\mathbf{r}) = \frac{1}{a_i a_j}\int_{-h}^{h} I_j^{\mathrm{ind}(m)}(x')\left[\hat{\mathbf{x}}\cdot\mathbf{E}_{\mathrm{RO},i}^{(m)}(x')\right]dx' . \tag{2.8}$$

Here, $\hat{\mathbf{x}}$ is along the wire's axis and x' is the axial position. Further, if $k_0^{(m)}h << 1$, the induced current is expressed as [21]:

$$I_j^{\mathrm{ind}(m)}(x') = I_{0,j}^{(m)}\left[1-\left(\frac{x'}{h}\right)^2\right],\ |x'| \le h \tag{2.9}$$

where

$$I_{0,j}^{(m)} = \alpha^{(m)}\left(\hat{\mathbf{x}}\cdot\mathbf{E}_{\mathrm{RO},j}^{(m)}\right), \tag{2.10}$$

$$\alpha^{(m)} \approx \frac{\mathrm{i}\pi\varepsilon_0\varepsilon_{\mathrm{r,RO}}^{(m)}\omega^{(m)}h^2}{\left[\frac{1}{2}\ln\left(\frac{\beta+1}{\beta-1}\right)-\frac{1}{\beta}\right]\left[1-\frac{1}{2}\left(k^{(m)}h\beta\right)^2\right]+\mathrm{i}\frac{2}{9}\left(k^{(m)}h\right)^3}, \tag{2.11}$$

$$\beta = \sqrt{1+\left(a/h\right)^2} . \tag{2.12}$$

Note that $\mathbf{E}_{\mathrm{RO},j}^{(m)}$ is assumed constant along the wire's extent since the wire is electrically small and sufficiently far from the *j*th source. With this assumption, the integration in (2.8) is performed using (2.9), which yields

$$\Delta S^{(m)}_{\mathrm{CO},n,\mathbf{r}_\mathrm{w}}(\mathbf{r}) \approx \frac{\alpha^{(m)}}{a_i a_j} \cdot \frac{4h}{3} \cdot \left[\hat{\mathbf{x}} \cdot \mathbf{E}^{(m)}_{\mathrm{RO},i}(\mathbf{r}_\mathrm{w};\mathbf{r})\right]\left[\hat{\mathbf{x}} \cdot \mathbf{E}^{(m)}_{\mathrm{RO},j}(\mathbf{r}_\mathrm{w};\mathbf{r})\right]. \tag{2.13}$$

Here, $\mathbf{r}_\mathrm{w}$ is the position of the wire's center.

We can see that each of the $\mathbf{E}^{(m)}_{\mathrm{RO},i}$ and $\mathbf{E}^{(m)}_{\mathrm{RO},j}$ distributions can be mapped individually by *S*-parameter measurements. The separation of these two field distributions in the kernel is critical in the nonlinear reconstruction methods where $\mathbf{E}^{(m)}_{\mathrm{RO},j}$ and/or $\mathbf{E}^{(m)}_{\mathrm{RO},i}$ are subjected separately to iterative updates.

Notice that, with a wire scatterer, only one field component may be resolved at a time. This is in fact desirable when full polarimetric information is required. With the wire being in two mutually orthogonal positions in two consecutive measurements, the polarization vector of the wave can be determined since the approach provides both amplitude and phase information. Another advantage of the wire shape is its simple scattering model, which employs only electric equivalent current (see (2.8)).

In conclusion, if the inspected volume is uniform, one measurement of the system PSF with a scattering probe at the center suffices in estimating the resolvent kernel of the data equation for all responses. Even though such measurement has to be repeated for several range locations, it still proves to be faster than simulations.

As a final remark, it should be noted that an acquisition of the measured resolvent kernel is impossible when the imaged domain is inaccessible for a scattering probe to be embedded in it. In addition, both simulated and measured resolvent kernels cannot be

estimated in the case of a completely unknown imaged scene since it cannot be emulated before the imaging system is deployed on site. In such cases, we have to resort to analytical approximations.

2.3 Linear Approximations of the Data Equation

2.3.1 Calibration with Dielectric Scattering Probe

In case of a calibration with dielectric scattering probe, the CO consists of a single voxel-size scatterer (the scattering probe) of known relative permittivity contrast $\delta\varepsilon_{\mathrm{CO}}$ embedded in the RO. Let V' be uniformly discretized into N_{v} voxels of volume Ω_{v} and let the scattering probe reside at the pth voxel ($p=1,...,N_{\mathrm{v}}$), the position of which is given by $\mathbf{r}'_p \in V'$. Assuming constant field inside the probe, its nth scattered response,

$$\Delta S^{(m)}_{\mathrm{CO},n,\mathbf{r}'_p}(\mathbf{r}) = S^{(m)}_{\mathrm{CO},n,\mathbf{r}'_p}(\mathbf{r}) - S^{(m)}_{\mathrm{RO},n}(\mathbf{r}) \tag{2.14}$$

is obtained from (2.1) as

$$\Delta S^{(m)}_{\mathrm{CO},n,\mathbf{r}'_p}(\mathbf{r}) \approx \kappa^{(m)}_n \delta\varepsilon_{\mathrm{CO}} \Omega_{\mathrm{v}} \left[\mathbf{E}^{(m)}_{\mathrm{RO},i}(\mathbf{r}'_p;\mathbf{r}) \cdot \mathbf{E}^{(m)}_{\mathrm{CO},j}(\mathbf{r}'_p;\mathbf{r}) \right]. \tag{2.15}$$

The expression in (2.15) represents the PSF of the nth response of the imaging system.

2.3.1.1 Localized Quasi-Linear Approximation

To express the total field $\mathbf{E}_{\mathrm{CO}}$ in the scattering probe in terms of the incident field $\mathbf{E}_{\mathrm{RO}}$, we utilize the localized quasi-linear (LQL) approximation, which has a wider range of

applicability compared to the Born approximation [22][23]. It assumes that the total field within an electrically small scatterer is proportional to the incident field via a reflectivity tensor $\bar{\bar{\boldsymbol{\lambda}}}$:

$$\mathbf{E}^{(m)}_{\mathrm{CO},j}(\mathbf{r}'_p;\mathbf{r}) \approx \bar{\bar{\boldsymbol{\lambda}}}^{(m)}_{\mathrm{CO}} \cdot \mathbf{E}^{(m)}_{\mathrm{RO},j}(\mathbf{r}'_p;\mathbf{r}) \,. \tag{2.16}$$

Note that (2.16) is similar to the localized nonlinear approximation, which employs the depolarization tensor $\bar{\bar{\boldsymbol{\Gamma}}}$ instead of $\bar{\bar{\boldsymbol{\lambda}}}$ [20][24]. These two quantities are formally related by a linear relationship [22]. What is important here is that the localized nonlinear approximation is most suitable for the scenarios when the internal field is a smoothly varying function of position, which is not the case with near-field imaging.

We assume that the total field $\mathbf{E}_{\mathrm{CO}}$ inside the scattering probe is collinear with the incident field $\mathbf{E}_{\mathrm{RO}}$. In this case, $\bar{\bar{\boldsymbol{\lambda}}}_{\mathrm{CO}}$ is expressed through a coefficient λ_{CO} as:

$$\bar{\bar{\boldsymbol{\lambda}}}_{\mathrm{CO}} = \lambda_{\mathrm{CO}} \bar{\bar{\mathbf{I}}} \,. \tag{2.17}$$

Substituting (2.17) into (2.15) leads to

$$\left[\mathbf{E}^{(m)}_{\mathrm{RO},i}(\mathbf{r}'_p;\mathbf{r}) \cdot \mathbf{E}^{(m)}_{\mathrm{RO},j}(\mathbf{r}'_p;\mathbf{r}) \right]_{\mathrm{LQL}} \approx \frac{\Delta S^{(m)}_{\mathrm{CO},n,\mathbf{r}'_p}(\mathbf{r})}{\kappa_n^{(m)} \delta\varepsilon_{\mathrm{CO}} \Omega_{\mathrm{v}} \lambda^{(m)}_{\mathrm{CO}}} \,. \tag{2.18}$$

The above is the LQL resolvent kernel of the forward model specific to the *n*th response of the imaging system.

Next, the forward model (2.1) is applied to the OUT data:

$$\Delta S^{(m)}_{\mathrm{OUT},n}(\mathbf{r}) = \kappa_n^{(m)} \int_{V'} \Delta\varepsilon_{\mathrm{OUT}}(\mathbf{r}') \left[\mathbf{E}^{(m)}_{\mathrm{RO},i}(\mathbf{r}';\mathbf{r}) \cdot \mathbf{E}^{(m)}_{\mathrm{OUT},j}(\mathbf{r}';\mathbf{r}) \right] d\mathbf{r}' \,. \tag{2.19}$$

Neglecting the mutual coupling between the scattering voxels in the OUT, the LQL approximation is applied to (2.19) to obtain

$$\Delta S^{(m)}_{\mathrm{OUT},n,\mathrm{LQL}}(\mathbf{r}) \approx \kappa_n^{(m)} \int_{V'} \Delta\varepsilon_{\mathrm{OUT}}(\mathbf{r}') \lambda^{(m)}_{\mathrm{OUT}}(\mathbf{r}') \left[\mathbf{E}^{(m)}_{\mathrm{RO},i}(\mathbf{r}';\mathbf{r}) \cdot \mathbf{E}^{(m)}_{\mathrm{RO},j}(\mathbf{r}';\mathbf{r}) \right]_{\mathrm{LQL}} d\mathbf{r}'. \tag{2.20}$$

The substitution of (2.18) into (2.20) with $\mathbf{r}'_p \equiv \mathbf{r}'$ leads to

$$\Delta S^{(m)}_{\mathrm{OUT},n,\mathrm{LQL}}(\mathbf{r}) \approx \int_{V'} \Delta\varepsilon_{\mathrm{OUT}}(\mathbf{r}') \lambda^{(m)}_{\mathrm{OUT}}(\mathbf{r}') \left[\frac{\Delta S^{(m)}_{\mathrm{CO},n,\mathbf{r}'}(\mathbf{r})}{\delta\varepsilon_{\mathrm{CO}} \Omega_{\mathrm{v}} \lambda^{(m)}_{\mathrm{CO}}} \right] d\mathbf{r}' \,. \tag{2.21}$$

Note that all the quantities in the square brackets of (2.21) are known and they inherently incorporate the Green's function of the specific imaging setup.

2.3.1.2 Localized Quasi-Linear Rytov Approximation

Here, we derive the LQL Rytov (LQLR) approximation for the data equation using the LQL approximation of the CO internal field (2.16). The LQLR approximation can be expressed in terms of the LQL approximation in the following way [25]:

$$S^{(m)}_{\mathrm{OBJ},n,\mathrm{LQLR}}(\mathbf{r}) \approx S^{(m)}_{\mathrm{RO},n}(\mathbf{r}) \exp\left[\frac{\Delta S^{(m)}_{\mathrm{OBJ},n,\mathrm{LQL}}(\mathbf{r})}{S^{(m)}_{\mathrm{RO},n}(\mathbf{r})} \right]. \tag{2.22}$$

In the case of $\mathrm{OBJ} \equiv \mathrm{CO}$, where the scattering probe is at $\mathbf{r}'$, we set $S^{(m)}_{\mathrm{OBJ},n,\mathrm{LQLR}}(\mathbf{r}) = S^{(m)}_{\mathrm{CO},n,\mathbf{r}'}(\mathbf{r})$ and re-arrange to obtain

$$\Delta S^{(m)}_{\mathrm{CO},n,\mathrm{LQL},\mathbf{r}'}(\mathbf{r}) \approx S^{(m)}_{\mathrm{RO},n}(\mathbf{r}) \ln\left[\frac{S^{(m)}_{\mathrm{CO},n,\mathbf{r}'}(\mathbf{r})}{S^{(m)}_{\mathrm{RO},n}(\mathbf{r})}\right]. \tag{2.23}$$

Using (2.15) and (2.17), the *n*th CO scattered response for a scattering probe at $\mathbf{r}'$ at the *m*th frequency is obtained as

$$\Delta S^{(m)}_{\mathrm{CO},n,\mathbf{r}',\mathrm{LQL}}(\mathbf{r}) = \kappa_n^{(m)} \delta\varepsilon_{\mathrm{CO}} \Omega_{\mathrm{v}} \lambda^{(m)}_{\mathrm{CO}} \left[\mathbf{E}^{(m)}_{\mathrm{RO},i}(\mathbf{r}';\mathbf{r}) \cdot \mathbf{E}^{(m)}_{\mathrm{RO},j}(\mathbf{r}';\mathbf{r})\right]. \tag{2.24}$$

It follows from (2.23) and (2.24), that the LQLR resolvent kernel can be expressed as

$$\left[\mathbf{E}^{(m)}_{\mathrm{RO},i}(\mathbf{r}';\mathbf{r}) \cdot \mathbf{E}^{(m)}_{\mathrm{RO},j}(\mathbf{r}';\mathbf{r})\right]_{\mathrm{LQLR}} \approx \frac{S^{(m)}_{\mathrm{RO},n}(\mathbf{r}) \cdot \ln\left[S^{(m)}_{\mathrm{CO},n,\mathbf{r}'}(\mathbf{r}) / S^{(m)}_{\mathrm{RO},n}(\mathbf{r})\right]}{\kappa_n^{(m)} \delta\varepsilon_{\mathrm{CO}} \Omega_{\mathrm{v}} \lambda^{(m)}_{\mathrm{CO}}}. \tag{2.25}$$

Finally, to obtain the expression for the forward model of scattering under the LQLR approximation, we use the expression of the LQL forward model (2.20) and replace its resolvent kernel with the one from (2.25):

$$\begin{aligned} S^{(m)}_{\mathrm{RO},n}(\mathbf{r}) \cdot \ln\left[\frac{S^{(m)}_{\mathrm{OUT},n}(\mathbf{r})}{S^{(m)}_{\mathrm{RO},n}(\mathbf{r})}\right] \approx & \int_{V'} \Delta\varepsilon_{\mathrm{OUT}}(\mathbf{r}') \times \\ & \lambda^{(m)}_{\mathrm{OUT}}(\mathbf{r}') \left[\frac{S^{(m)}_{\mathrm{RO},n}(\mathbf{r}) \cdot \ln\left(S^{(m)}_{\mathrm{CO},n,\mathbf{r}'}(\mathbf{r}) / S^{(m)}_{\mathrm{RO},n}(\mathbf{r})\right)}{\delta\varepsilon_{\mathrm{CO}} \Omega_{\mathrm{v}} \lambda^{(m)}_{\mathrm{CO}}}\right] d\mathbf{r}'. \end{aligned} \tag{2.26}$$

Note that we write the expression for $\Delta S^{(m)}_{\mathrm{OUT},n,\mathrm{LQL}}(\mathbf{r})$ in the left-hand side of (2.26) explicitly. For that, (2.22) is re-arranged similarly to (2.23), but with $\mathrm{OBJ} \equiv \mathrm{OUT}$ and $S^{(m)}_{\mathrm{OBJ},n,\mathrm{LQLR}}(\mathbf{r}) = S^{(m)}_{\mathrm{OUT},n}(\mathbf{r})$. Also, note that the left-hand side as well as all the quantities in the square brackets of the right-hand side of (2.26) are known, which allows for

formulating a respective system of equations for the unknown distribution $\Delta\varepsilon_{\mathrm{OUT}}(\mathbf{r}')$, $\mathbf{r}' \in V'$.

2.3.2 Calibration with Metallic Scattering Probe

Calibration with a dielectric scattering probe has a significant limitation. For accurate quantitative results, the permittivity of a voxel in the OUT must be close to that of the scattering probe in the CO [13][19]. Since the permittivity of the scattering probe is fixed, the quantitative reconstruction of objects with widely varying permittivity distribution is not likely to be accurate. In order to achieve target-independent quantitative accuracy, a new calibration strategy employing a metallic scattering probe can be used.

In case of a calibration with metallic scattering probe, the CO consists of an electrically short perfectly conducting straight piece of wire embedded in the RO. This calibration step aims at acquiring the incident-field distributions due to all antennas (Tx and Rx) in the setup. The so-obtained distributions can then be used to construct a system-specific scattering model [5].

2.3.2.1 Linear Born Approximation

The CO scattered response from an electrically small wire under the linear Born (LB) approximation has been obtained in (2.13). Using this result, we can express the resolvent kernel as

$$\left(\left[\hat{\mathbf{x}}\cdot\mathbf{E}^{(m)}_{\mathrm{RO},i}(\mathbf{r}'_{\mathrm{w}};\mathbf{r})\right]\left[\hat{\mathbf{x}}\cdot\mathbf{E}^{(m)}_{\mathrm{RO},j}(\mathbf{r}'_{\mathrm{w}};\mathbf{r})\right]\right)_{\mathrm{LB}} \approx \frac{3a_i a_j \Delta S^{(m)}_{\mathrm{CO},n,\mathbf{r}'_{\mathrm{w}}}(\mathbf{r})}{\alpha^{(m)} 4h}, \tag{2.27}$$

where $\mathbf{r}'_{\mathrm{w}} \in V'$ is the position of the scattering probe's center. The above is the LB resolvent kernel of the forward model specific to the *n*th response of the imaging system.

Neglecting the mutual coupling between the scattering voxels in the OUT, the LB approximation is applied to (2.19) to obtain

$$\Delta S^{(m)}_{\mathrm{OUT},n,\mathrm{LB}}(\mathbf{r}) \approx \kappa_n^{(m)} \int_{V'} \Delta\varepsilon_{\mathrm{OUT}}(\mathbf{r}') \left[\mathbf{E}^{(m)}_{\mathrm{RO},i}(\mathbf{r}';\mathbf{r}) \cdot \mathbf{E}^{(m)}_{\mathrm{RO},j}(\mathbf{r}';\mathbf{r}) \right]_{\mathrm{LB}} d\mathbf{r}'. \tag{2.28}$$

Substituting (2.27) into (2.28) with $\mathbf{r}'_{\mathrm{w}} \equiv \mathbf{r}'$ and using $\kappa_n^{(m)} = -\mathrm{i}\,\omega^{(m)}\varepsilon_0 / 2a_i a_j$ leads to

$$\Delta S^{(m)}_{\mathrm{OUT},n,\mathrm{LB}}(\mathbf{r}) \approx -\int_{V'} \Delta\varepsilon_{\mathrm{OUT}}(\mathbf{r}') \left[\frac{\mathrm{i}\,\omega^{(m)}\varepsilon_0 3 \Delta S^{(m)}_{\mathrm{CO},n,\mathbf{r}'}(\mathbf{r})}{\alpha^{(m)} 8h} \right] d\mathbf{r}'. \tag{2.29}$$

All the quantities in the square brackets of (2.29) are known. Note that in (2.27) and (2.29), the wire's axis is along *x* and it has been assumed that the *y* and *z* **E**-field components are negligible. Analogous expressions accounting for the positioning of the wire along *y* and *z* can be easily obtained and added to the *x* field term in (2.29).

2.3.2.2 Linear Rytov Approximation

The linear Rytov (LR) approximation for the data equation is presented next based on the LB model. For that, we follow the derivation given in the case of the calibration with a dielectric scattering probe (see (2.22)-(2.26)). Thus, the forward model of scattering under the LR approximation is expressed using (2.29) as

$$S_{\mathrm{RO},n}^{(m)}(\mathbf{r})\cdot\ln\left[\frac{S_{\mathrm{OUT},n}^{(m)}(\mathbf{r})}{S_{\mathrm{RO},n}^{(m)}(\mathbf{r})}\right]\approx-\int_{V'}\Delta\varepsilon_{\mathrm{OUT}}(\mathbf{r}')\times \left[\frac{\mathrm{i}\,\omega^{(m)}\varepsilon_0 3S_{\mathrm{RO},n}^{(m)}(\mathbf{r})\cdot\ln\left(S_{\mathrm{CO},n,\mathbf{r}'}^{(m)}(\mathbf{r})/S_{\mathrm{RO},n}^{(m)}(\mathbf{r})\right)}{\alpha^{(m)}8h}\right]d\mathbf{r}'. \tag{2.30}$$

The left-hand side and all the quantities in the square brackets of (2.30) are known. Thus, the respective system of equations can be formed for the unknown distribution $\Delta\varepsilon_{\mathrm{OUT}}(\mathbf{r}'),\ \mathbf{r}'\in V'$.

2.3.3 Limitations of the Linearized Forward Model

The major limitation of all direct-inversion methods is their inability to account for the mutual coupling and multiple scattering present in the OUT. Such effects dominate the scattering in complex heterogeneous objects such as living tissue, luggage items, structural components in civil engineering, etc.

In general, the accuracy of the LQL approximation and LQLR approximation is a function of frequency and the size of the imaged target [20][22][23]. It is well known that the original Rytov approximation outperforms Born's approximation when electrically large low-contrast objects are imaged since the accuracy of the Rytov approximation does not depend on the scatterer's size [20][26][27]. Therefore, in general, the LQLR approximation is expected to provide additional phase corrections to the simpler LQL approximation in the case of electrically-large scatterers.

References

[1] N. K. Nikolova, "Microwave biomedical imaging," *Wiley Encyclopedia of Electrical and Electronics Engineering*, pp. 1–22. (published online Apr. 25, 2014).

[2] M. Haynes and M. Moghaddam, "Vector Green's function for *S*-parameter measurements of the electromagnetic volume integral equation," *IEEE Trans. Antennas Propag.*, vol. 60, no. 3, pp. 1400–1413, Mar. 2012.

[3] M. Haynes and M. Moghaddam, "Multipole and *S*-parameter antenna and propagation model," *IEEE Trans. Antennas Propag.*, vol. 59, no. 1, pp. 225–235, Jan. 2011.

[4] M. N. Akinci *et al*., "Qualitative microwave imaging with scattering parameters measurements," *IEEE Trans. Microw. Theory Techn.*, vol. 63, no. 9, pp. 2730–2740, Sep. 2015.

[5] A. S. Beaverstone, D. S. Shumakov, and N. K. Nikolova, "Frequency-domain integral equations of scattering for complex scalar responses," *IEEE Trans. Microw. Theory Techn.*, vol. 65, no. 4, pp. 1120–1132, Apr. 2017.

[6] D. M. Pozar, "Microwave network analysis," in Microwave Engineering, 2nd ed. Hoboken, NJ, USA: Wiley, 1998, pp. 204–205.

[7] N. K. Nikolova, *Introduction to Microwave Imaging*. Cambridge University Press, 2017.

[8] D. M. Sheen, D. L. McMakin, and T. E. Hall, "Near-field three-dimensional radar imaging techniques and applications," *Applied Optics*, vol. 49, no. 19, pp. E83–E93, Jul. 2010.

[9] D. M. Sheen, D. L. McMakin, and T. E. Hall, "Three-dimensional millimeter-wave imaging for concealed weapon detection," *IEEE Trans. Microw. Theory Techn.*, vol. 49, no. 9, pp. 1581–1592, Sep. 2001.

[10] R. K. Amineh, J. J. McCombe, and N. K. Nikolova, "Microwave holographic imaging using the antenna phaseless radiation pattern," *IEEE Antennas and Wireless Propag. Lett.*, vol. 11, pp. 1529–1532, 2012.

[11] M. Ostadrahimi, P. Mojabi, C. Gilmore, A. Zakaria, S. Noghanian, S. Pistorius, and J. LoVetri, "Analysis of incident field modeling and incident/scattered field calibration techniques in microwave tomography," *IEEE Antennas and Wireless Propag. Lett.*, vol. 10, pp. 900–903, Sep. 2011.

[12] R. K. Amineh, J. J. McCombe, A. Khalatpour, and N. K. Nikolova, "Microwave holography using point-spread functions measured with calibration objects," *IEEE Trans. Instrum. Meas.*, vol. 64, no. 2, pp. 403–417, Feb. 2015.

[13] D. Tajik, J. Thompson, A. S. Beaverstone, and N. K. Nikolova, "Real-time quantitative reconstruction based on microwave holography," *IEEE AP-S/URSI Int. Symp. on Antennas Propag.*, Fajardo, Puerto Rico, pp. 851–852, Jun. 2016.

[14] J. W. Goodman. *Introduction to Fourier Optics*. New York, NY, USA: McGraw-Hill, 1996.

[15] A. Schatzberg and A. J. Devaney, "Super-resolution in diffraction tomography," *Inverse Problems*, vol. 8, no. 1, pp. 149–164, 1992.

[16] L. Diener, "Microwave near-field imaging with open-ended waveguide – Comparison with other techniques of non-destructive testing," *Res. Nondestruct. Eval.*, vol. 7, no. 2, pp. 137–152, 1995.

[17] M. Bertero, M. Miyakawa, P. Boccacci, F. Conte, K. Orikasa, and M. Furutani, "Image restoration in chirp-pulse microwave CT (CP-MCT)," *IEEE Trans. Biomed. Eng.*, vol. 47, no. 5, pp. 690–699, May 2000.

[18] T. G. Savelyev and A. G. Yarovoy, "Fast imaging by 3-D deconvolution in short-range UWB radar for concealed weapon detection," in *Proc. 9th Eur. Radar Conf. (EuRAD)*, pp. 26–29, Oct./Nov. 2012.

[19] S. Tu, J. J. McCombe, D. S. Shumakov, and N. K. Nikolova, "Fast quantitative microwave imaging with resolvent kernel extracted from measurements," *Inverse Problems*, vol. 31, no. 4, 33 pp., Mar. 2015.

[20] T. M. Habashy, R. W. Groom, and B. R. Spies, "Beyond the Born and Rytov approximations: a nonlinear approach to electromagnetic scattering," *J. Geophys. Res.*, vol. 98, no. B2, pp. 1759–1775, Feb. 1993.

[21] G. S. Smith. *An Introduction to Classical Electromagnetic Radiation*. Cambridge, U.K.: Cambridge Univ. Press, 1997.

[22] M. S. Zhdanov and S. Fang, "Quasi-linear approximation in 3D EM modeling," *Geophysics*, vol. 61, no. 3, pp. 646–665, Jun 1996.

[23] M. S. Zhdanov and E. Tartaras, "Three-dimensional inversion of multitransmitter electromagnetic data based on the localized quasi-linear approximation," *Geophys. J. Int.*, vol. 148, pp. 506–519, Mar. 2002.

[24] C. Torres-Verdin and T. M. Habashy, "Rapid 2.5-dimensional forward modeling and inversion via a new nonlinear scattering approximation," *Radio Science*, vol. 29, no. 4, pp. 1051–1079, Jul.-Aug. 1994.

[25] N. K. Nikolova, "The basics of microwave imaging," in *Principles of RF and Microwave Imaging Technology: From Radar to MRI*, Short Course SFB, *2016 Int. Microw. Symp.*, May 2016.

[26] B. Chen and J. J. Stamnes, "Validity of diffraction tomography based on the first Born and the first Rytov approximations," *Applied Optics*, vol. 37, no. 14, pp. 2996–3006, May 1998.

[27] M. Slaney, A. C. Kak, and L. E. Larsen, "Limitations of imaging with first-order diffraction tomography," *IEEE Trans. Microw. Theory Techn.*, vol. 32, no. 8, pp. 860–874, Aug. 1984.

Chapter 3

Theory of the Direct Inversion with Scattered Power Maps

3.1 Introduction

In microwave imaging, the nonlinear inverse problem can be linearized by making certain approximations of the internal total field. The linear Born approximation is the classic example of such linearization [1][2]. It exploits the assumption that the total field is the same as the incident field within the imaged domain. In another linearization strategy, the Rytov approximation, the total internal field is expressed as an exponential correction to the known incident field [3][4]. Typically, the application of linear approximations is limited to the weak-scattering problems with each approximation having its pros and cons. For example, the Rytov approximation requires small contrast but is independent of the size of the scatterer unlike the Born approximation [5]. More recent approximations have been developed to enhance the accuracy and the range of applicability of the Born and Rytov approximations [5]-[7].

Once the inverse problem is linearized, it is solved by direct inversion methods, also known as linear inversion methods. In one such method, microwave holography, a linear system of equations is solved in Fourier domain, typically employing least-square

strategies [8]-[12]. Another representative example is diffraction tomography which is analogous to the inversion scheme used in X-ray computed tomography [13]-[17]. Unlike holography, it applies to 2D imaging in a cross section of the imaged object. The diffraction effects are incorporated by replacing the simplistic straight-line propagation model with a more realistic incident field and Green's function. In case of far-zone measurements, the measured scattered field can be related to the Fourier transform of the contrast function and the inversion can be done via an inverse Fourier transform [18][19].

Sensitivity-based imaging is another qualitative method operating on the frequency-domain measured data [20][21]. The linear problem is solved in the spatial domain with no matrix inversion. The method calculates the Fréchet derivatives of a least-square response-error function with respect to the complex permittivity as a function of position. The Fréchet derivatives are computed in real time using a self-adjoint formulation.

Confocal imaging, also known as synthetic focusing, solves the linearized scattering problem in the spatial domain without matrix inversion as well [22][23]. The method operates on time-domain data and relies on multiple received signals. The strength of a scattering point depends on the coherent summation of its scattered components present in all received signals. The calculations involved are not demanding.

All these linear inversion methods provide fast qualitative estimates of an object's shape and electrical contrast. However, they cannot be used as linearized solvers at the core of nonlinear iterative reconstruction schemes because of their inability to provide a quantitative estimate of the electromagnetic constitutive parameters.

In the past decade, advances have led to two powerful approaches to linear quantitative inversion, specifically developed for microwave imaging based on scattering-parameter data. These two approaches, quantitative microwave holography [24] and scattered-power mapping (SPM) [25][26], rely on a high-fidelity forward model obtained from measurements. The key lies in the experimentally acquired resolvent kernel which properly scales the inversion problem thereby enabling quantitative imaging. For that, the system PSF for each range location has to be measured.

In [25][26], the SPM methodology is derived for the case of planar acquisition surfaces. The RO measurements, carried out as part of the system calibration, provide the baseline data. In order to obtain the system PSF, a second set of calibration measurements is performed with a scattering probe of known electrical properties embedded in the RO. The so-obtained object is referred to as the calibration object (CO). Since the RO is assumed to be homogeneous or layered, which infers a translationally-invariant system, the coordinate translation can be applied. Therefore, a single scan of the CO with a scattering probe at the center of each range plane is sufficient to obtain the system PSF for all points in that plane. However, the coordinate translation proposed in [25][26] requires a four times larger scan area for the CO scan than that for the OUT scan. This makes the system calibration too time consuming and impractical.

Here, we propose two new methods, BCCB SPM and convolution-based SPM, which exploit the key idea of the work in [25][26], but are more general and far more efficient in solving the linear inverse problem. The first important improvement is that the proposed methods employ the localized quasi-linear Rytov (LQLR) approximation, in addition to

also being capable of employing the localized quasi-linear (LQL) model of scattering. The LQLR approximation is subjected to a different set of limitations compared to the LQL approximation; thus, the applicability of the methods is significantly expanded. Second, a new way of building the SPM system matrix is proposed although its physical meaning of being the image PSF remains the same as initially introduced in [25]. This brings two advantages: (i) reduced number of calibration measurements, and (ii) the computational time being a few orders of magnitude less than that in [25][26].

3.2 Block Circulant with Circulant Blocks (BCCB) Scattered-Power Mapping (SPM)

We commence the discussion with the BCCB SPM, the name of which comes from its system matrix being of a particular mathematical structure: block circulant with circulant blocks in the case of 2D imaging or block circulant with BCCB blocks in 3D imaging.

3.2.1 Qualitative Reconstruction

As shown in [25], the closer the relative permittivity contrast of the scattering probe $\delta\varepsilon_{\mathrm{CO}}$ is to the relative permittivity contrast of the OUT $\Delta\varepsilon_{\mathrm{OUT}}(\mathbf{r}')$, the closer the ratio of their respective reflectivity tensors $\lambda_{\mathrm{OUT}}^{(m)}(\mathbf{r}') / \lambda_{\mathrm{CO}}^{(m)}$ is to unity. Assuming that

$$\lambda_{\mathrm{OUT}}^{(m)}(\mathbf{r}') / \lambda_{\mathrm{CO}}^{(m)} \approx 1 \tag{3.1}$$

and discretizing the integral in the data equation (2.21) into a sum over all N_{v} voxels, (2.21) is written in the discrete form:

$$\Delta S^{(m)}_{\mathrm{OUT},n,\mathrm{LQL}}(\mathbf{r}) \approx \sum_{q=1}^{N_\mathrm{v}} \tau_q \Delta S^{(m)}_{\mathrm{CO},n,\mathbf{r}'_q,\mathrm{LQL}}(\mathbf{r}), \tag{3.2}$$

where

$$\tau_q = \Delta\varepsilon_{\mathrm{OUT}}(\mathbf{r}'_q) / \delta\varepsilon_{\mathrm{CO}},\ q = 1,\ldots,N_\mathrm{v}. \tag{3.3}$$

Note that (3.2) is a discretized version of the LQL forward model (2.21) with $\Delta S^{(m)}_{\mathrm{OUT},n,\mathrm{LQL}}(\mathbf{r})$ and $\Delta S^{(m)}_{\mathrm{CO},n,\mathbf{r}'_q,\mathrm{LQL}}$ defined as (see (2.14)):

$$\Delta S^{(m)}_{\mathrm{OUT},n,\mathrm{LQL}}(\mathbf{r}) = S^{(m)}_{\mathrm{OUT},n}(\mathbf{r}) - S^{(m)}_{\mathrm{RO},n}(\mathbf{r}), \tag{3.4}$$

$$\Delta S^{(m)}_{\mathrm{CO},n,\mathbf{r}'_q,\mathrm{LQL}}(\mathbf{r}) = S^{(m)}_{\mathrm{CO},n,\mathbf{r}'_q}(\mathbf{r}) - S^{(m)}_{\mathrm{RO},n}(\mathbf{r}). \tag{3.5}$$

Discretizing the forward model under the LQLR approximation in (2.26), we arrive to an expression similar to (3.2), except for $\Delta S^{(m)}_{\mathrm{OUT},n,\mathrm{LQLR}}(\mathbf{r})$ and $\Delta S^{(m)}_{\mathrm{CO},n,\mathbf{r}'_q,\mathrm{LQLR}}$ defined as follows:

$$\Delta S^{(m)}_{\mathrm{OUT},n,\mathrm{LQLR}}(\mathbf{r}) = S^{(m)}_{\mathrm{RO},n}(\mathbf{r}) \cdot \ln\left[\frac{S^{(m)}_{\mathrm{OUT},n}(\mathbf{r})}{S^{(m)}_{\mathrm{RO},n}(\mathbf{r})}\right], \tag{3.6}$$

$$\Delta S^{(m)}_{\mathrm{CO},n,\mathbf{r}'_q,\mathrm{LQLR}}(\mathbf{r}) = S^{(m)}_{\mathrm{RO},n}(\mathbf{r}) \cdot \ln\left[\frac{S^{(m)}_{\mathrm{CO},n,\mathbf{r}'_q}(\mathbf{r})}{S^{(m)}_{\mathrm{RO},n}(\mathbf{r})}\right]. \tag{3.7}$$

Note that (3.3) stays the same in the case of LQLR approximation.

In the case of the calibration with a metallic scattering probe (see (2.29) and (2.30)), the discretizations of the forward models under the linear Born and Rytov approximations lead to

$$\Delta S^{(m)}_{\mathrm{OUT},n,\mathrm{LB}}(\mathbf{r}) \approx \sum_{q=1}^{N_\mathrm{v}} \tau'_q \left[-\frac{\mathrm{i}3\omega^{(m)}\varepsilon_0 \Delta S^{(m)}_{\mathrm{CO},n,\mathbf{r}'_q,\mathrm{LB}}(\mathbf{r})}{8h\alpha^{(m)}} \right], \tag{3.8}$$

$$\Delta S^{(m)}_{\mathrm{OUT},n,\mathrm{LR}}(\mathbf{r}) \approx \sum_{q=1}^{N_\mathrm{v}} \tau'_q \left[-\frac{\mathrm{i}3\omega^{(m)}\varepsilon_0 \Delta S^{(m)}_{\mathrm{CO},n,\mathbf{r}'_q,\mathrm{LR}}(\mathbf{r})}{8h\alpha^{(m)}} \right]. \tag{3.9}$$

Here, the expressions for $\Delta S^{(m)}_{\mathrm{OUT},n,\mathrm{LB}}$, $\Delta S^{(m)}_{\mathrm{OUT},n,\mathrm{LR}}$, $\Delta S^{(m)}_{\mathrm{CO},n,\mathbf{r}'_q,\mathrm{LB}}$ and $\Delta S^{(m)}_{\mathrm{CO},n,\mathbf{r}'_q,\mathrm{LR}}$ are identical to those in (3.4), (3.6), (3.5) and (3.7), respectively. However, for the calibration with a metallic scattering probe τ'_q is defined as

$$\tau'_q = \Delta\varepsilon_{\mathrm{OUT}}(\mathbf{r}'_q),\ q = 1,\ldots,N_\mathrm{v}. \tag{3.10}$$

Henceforth, for the sake of brevity, all the theory is presented only for the case of the LQL approximation, thus the subscript LQL is omitted. The application of the LQLR approximation as well as the LB and LR approximations in the case of the calibration with a metallic scattering probe follows similar steps.

3.2.1.1 Power Maps

As proposed in [25], the OUT power map is defined as a qualitative measure of the scattering occurring at each pth voxel, $p=1,\ldots,N_\mathrm{v}$. Its value at $\mathbf{r}'_p \in V'$ for the mth

frequency is determined via the CO responses with the scattering probe being at $\mathbf{r}'_p$, i.e., $S^{(m)}_{\mathrm{CO},n,\mathbf{r}'_p}(\mathbf{r})$, $n=1,\ldots,N_\mathrm{r}\cdot N_\mathrm{t}$. Let all responses (both CO and OUT) be measured on a discrete grid over the acquisition surface, where the observation location is indicated by the indices *u* and *v*, i.e., $\mathbf{r}\equiv\mathbf{r}_{uv}$. For example, in a rectangular planar scan of $N_x\cdot N_y$ grid points, $u=1,\ldots,N_x$ and $v=1,\ldots,N_y$. The value of the OUT power map $M^{(m)}_\mathrm{OUT}$ at $\mathbf{r}'_p$ is defined as

$$M^{(m)}_\mathrm{OUT}(\mathbf{r}'_p)=\sum_{n=1}^{N_\mathrm{t}\cdot N_\mathrm{r}}\sum_{u=1}^{N_x}\sum_{v=1}^{N_y}\Delta S^{(m)}_{\mathrm{OUT},n}(\mathbf{r}_{uv})\cdot\left[\Delta S^{(m)}_{\mathrm{CO},n,\mathbf{r}'_p}(\mathbf{r}_{uv})\right]^*,\ p=1,\ldots,N_\mathrm{v}. \tag{3.11}$$

Note that (3.11) can produce a qualitative OUT image very fast without solving any systems of equations. Analogously to the OUT power map, the CO power map is defined as

$$M^{(m)}_{\mathrm{CO},q}(\mathbf{r}'_p)=\sum_{n=1}^{N_\mathrm{t}\cdot N_\mathrm{r}}\sum_{u=1}^{N_x}\sum_{v=1}^{N_y}\Delta S^{(m)}_{\mathrm{CO},n,\mathbf{r}'_q}(\mathbf{r}_{uv})\cdot\left[\Delta S^{(m)}_{\mathrm{CO},n,\mathbf{r}'_p}(\mathbf{r}_{uv})\right]^*,\quad q=1,\ldots,N_\mathrm{v},\ p=1,\ldots,N_\mathrm{v}. \tag{3.12}$$

Here, *q* denotes the voxel with a scattering probe in it. When $p=q$, (3.12) becomes

$$M^{(m)}_{\mathrm{CO},p}(\mathbf{r}'_p)=\sum_{n=1}^{N_\mathrm{t}\cdot N_\mathrm{r}}\sum_{u=1}^{N_x}\sum_{v=1}^{N_y}\left|\Delta S^{(m)}_{\mathrm{CO},n,\mathbf{r}'_p}(\mathbf{r}_{uv})\right|^2. \tag{3.13}$$

The power maps are pivotal in the SPM method, hence its name. The value of a power map at $\mathbf{r}'_p$ (see (3.11) or (3.12)) provides a measure of the similarity between the OUT responses and those of the CO obtained with the scattering probe at $\mathbf{r}'_p$. This measure

corresponds to a cross-correlation in the time domain. On the other hand, the CO power map value at $\mathbf{r}'_p$, when the scattering probe is at $\mathbf{r}'_p$, represents the maximum attainable scattered power among all voxels; see (3.13), which is expressed as the sum of the autocorrelations of all responses.

3.2.1.2 Application to Frequency-Swept Data

Often, microwave imaging employs multi-frequency data. In this case, the multi-frequency power maps are added after the following normalization procedure [25][27]:

$$M_{\mathrm{OBJ}}(\mathbf{r}'_p) = \frac{1}{N_f}\sum_{m=1}^{N_f} \frac{\left|M_{\mathrm{OBJ}}^{(m)}(\mathbf{r}'_p)\right|}{\eta^{(m)}} \cdot e^{\mathrm{i}\angle M_{\mathrm{OBJ}}^{(m)}(\mathbf{r}'_p)}, \tag{3.14}$$

where $\eta^{(m)}$ is the maximum magnitude value of the CO power map at the *m*th frequency:

$$\eta^{(m)} = \max\left(\left|M_{\mathrm{CO},q}^{(m)}(\mathbf{r}'_p)\right|\right). \tag{3.15}$$

The normalization strategy in (3.14) preserves the phase of each single-frequency power map. The normalization factor $\eta^{(m)}$ in (3.14) can be calculated using strategies alternative to (3.15), e.g., using the energy normalization [20]. However, (3.15) offers simpler implementation and faster computation [27].

3.2.2 Quantitative Reconstruction

Substituting (3.2) into (3.11) leads to a linear system of equations in the unknown contrast distribution τ_q, $q = 1,...,N_{\mathrm{v}}$, which is explicitly written as

$$M_{\mathrm{OUT}}^{(m)}(\mathbf{r}'_p)=\sum_{n=1}^{N_{\mathrm{t}}N_{\mathrm{r}}}\sum_{q=1}^{N_{\mathrm{v}}}\sum_{u=1}^{N_x}\sum_{v=1}^{N_y}\tau_q\Delta S_{\mathrm{CO},n,\mathbf{r}'_q}^{(m)}(\mathbf{r}_{uv})\cdot\left[\Delta S_{\mathrm{CO},n,\mathbf{r}'_p}^{(m)}(\mathbf{r}_{uv})\right]^*, \quad p=1,\ldots,N_{\mathrm{v}}. \tag{3.16}$$

Employing (3.12) allows for writing (3.16) in a matrix form:

$$\boldsymbol{A}^{(m)}\boldsymbol{\tau} = \boldsymbol{b}^{(m)}, \tag{3.17}$$

where

$$\boldsymbol{A}^{(m)}=\begin{bmatrix} M_{\mathrm{CO},1}^{(m)}(\mathbf{r}'_1) & \cdots & M_{\mathrm{CO},N_{\mathrm{v}}}^{(m)}(\mathbf{r}'_1) \\ \vdots & & \vdots \\ M_{\mathrm{CO},1}^{(m)}(\mathbf{r}'_{N_{\mathrm{v}}}) & \cdots & M_{\mathrm{CO},N_{\mathrm{v}}}^{(m)}(\mathbf{r}'_{N_{\mathrm{v}}}) \end{bmatrix}, \tag{3.18}$$

$$\boldsymbol{\tau} = \begin{bmatrix} \tau_1 & \cdots & \tau_{N_{\mathrm{v}}} \end{bmatrix}^T, \tag{3.19}$$

$$\boldsymbol{b}^{(m)} = \begin{bmatrix} M_{\mathrm{OUT}}^{(m)}(\mathbf{r}'_1) & \cdots & M_{\mathrm{OUT}}^{(m)}(\mathbf{r}'_{N_{\mathrm{v}}}) \end{bmatrix}^T. \tag{3.20}$$

The $N_{\mathrm{v}}\times N_{\mathrm{v}}$ matrix $\boldsymbol{A}^{(m)}$ in (3.17) and (3.18) consists of the CO power maps formed using (3.12). The $N_{\mathrm{v}}\times 1$ vector $\boldsymbol{b}^{(m)}$ contains the OUT power map formed using (3.11). Solving (3.17) for $\boldsymbol{\tau}$ allows to estimate a relative permittivity contrast $\Delta\varepsilon_{\mathrm{OUT}}(\mathbf{r}'_p)$ from (3.3). Finally, an actual relative permittivity distribution of the OUT is obtained from (2.2).

The CO power maps across all frequencies can be combined using (3.14) to form the multi-frequency matrix $\boldsymbol{A}$. Similarly, the vector $\boldsymbol{b}$ can be formed using the frequency-combined OUT power map. The size of the so-obtained linear system of equations

$\boldsymbol{A\tau} = \boldsymbol{b}$ is still $N_{\mathrm{v}} \times N_{\mathrm{v}}$ and it is independent of the number of frequency points. In the case of calibration with dielectric scattering probe, each component of the unknown vector $\boldsymbol{\tau}$ is defined as per (3.3). In the case of the calibration with a metallic scattering probe, it is defined as per (3.10).

3.2.2.1 Planar Coordinate Translation in Fourier Space

If the imaging system is invariant to lateral translations, the experimentally obtained PSF with a scattering probe at the center of the imaged volume can be used to obtain the PSFs at all other lateral positions $\mathbf{r}'_p \in V'$. This can be realized by coordinate translation.

In [25][26], it is suggested to perform the CO scan over an area A_{CO}, which is four times larger than the area A' used to acquire the data for an OUT. This concept is illustrated in Figure 3.1 with two examples of voxels to be imaged. Each element of the square grid indicates a sampling position, which is also an imaged voxel. Figure 3.1(a) and Figure 3.1(c) show the cross-sectional area of the OUT. In Figure 3.1(a), the central voxel P_{center} is highlighted, whereas in Figure 3.1(c), the corner voxel P_{corner} is indicated by a thick line. Figure 3.1(b) and Figure 3.1(d) show the entire area A_{CO} scanned in the calibration (CO) measurement. In this measurement, the scattering probe is fixed at the origin O while the antennas sample the response over A_{CO}. The CO response subset acquired in the area $A'_{P_{\mathrm{center}}}$ (outlined with a solid line in Figure 3.1(b)) is $\Delta S^{(m)}_{\mathrm{CO},n,P_{\mathrm{center}}}(\mathbf{r})$, $\mathbf{r} \in A'_{P_{\mathrm{center}}}$. This is the PSF used to compute the value of the OUT power map at P_{center} with (3.11), wherein $\mathbf{r}'_p \equiv P_{\mathrm{center}}$; see Figure 3.1(a). On the other hand, the CO response

subset $\Delta S^{(m)}_{\mathrm{CO},n,P_{\mathrm{corner}}}(\mathbf{r})$, $\mathbf{r} \in A'_{P_{\mathrm{corner}}}$, acquired in the area $A'_{P_{\mathrm{corner}}}$ (outlined with a solid line in Figure 3.1(d)) is the PSF used to compute the value of the OUT power map at $\mathbf{r}'_p \equiv P_{\mathrm{corner}}$.

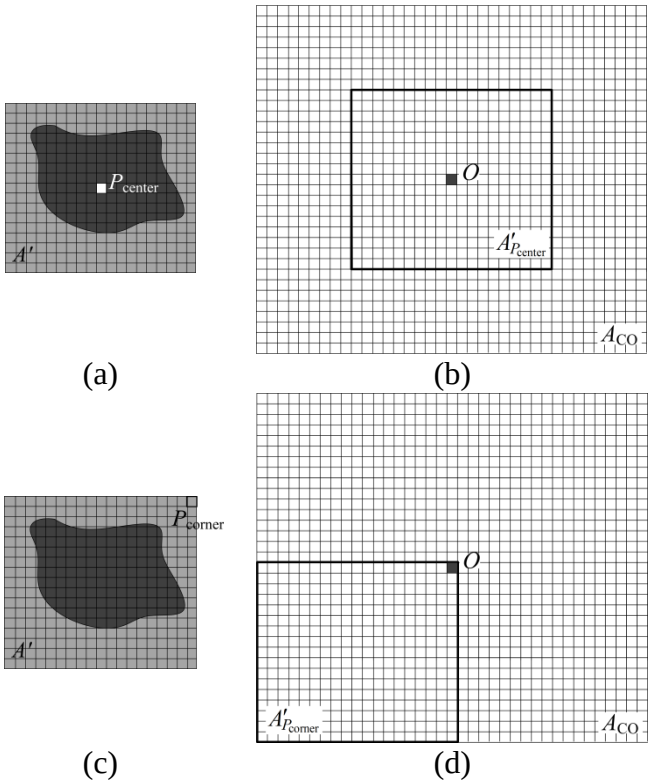

Figure 3.1 Illustration of the measured *S*-parameter data on a square sampling grid: (a) the OUT area A' with an imaged voxel P_{center} at the center; (b) the CO area A_{CO} and its portion $A'_{P_{\mathrm{center}}}$ used to image the voxel P_{center}; (c) the OUT area A' with an imaged voxel P_{corner} at the corner; (d) the CO area A_{CO} and its portion $A'_{P_{\mathrm{corner}}}$ used to image the voxel P_{corner}. The origin of the CO area, which also the position of the scattering probe, is denoted as *O*.

Here, we propose to eliminate the need for four times larger CO scan by exploiting the shift property of the Fourier transform. Let $\mathbf{r}'_0(\bar{z}') \equiv P_{\mathrm{center}}$ denote the center of the fixed range plane $\bar{z}'$ in which the scattering probe resides. Let the PSF shift along x and y

with respect to $\mathbf{r}_0'(\bar{z}')$ be expressed with multiples of the respective sampling steps Δx and Δy as

$$\Delta\mathbf{r}_{uv}(\bar{z}') = (u\Delta x, v\Delta y),\ u = -N_{x,\max},\ldots,N_{x,\max},\ v = -N_{y,\max},\ldots,N_{y,\max}. \tag{3.21}$$

Here, $N_{x,\max}$ and $N_{y,\max}$ are the maximum shifts along *x* and *y*, respectively. Therefore, $N_x = 2N_{x,\max}$ in the case of an even number of samples along *x* whereas $N_x = 2N_{x,\max}+1$ in the case of an odd number of samples along *x*. Analogously, $N_y = 2N_{y,\max}$ in the case of an even number of samples along *y* whereas $N_y = 2N_{y,\max}+1$ in the case of an odd number of samples along *y*.

Then, the values of the shifted PSFs,

$$\Delta S^{(m)}_{\mathrm{CO},n,\mathbf{r}_0'(\bar{z}')-\Delta\mathbf{r}_{uv}'(\bar{z}')}(x,y),\ u = -N_{x,\max},\ldots,N_{x,\max},\ v = -N_{y,\max},\ldots,N_{y,\max}, \tag{3.22}$$

can be obtained from that of $\Delta S^{(m)}_{\mathrm{CO},n,\mathbf{r}_0'(\bar{z}')}(x,y)$ using

$$\Delta S^{(m)}_{\mathrm{CO},n,\mathbf{r}_0'(\bar{z}')-\Delta\mathbf{r}_{uv}'(\bar{z}')}(x,y) = \mathcal{F}_{2\mathrm{D}}^{-1}\left\{\mathcal{F}_{2\mathrm{D}}\left\{\Delta S^{(m)}_{\mathrm{CO},n,\mathbf{r}_0'(\bar{z}')}(x,y)\right\}e^{-\mathrm{i}k_x u\Delta x}e^{-\mathrm{i}k_y v\Delta y}\right\}. \tag{3.23}$$

Here, k_x and k_y are the Fourier variables corresponding to x and y, respectively. With this approach, the CO scan area matches that of the OUT.

3.2.2.2 Solving BCCB Linear System of Equations

Utilizing the *k*-space coordinate translation has yet another advantage – the SPM system matrix $\boldsymbol{A} \in \mathbb{C}^{N_\mathrm{v} \times N_\mathrm{v}}$, $N_\mathrm{v} = N_x N_y$ becomes block circulant with circulant blocks, or BCCB. When the number of range samples N_z is larger than one (3D imaging), we have $N_\mathrm{v} = N_x N_y N_z$ and the matrix $\boldsymbol{A}$ becomes block circulant with BCCB blocks. We emphasize that the calibration object in either case does not have to be symmetrical $(N_x \neq N_y)$. If $\boldsymbol{A}$ is block circulant with BCCB blocks (which is the most general case), the following holds [28][29]

$$\boldsymbol{A} = \boldsymbol{F}^{-1} \operatorname{diag}(\mathbf{vec}(\hat{\boldsymbol{a}}))\, \boldsymbol{F}\,, \tag{3.24}$$

where the Fourier matrix $\boldsymbol{F} \in \mathbb{C}^{N_\mathrm{v} \times N_\mathrm{v}}$ is found from the Kronecker tensor product $\boldsymbol{F} = \boldsymbol{F}_z \otimes \boldsymbol{F}_y \otimes \boldsymbol{F}_x$ ("outside" to "inside" order) with $\boldsymbol{F}_z$, $\boldsymbol{F}_y$ and $\boldsymbol{F}_x$ being Fourier matrices [29] of size $N_z \times N_z$, $N_y \times N_y$ and $N_x \times N_x$, respectively. The linear operator $\mathbf{vec}: \mathbb{C}^{N_x \times N_y \times N_z} \to \mathbb{C}^{N_\mathrm{v}}$ produces a vector by stacking the columns of $\hat{\boldsymbol{a}}$, where the components of $\hat{\boldsymbol{a}}$ are the eigenvalues of $\boldsymbol{A}$ found from

$$\hat{\boldsymbol{a}} = \sqrt{N_\mathrm{v}}\, \mathcal{F}_{2\mathrm{D}(3\mathrm{D})} \left\{ \mathbf{array}\left(\boldsymbol{a}\right) \right\}. \tag{3.25}$$

Here, the symbol $\mathbf{array}: \mathbb{C}^{N_\mathrm{v}} \to \mathbb{C}^{N_x \times N_y \times N_z}$ denotes the inverse of the **vec** operator, whereas $\boldsymbol{a}$ is the first column of $\boldsymbol{A}$. Also, since the Fourier matrix $\boldsymbol{F}$ is unitary, its inverse in (3.24) is readily calculated using the adjoint matrix $\boldsymbol{F}^\dagger$ as

$$\boldsymbol{F}^{-1} = \left(N_\mathrm{v}\right)^{-1} \boldsymbol{F}^\dagger. \tag{3.26}$$

From (3.24) it follows that there is no need to construct the whole matrix of CO power maps as per (3.18). Furthermore, nonsingular BCCB systems can be solved using the following recipe [29]:

$$\boldsymbol{\tau} = \mathbf{vec}\left(\mathcal{F}_{2\,\mathrm{D(3D)}}^{-1}\left\{\mathcal{F}_{2\,\mathrm{D(3D)}}\left\{\mathbf{array}(\boldsymbol{b})\right\}./\,\hat{\boldsymbol{a}}\right\}\right), \tag{3.27}$$

where "./" means component-wise division of the 2D (or 3D) arrays.

Note that the solution $\boldsymbol{\tau}$ in (3.27) is obtained only from the first column of $\boldsymbol{A}$. Utilizing 2D (or 3D) Fast Fourier transform (FFT) in (3.27) allows to solve the system of equations (3.17) at a $O(N_{\mathrm{v}}\log(N_{\mathrm{v}}))$ cost. Thus, there is no need to invert a matrix at the typical cost of $O(N_{\mathrm{v}}{}^3)$. There is no need to perform a matrix-vector multiplication either at a $O(2N_{\mathrm{v}})$ cost.

Moreover, due to the ill-posed nature of an inverse problem, the matrix $\boldsymbol{A}$ is usually ill-conditioned. Convergence rates for solution schemes based on the conjugate-gradient method depend on the singular values of $\boldsymbol{A}$. Such solvers typically take a long time to reach a solution. On the other hand, the solution with (3.27) is not affected by ill-conditioning: being expedited by the 2D (or 3D) FFT, it is performed in real time. This is possible due to the advantage of having the BCCB structure. Finally, we remark that Tikhonov regularization is applicable with the BCCB system. It results in a system that can be solved directly using 2D (or 3D) FFTs without computational overhead in a manner similar to (3.27) [29].

3.2.3 Pros and Cons of BCCB SPM

BCCB SPM is proposed as a direct inversion method for fast quantitative imaging. It accommodates a forward model of scattering cast either as a linearized Born model or as a Rytov model. Two key advantages of the BCCB SPM compared to the work reported in [25][26] are the computational speed and the reduced area of the calibration scan. These advantages stem from the PSF coordinate translation implemented in the Fourier domain, which leads to the system matrix being of a particular mathematical structure. This feature is exploited to reduce drastically the computational cost from hours to minutes. Note, however, that although fast, BCCB SPM is not a real-time inversion method.

It should be emphasized that the SPM method is not limited to the BCCB solver described by (3.27). Since the system matrix (3.18) can be readily constructed from its first column using (3.24), other solvers (e.g., conjugate-gradient with or without preconditioner) are applicable as well.

Often, the reconstructed images contain some nonphysical values of the relative permittivity. The most straightforward way to resolve the non-physicality problem is to impose the following constraints:

$$\begin{cases} \mathrm{Re}\left(\varepsilon_{\mathrm{OUT}}(\mathbf{r}'_p)\right) \geq 1 \\ \mathrm{Im}\left(\varepsilon_{\mathrm{OUT}}(\mathbf{r}'_p)\right) \leq 0 \end{cases}, \mathbf{r}' \in V'. \tag{3.28}$$

In order to be able to impose these constraints, another solver is needed, e.g., constrained linear least-squares or semidefinite programming. However, constrained solvers might

significantly slow down the solution. Nonetheless, the freedom of choosing the solver is one of the biggest advantages of the BCCB SPM.

3.3 Convolution-Based SPM

Since we operate with frequency-domain data acquired on planar surfaces, the CO and OUT scattered responses at each frequency are functions of x and y. As per (2.5), for an imaging system which is translationally invariant in the lateral directions, the PSFs at all locations of the scattering probe in a plane $z' = z_0$ can be obtained from the one at the plane's center as

$$\Delta S^{(m)}_{\mathrm{CO},n,\mathbf{r}'_p}(x, y \mid z_0) = \Delta S^{(m)}_{\mathrm{CO},n,\mathbf{r}'_0}\left(x-(x'_p - x'_0), y-(y'_p - y') \mid z_0\right). \tag{3.29}$$

Substituting (3.29) into (2.21), we notice that the integral is a 2D convolution of two functions

$$\Delta S^{(m)}_{\mathrm{OUT},n}(x, y) = \frac{1}{\Omega_{\mathrm{v}}} \int_z \left[\tau(x', y' \mid z') \otimes \Delta S^{(m)}_{\mathrm{CO},n,\mathbf{r}'_0}(x', y' \mid z') \right] dz', \tag{3.30}$$

where $\tau(\mathbf{r}') = \Delta\varepsilon_{\mathrm{OUT}}(\mathbf{r}') / \delta\varepsilon_{\mathrm{CO}}$ is the unknown contrast function, whereas the operator $\otimes$ represents a 2D convolution over x' and y' at each z' plane. Thus, having estimated the system PSF and having measured the OUT, the 3D image can be reconstructed slice by slice by deconvolution. Linear deconvolution methods offer the fastest and the simplest choice when computing the unknown τ in (3.30). These algorithms employ some form of the linear reconstruction filter in a single step. The classical inverse filter, the pseudo-

inverse filter, the Wiener filter, the constrained least-squares filter and the Tikhonov-Miller inversion belong to this group of methods [30]-[34].

3.3.1 Linear Deconvolution in Fourier Space

In this thesis, we demonstrate the most straightforward method of deconvolution, which is performed in Fourier space. This method is also known as classical inverse filter [30][32].

The coordinate translation described for the CO scattered responses also holds for the CO power maps. Thus, (3.16) can be represented as (see (3.30)):

$$\tilde{M}_{\mathrm{OUT},n}(k_x,k_y \mid z') = \frac{\Delta\Omega'}{\Omega_{\mathrm{v}}}\sum_{j=1}^{N_z}\tilde{\tau}(k_x,k_y \mid \xi_j)\cdot\tilde{M}_{\mathrm{CO},n@(0,0,\xi_j)}(k_x,k_y \mid z'), \qquad (3.31)$$

where $n=1,\ldots,N_{\mathrm{t}}N_{\mathrm{r}}$ and the tilde denotes the 2D Fourier transform of the OUT or CO multi-frequency power map, whereas $\Delta\Omega'=\Delta x'\Delta y'\Delta z'$ is the voxel's volume with $\Delta x'$, $\Delta y'$, $\Delta z'$ being the discrete steps along *x*, *y* and *z*, respectively, in the imaged volume. N_z is the number of imaged range locations.

Equation (3.31) allows formulating a square linear system of equations at each point in Fourier space $\boldsymbol{\kappa}=(k_x,k_y)$ as

$$\begin{bmatrix}\boldsymbol{M}_1(\boldsymbol{\kappa})\\ \vdots \\ \boldsymbol{M}_{(N_{\mathrm{t}}N_{\mathrm{r}})}(\boldsymbol{\kappa})\end{bmatrix}_{(N_{\mathrm{t}}N_{\mathrm{r}})\times N_z}\cdot\boldsymbol{x}(\boldsymbol{\kappa})=\begin{bmatrix}\boldsymbol{m}_1(\boldsymbol{\kappa})\\ \vdots \\ \boldsymbol{m}_{(N_{\mathrm{t}}N_{\mathrm{r}})}(\boldsymbol{\kappa})\end{bmatrix}_{(N_{\mathrm{t}}N_{\mathrm{r}})}, \qquad (3.32)$$

where the following notations are introduced

$$\boldsymbol{x}(\boldsymbol{\kappa}) = \frac{\Delta\Omega}{\Omega_{\mathrm{v}}}\left[\tilde{\tau}(\boldsymbol{\kappa}, z_1')\cdots\tilde{\tau}(\boldsymbol{\kappa}, z_{N_z}')\right]^T, \tag{3.33}$$

$$\boldsymbol{m}_n(\boldsymbol{\kappa}) = \left[\tilde{M}_{\mathrm{OUT},n}(\boldsymbol{\kappa}, z_1')\cdots\tilde{M}_{\mathrm{OUT},n}(\boldsymbol{\kappa}, z_{N_z}')\right]^T, \tag{3.34}$$

$$\boldsymbol{M}_n(\boldsymbol{\kappa}) = \begin{bmatrix} \tilde{M}_{\mathrm{CO},n@(0,0,z_1')}(\boldsymbol{\kappa}, z_1') & \cdots & \tilde{M}_{\mathrm{CO},n@(0,0,z_{N_z}')}(\boldsymbol{\kappa}, z_1') \\ \tilde{M}_{\mathrm{CO},n@(0,0,z_1')}(\boldsymbol{\kappa}, z_2') & \cdots & \tilde{M}_{\mathrm{CO},n@(0,0,z_{N_z}')}(\boldsymbol{\kappa}, z_2',) \\ \vdots & \ddots & \vdots \\ \tilde{M}_{\mathrm{CO},n@(0,0,z_1')}(\boldsymbol{\kappa}, z_{N_z}') & \cdots & \tilde{M}_{\mathrm{CO},n@(0,0,z_{N_z}')}(\boldsymbol{\kappa}, z_{N_z}') \end{bmatrix}_{N_z\times N_z}. \tag{3.35}$$

Once we have $\tilde{\tau}(\boldsymbol{\kappa}, z')$ for $\forall\boldsymbol{\kappa}$ and for $\forall z'$, the frequency-combined 3D ratio contrast is recovered via 2D inverse Fourier transform slice by slice:

$$\tau(x', y' \mid z_l') = F_{2\mathrm{D}}^{-1}\left\{\tilde{\tau}(\boldsymbol{\kappa}, z_l')\right\},\ z_l' = z_1', \ldots, z_{N_z}'. \tag{3.36}$$

Finally, the relative complex permittivity of the OUT is found from

$$\varepsilon_{\mathrm{OUT}}(x', y' \mid z_l') = \varepsilon_{\mathrm{RO}}(x', y' \mid z_l') + \delta\varepsilon_{\mathrm{CO}} \cdot \tau(x', y' \mid z_l'). \tag{3.37}$$

Note that a similar methodology has been implemented in another linear inversion method, quantitative microwave holography (QMH) [24]. However, the distinct feature of QMH is that its linear system of equations is formulated directly in terms of the scattered CO and OUT responses (see (3.30)) as

$$\begin{bmatrix} \boldsymbol{A}_1(\boldsymbol{\kappa}) \\ \vdots \\ \boldsymbol{A}_{(N_\mathrm{t}N_\mathrm{r})}(\boldsymbol{\kappa}) \end{bmatrix}_{(N_\mathrm{t}N_\mathrm{r}N_f)\times N_z} \cdot \boldsymbol{x}(\boldsymbol{\kappa}) = \begin{bmatrix} \boldsymbol{b}_1(\boldsymbol{\kappa}) \\ \vdots \\ \boldsymbol{b}_{(N_\mathrm{t}N_\mathrm{r}N_f)}(\boldsymbol{\kappa}) \end{bmatrix}_{(N_\mathrm{t}N_\mathrm{r}N_f)}, \tag{3.38}$$

where

$$\boldsymbol{b}_n(\boldsymbol{\kappa}) = \left[\Delta\tilde{S}_{\mathrm{OUT},n}{}^{(1)}(\boldsymbol{\kappa}) \cdots \Delta\tilde{S}_{\mathrm{OUT},n}{}^{(N_f)}(\boldsymbol{\kappa}) \right]^T, \tag{3.39}$$

$$\boldsymbol{x}(\boldsymbol{\kappa}) = \frac{\Delta\Omega}{\Omega_\mathrm{v}} \left[\tilde{\tau}(\boldsymbol{\kappa}, z_1') \cdots \tilde{\tau}(\boldsymbol{\kappa}, z_{N_z}') \right]^T, \tag{3.40}$$

$$\boldsymbol{A}_n(\boldsymbol{\kappa}) = \begin{bmatrix} \Delta\tilde{S}_{\mathrm{CO},n@(0,0,z_1')}(\boldsymbol{\kappa}, f_1) & \cdots & \Delta\tilde{S}_{\mathrm{CO},n@(0,0,z_{N_z}')}(\boldsymbol{\kappa}, f_1) \\ \Delta\tilde{S}_{\mathrm{CO},n@(0,0,z_1')}(\boldsymbol{\kappa}, f_2) & \cdots & \Delta\tilde{S}_{\mathrm{CO},n@(0,0,z_{N_z}')}(\boldsymbol{\kappa}, f_2) \\ \vdots & \ddots & \vdots \\ \Delta\tilde{S}_{\mathrm{CO},n@(0,0,z_1')}(\boldsymbol{\kappa}, f_{N_f}) & \cdots & \Delta\tilde{S}_{\mathrm{CO},n@(0,0,z_{N_z}')}(\boldsymbol{\kappa}, f_{N_f}) \end{bmatrix}_{N_f \times N_z}. \tag{3.41}$$

It can be shown that $\boldsymbol{A}_n^\dagger \boldsymbol{A}_n \boldsymbol{x} = \boldsymbol{A}_n^\dagger \boldsymbol{b}_n$ (see (3.38)) is equivalent to the system $\boldsymbol{M}_n \boldsymbol{x} = \boldsymbol{m}_n$ (see (3.32)). Since the data $\boldsymbol{b}_n$ may not be entirely in the range of the forward operator represented by $\boldsymbol{A}_n$, the direct solution of $\boldsymbol{A}_n \boldsymbol{x} = \boldsymbol{b}_n$ may not exist. On the other hand, under the same conditions, $\boldsymbol{A}_n^\dagger \boldsymbol{A}_n \boldsymbol{x} = \boldsymbol{A}_n^\dagger \boldsymbol{b}_n$ may have a solution and it would minimize the least-square error of $\boldsymbol{A}_n \boldsymbol{x} = \boldsymbol{b}_n$ [17][23]. This argument also speaks in favor of obtaining the PSFs experimentally, which ensures that the system matrix $\boldsymbol{M}_n$ provides the physically correct functional space encompassing all possible responses acquired with the particular imaging setup. Lastly, note that the matrix $\boldsymbol{A}_n^\dagger \boldsymbol{A}_n$ has not been used explicitly in neither the BCCB SPM nor the convolution-based SPM.

3.3.2 Pros and Cons of Convolution-Based SPM

A new method referred to as the convolution-based SPM, is proposed. Compared to the BCCB SPM, the convolution-based SPM inversion procedure is performed in Fourier space. Being computationally simple, the method offers real-time reconstruction. However, the linear deconvolution implemented through a classical inverse filter has disadvantages. First, it fails if the matrix $\boldsymbol{M}$ (see (3.32)) is singular or if there are zeros in the system PSF. This disadvantage can be counteracted with regularization schemes [31]. Second, even small levels of noise are significantly amplified by the inversion of very small values in $\boldsymbol{M}_n(\boldsymbol{\kappa})$, which results in reconstruction artifacts [30]. Using another linear deconvolution method, such as the Wiener filter or the constrained least-squares filter is recommended to alleviate the discussed disadvantages [30][33].

Finally, within the proposed inversion procedure in Fourier space, the convolution-based SPM cannot incorporate physicality constraints as per (3.28). Thus, the reconstructed images may contain nonphysical values of the relative permittivity. Such nonphysical values in the resultant images typically have a structure similar to those found in emission tomography [35]: in the neighborhood of a pixel with a large negative (nonphysical) value, there are a number of surrounding pixels where the solution is relatively large and positive. Since in the weak-scattering problems, the reconstructed images are relatively flat with limited high-frequency activity, it is suggested to use the constrained least-squares filter [30][33][35]. It minimizes the amount of high-pass energy in the reconstructed image, thereby ensuring the smoothness of the solution.

3.4 Reconstruction Limitations

The major limitation of the proposed BCCB SPM and convolution-based SPM is their inability to account for the mutual coupling and multiple scattering effects present in the OUT. This limitation is typical for all direct-inversion methods. For example, the reconstruction of a complex object comprised of high-contrast layers with embedded scatterers of varying dielectric permittivity is likely to fail. These limitations stem from the LQL (Born) or LQLR (Rytov) approximations, which linearize the forward model. That is why the proposed methods can be used either in weak-scattering problems or as modules within nonlinear iterative methods such as the Born iterative method [36] and the distorted Born iterative method [37].

The calibration strategy employing a dielectric scattering probe has a significant limitation in tissue imaging. Its quantitative reconstruction accuracy is target-dependent as seen from the assumption (3.1). Since this assumption holds only if $\delta\varepsilon_{\mathrm{CO}} \approx \varepsilon_{\mathrm{OUT}}(\mathbf{r}')$, as the dielectric properties of the inspected object vary with position, the quantitative reconstruction accuracy will also vary from one position to another. Note, however, that the calibration with a metallic scattering probe does not suffer from the aforementioned limitation. Finally, we emphasize that the qualitative reconstruction is target-independent with both calibration strategies.

Also, it should be stressed that if the CO cannot be reconstructed, the OUT would not be imaged either since the CO response represents the PSF of each particular imaging setup. Thus, the size of a scattering probe should be large enough for the imaging system

to detect its response. However, if the scattering probe is not electrically small, the acquired responses do not represent well the system PSFs and the reconstruction is likely to fail or, at least, be quantitatively inaccurate. That is why, the recommended lateral size of a dielectric scattering probe is smaller than $\lambda_{\min,CO}/4$, where $\lambda_{\min,CO}$ is the shortest wavelength inside the CO. As for the vertical dimension, it should be approximately the same as the thickness of the measured spatial step along the range. In case of a metallic scattering probe, the recommended length and diameter of the wire are $\lambda_{\min,CO}/8$ and $\lambda_{\min,CO}/400$, respectively.

As a final remark, note that increasing the number of the independent responses improves the SPM (BCCB SPM and convolution-based SPM) robustness to noise, i.e., imaging is successful with lower data signal-to-noise ratio. This is achieved by increasing the number of the transmitters, the receivers and the frequency samples [20][21][25]. The improved robustness to noise is due to the fact that the SPM qualitative maps are, in essence, plots of the cross-correlation of the OUT data with the system PSF. The cross-correlation peaks at voxels where scattering occurs. Moreover, with multiple data sets, these peaks add coherently. In contrast, at voxels void of scatterers, the cross-correlation values across the data sets add incoherently thus enhancing the image signal-to-noise ratio.

References

[1] M. Born and E. Wolf. *Principles of Optics*. New York: Pergamon, 1980.

[2] M. Nieto-Vesperinas. *Scattering and Diffraction in Physical Optics*. New York: John Wiley, 1991.

[3] J. B. Keller, "Accuracy and validity of the Born and Rytov approximations," *J. Opt. Soc. Am.*, vol. 59, no. 8, pp. 1003–1004, 1969.

[4] M. I. Sancer and A. D. Varvatsis, "A comparison of the Born and Rytov methods," *Proc. IEEE*, vol. 58, no. 1, pp. 140–141, Jan. 1970.

[5] T. M. Habashy, R. W. Groom, and B. R. Spies, "Beyond the Born and Rytov approximations: a nonlinear approach to electromagnetic scattering," *J. Geophys. Res.*, vol. 98, no. B2, pp. 1759–1775, Feb. 1993.

[6] A. Abubakar and T. M. Habashy, "A Green function formulation of the extended Born approximation for three-dimensional electromagnetic modelling," *Wave Motion*, vol. 41, no. 3, pp. 211–227, Mar. 2005.

[7] M. S. Zhdanov and E. Tartaras, "Three-dimensional inversion of multitransmitter electromagnetic data based on the localized quasi-linear approximation," *Geophys. J. Int.*, vol. 148, pp. 506–519, Mar. 2002.

[8] E. J. Feleppa, "Holography and medicine," *IEEE Trans. Biomed. Eng.*, vol. BME-19, no. 3, pp. 194–205, May 1972.

[9] N. Farhat, "Microwave holography and coherent tomography," *Medical Applications of Microwave Imaging*, pp. 66–81, 1986.

[10] M. Elsdon, D. Smith, M. Leach, and S. Foti, "Experimental investigation of breast tumor imaging using indirect microwave holography," *Microw. Optical Technology Lett.*, vol. 48, no. 3, pp. 480–482, 2006.

[11] R. K. Amineh, A. Khalatpour, H. Xu, Y. Baskharoun, and N. K. Nikolova, "Three-dimensional near-field microwave holography for tissue imaging," *Int. J. Biomed. Imag.*, vol. 2012, 11 pp., 2012.

[12] L. Wang, R. Simpkin, and A. Al-Jumaily, "Holographic microwave imaging for medical applications," *J. Biomed. Sci. Eng.*, vol. 6, pp. 823–833, Aug. 2013.

[13] O. Mudanyali *et al*., "A microwave tomographic approach for nondestructive testing of dielectric coated metallic surfaces," *IEEE Geosci. Rem. Sens. Lett.*, vol. 5, no. 2, pp. 180–184, Apr. 2008.

[14] J. C. Bolomey, A. Izadnegahdar, L. Jofre, C. Pichot, G. Peronnet, and M. Solaimani, "Microwave diffraction tomography for biomedical applications," *IEEE Trans. Microw. Theory Techn.*, vol. 30, no. 11, pp. 1998–2000, Nov. 1982.

[15] F. J. Paoloni, "Implementation of microwave diffraction tomography for measurement of dielectric constant distribution," *IEE Proceedings H – Microwaves, Antennas and Propagation*, vol. 134, no. 1, pp. 25–29, Feb. 1987.

[16] P. M. Meaney, M. W. Fanning, D. Li, S. P. Poplack, and K. D. Paulsen, "A clinical prototype for active microwave imaging of the breast," *IEEE Trans. Microw. Theory Techn.*, vol. 48, no. 11, pp. 1841–1853, Nov. 2000.

[17] A. J. Devaney. *Mathematical Foundations of Imaging, Tomography and Wavefield Inversion*. Cambridge, UK: Cambridge University Press, 2012.

[18] M. Slaney, A. C. Kak, and L. E. Larsen, "Limitations of imaging with first-order diffraction tomography," *IEEE Trans. Microw. Theory Thechn.*, vol. MTT-32, no. 8, pp. 860–874, Aug. 1984.

[19] W. C. Chew. *Waves and Fields in Inhomogeneous Media*. Piscataway, NJ: IEEE Press, 1995 (reprint).

[20] L. Liu, A. Trehan, and N. K. Nikolova, "Near-field detection at microwave frequencies based on self-adjoint response sensitivity analysis," *Inverse Problems*, vol. 26, no. 10, 28 pp., Aug. 2010.

[21] Y. Zhang, S. Tu, R. K. Amineh, and N. K. Nikolova, "Microwave sensitivity-based imaging with data acquired on cylindrical surfaces: resolution and robustness to noise," *Inverse Problems*, vol. 28, no. 11, 15 pp., Oct. 2012.

[22] N. K. Nikolova, "Microwave biomedical imaging," *Wiley Encyclopedia of Electrical and Electronics Engineering*, pp. 1–22. (published online Apr. 25, 2014).

[23] M. Pastorino. *Microwave Imaging*. Hoboken, NJ: Wiley, 2010.

[24] D. Tajik, J. Thompson, A. S. Beaverstone, and N. K. Nikolova, "Real-time quantitative reconstruction based on microwave holography," *IEEE AP-S/URSI Int. Symp. on Antennas and Propag*., Fajardo, Puerto Rico, pp. 851–852, Jun. 2016.

[25] S. Tu, J. J. McCombe, D. S. Shumakov, and N. K. Nikolova, "Fast quantitative microwave imaging with resolvent kernel extracted from measurements," *Inverse Problems*, vol. 31, no. 4, 33 pp., Mar. 2015.

[26] D. S. Shumakov, S. Tu, and N. K. Nikolova, "Fast quantitative microwave imaging based on measured point spread functions and inversion in real space," *IEEE AP-S/URSI Int. Symp. Antennas Propag*., pp. 687–688, Jul. 2015.

[27] D. S. Shumakov, "Comparison of multi-frequency PSF normalization strategies," CEM-R-76, McMaster University, Canada, Jul. 2016.

[28] P. J. Davis, "Circulant matrices," in *Circulant Matrices*. New York: Wiley, 1979, pp. 66–189.

[29] C. R. Vogel, "Image deblurring," in *Computational Methods for Inverse Problems*. Philadelphia, PA: SIAM, 2002, pp. 64–76.

[30] D. S. C. Biggs, *Accelerated Iterative Blind Deconvolution*. PhD Thesis. University of Auckland, New Zealand, Dec. 1998, pp. 18–23.

[31] T. G. Savelyev and A. G. Yarovoy, "Fast imaging by 3-D deconvolution in short-range UWB radar for concealed weapon detection," *Proceedings of the 9th European Radar Conference (2012 EuMA)*, Amsterdam, The Netherlands, pp. 26–29, 31 Oct. – 2 Nov. 2012.

[32] F. Yano and S. Nomura, "Deconvolution of scanning electron microscopy images," *Scanning*, vol. 15, no. 1, pp. 19–24, 1993.

[33] M. R. Banham and A. K. Katsaggelos, "Digital image restoration," *IEEE Sign. Proc. Mag.*, vol. 14, no. 2, pp. 24–41, Mar. 1997.

[34] G. M. P. van Kempen, H. T. M. van der Voort, J. G. J. Bauman, and K. C. Strasters, "Comparing maximum likelihood estimation and constrained Tikhonov-Miller restoration," *IEEE Eng. Med. Biol. Mag.*, vol. 15, no. 1, pp. 76–83, Jan/Feb 1996.

[35] F. O'Sullivan, Y. Pawitan, and D. Haynor, "Reducing negativity artifacts in emission tomography: post-processing filtered backprojection solutions," *IEEE Trans. Medical Imaging*, vol. 12, no. 4, pp. 653–663, Dec. 1993.

[36] Y. M. Wang and W. C. Chew, "An iterative solution of the two-dimensional electromagnetic inverse scattering problem," *Int. J. Imaging Syst. Technol.*, vol. 1, no. 1, pp. 100–108, 1989.

[37] R. F. Remis and P. M. van den Berg, "On the equivalence of the Newton-Kantorovich and distorted Born methods," *Inverse Problems*, vol. 16, no. 1, 4 pp., Feb. 2000.

Chapter 4

De-noising Algorithm Enhancing Microwave Imaging

4.1 Introduction

The physical assessment of the imaging system aims at determining the quality of the data before they are processed to produce an image. The raw-data quality is critical for the final image fidelity and it can be assessed independently from the reconstruction or the image-processing algorithms. It is desirable to be able to quantify the physical merits of the data-acquisition hardware through common metrics [1][2]. For example, one such metric, the data signal-to-noise ratio (SNR), has a fundamental relationship with detectability. The Rose Criterion states that if SNR is larger than 5, the signal region will be detectable in most situations, but that detection performance continuously degrades as SNR approaches zero [2].

In microwave imaging, there is no agreed-upon approach to evaluate the SNR of the measured data or the images [3]-[7]. In [8], an approach to the data SNR estimation was proposed based on the measurement of a known object. However, it does not account for a scenario where the interference pattern in the measured two-dimensional (2D) data exceeds the so-called “exclusion zone” (the 2D region where the antenna aperture

contains the scatterer's lateral position). The de-noising method proposed here estimates the noise component of the data without the need to define an exclusion zone and is, therefore, independent of the scattered-field pattern at the acquisition surface. Thus, it offers a rigorous method to evaluate the SNR of a data set and the dynamic range of the particular acquisition system. More importantly, having the de-noised data is beneficial in image reconstruction [9][10] minimizing the need to employ case-specific filtering and regularization.

In signal processing, the extraction of the signal from noisy data is a long-standing problem [11]-[13]. The signals are usually dependent on a single variable, e.g., time. In the case of microwave imaging, raw frequency-sweep data are usually comprised of *S*-parameters that depend on the sampling location, e.g., (x, y) in planar scanning. Also, the *S*-parameters are complex. Here, an approach is introduced to separate the signal from the noise and positioning uncertainties in a complex-valued 2D data set at each sampled frequency.

In extracting the noise from the data, the proposed algorithm uses an iterative sifting procedure similar to the method of empirical mode decomposition (EMD). EMD was first developed to decompose a signal into intrinsic mode functions (IMFs) [14]. Later, EMD-based filtering of 1D time-domain signals was proposed for noise suppression [15][16]. Our method, however, does not perform data decomposition into IMFs. Unlike EMD, it extracts only one IMF through a single sifting iterative loop. This IMF estimates the noise, which is assumed to be uncorrelated to the signal content of the data. This assumption leads to a stopping criterion, which differs from that used in the EMD.

Moreover, the signal component is *not* represented as a sum of IMFs as in [15][16]. Thus, the algorithm is conceptually different from EMD despite the similarities in the sifting iterations. It is a novel effective 2D de-noising technique tailored to imaging applications. An important advantage compared with EMD-based noise reduction [15][16] is its superior speed, necessary for the real-time image reconstruction.

The de-noising algorithm is validated with complex-valued 2D data obtained from the microwave measurements of known objects. One such object is the reference object (RO), consisting of the background medium and the measurement setup (e.g., antennas, cables, enclosure, scanning mechanism, etc.). It serves as a host for the measured objects under test (OUT). The RO characterization is therefore an important part of the system calibration. In general, the raw image of the RO data features an interference pattern which varies relatively slowly in space. Another known object used here is the calibration object (CO) [17][18]. It consists of an electrically-small scatterer (dielectric scattering probe) embedded in the background. The CO interference pattern resembles a spherical wave which may or may not have discontinuities. The spacing between the ripples of this pattern remains relatively constant throughout an image and depends on the wavelength. Therefore, the performance of an ideal de-noising algorithm would not depend on the spatial variations of the interference pattern.

The proposed applications not only validate the algorithm but also show how it can be used to estimate the imaging system's SNR and dynamic range. Note that *a priori* knowledge of the scanned object is not required.

4.2 Algorithm Description

4.2.1 Trend and Noise Components

Similar to the EMD procedure, our de-noising algorithm starts with identifying all the local extrema in the 2D data. Interpolation of the maxima and minima returns two surfaces (2D envelopes) between which all other data points reside. The arithmetic mean of the two surfaces is the *trend* data set. The trend is then subtracted from the original data to produce the *residual* data, containing remaining information plus noise. This process iterates, applying the same trend extraction to the residual data. Meanwhile, the trend data sets taken from each iteration are added together to estimate the data signal component. The iterations terminate when a stopping criterion is satisfied. The final residual estimates the data noise component. For microwave imaging involving complex-valued data, the algorithm is applied separately to the real and imaginary parts of the *S*-parameters at each frequency.

Note that the trend components contain the relatively low spatial-frequency information, representing the scattering signal used in the image reconstruction. On the other hand, the extracted noise is characterized by the highest spatial frequencies. This physical interpretation of the trend and noise components is different from EMD [14]-[16], where the trend subtraction is used to extract the IMFs that represent the oscillation modes embedded in the data. The oscillation modes are of interest in the EMD method. In contrast, the trend components are of interest here because their sum defines the estimated signal embedded in the data.

4.2.2 Convergence Criterion

In accordance with the physical meaning of the *trend* and *noise* components, the proposed algorithm converges when the signal component (the sum of all extracted trends) and the noise component (the last residual) are uncorrelated. Thus, at each iteration, the convergence criterion checks the cross-correlation $\text{xcor}^{(i)} = s^{(i)} \star n^{(i)}$ between the signal $(s^{(i)})$ and the noise $(n^{(i)})$. For this purpose, the 99% confidence threshold in the cross-correlation function is used, which is defined as [19]:

$$B = \frac{\zeta_{1-\alpha/2}}{\sqrt{N}}. \tag{4.1}$$

Here, $N = N_x N_y$ is the sample size (N_x, N_y are the sample numbers along *x* and *y*, respectively), $\zeta_{1-\alpha/2} = 2.5758$ ($\alpha = 0.01$) is the 0.99 probability point of the cumulative distribution function of the standard normal distribution. Note that (4.1) depends on the sample size. The convergence criterion requires that $\text{xcor}^{(i)} < B$.

4.2.3 Step-by-Step Procedure

The algorithm can be summarized as follows:

1) Set *i* = 0; initialize signal component, $s^{(0)}(x, y) = 0$.

2) Load input data set $d(x, y)$.

3) Extract the *i*th trend $t^{(i)}(x, y)$ and the *i*th residual $r^{(i)}(x, y) = d(x, y) - t^{(i)}(x, y)$.

4) Update the signal $s^{(i+1)} = s^{(i)} + t^{(i)}$ and the noise $n = r^{(i)}$.

5) If the convergence criterion is satisfied, stop. If not – go to step 3 and use $r^{(i)}$ as input.

4.3 Validation Examples

The de-noising algorithm has been implemented in MATLAB [20]. Local extrema in the 2D data are found with the MATLAB functions *imregionalmin()/imregionalmax()* which are set to 2D minimal connectivity. The 2D extrema interpolations are done with the natural neighbor interpolation method [21]. The MATLAB function *scatteredInterpolant()* with an option *natural* is used.

As part of the measurement setup, the *S*-parameters are acquired with a planar raster scanner. The inspected object is scanned between two fixed antennas aligned along each other's boresight. Reflection and transmission *S*-parameters are acquired. The antennas are rectangular patches on a Teflon substrate. The frequency is swept from 11 GHz to 13 GHz. The distance between the top and bottom scanning planes is 10 cm. The sampling step in both directions (*x* and *y*) is 5 mm. The imaged area is 20 cm by 20 cm. The RO consists of the measurement setup immersed in air. The CO differs from the RO only by the presence of a dielectric ($\varepsilon_{r,sc} \approx 50$) cylinder of 1 cm height and 1 cm diameter located in the center of the imaged volume.

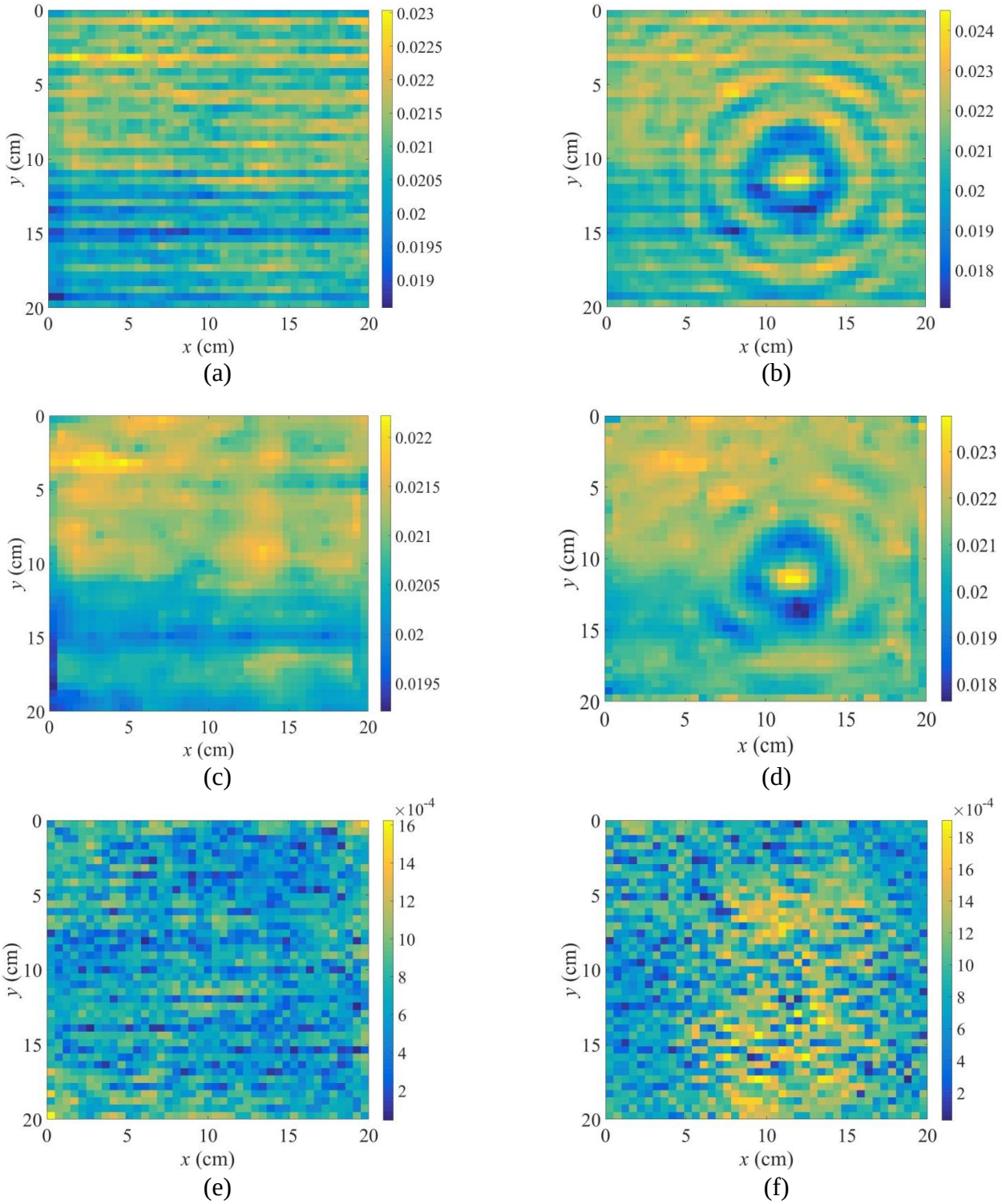

Figure 4.1 Measured transmission coefficient modulus of: (a) RO and (b) CO. Extracted signal-component modulus for: (c) RO and (d) CO. Extracted noise-component modulus for: (e) RO and (f) CO. Natural neighbor interpolation is used. Frequency is 12.5 GHz.

The algorithm is applied to the acquired transmission *S*-parameters of the RO and CO at all frequencies. It takes 4 iterations (4.2 sec) in the RO case and 60 iterations (51.7 sec) in the CO case to satisfy the convergence criterion.

Figure 4.1(a) shows a sample of the modulus of S_{RO} at 12.5 GHz. The RO signal and noise components extracted by the algorithm are shown in Figure 4.1(c) and Figure 4.1(e), respectively. Analogous plots of the CO input data, the extracted CO signal and CO noise are shown in Figure 4.1(b), (d), and (f), respectively.

The cross-correlation between the CO signal and noise components is shown in Figure 4.2(a). Within the 99% confidence interval, the CO noise is best aligned with the CO signal at zero lag. In addition, we analyze the noise outcome on repeating patterns by calculating the autocorrelation of the CO noise (Figure 4.2(b)). This correlogram suggests that the data are not random, but rather have a moderate positive autocorrelation. In general, noise autocorrelation can be used as an additional measure of the algorithm's performance.

Nearest neighbor interpolation is also suitable for the proposed algorithm [22]. The MATLAB function *scatteredInterpolant()* with the option *nearest* is used. It takes 81 iterations (64.5 sec) to satisfy the convergence criterion, with the resultant CO signal and noise components shown in Figure 4.3. The respective cross-correlation estimate from the convergence criterion is shown in Figure 4.2(c), whereas the noise autocorrelation is given in Figure 4.2(d). The CO's signal and noise become less correlated (Figure 4.2(c)) compared to Figure 4.2(a). Moreover, the CO noise component becomes random since

only a few values are outside the 99% confidence limit (Figure 4.2(d)). However, using nearest neighbor interpolation requires 21 more iterations to satisfy the convergence criterion in comparison with the natural neighbor interpolation.

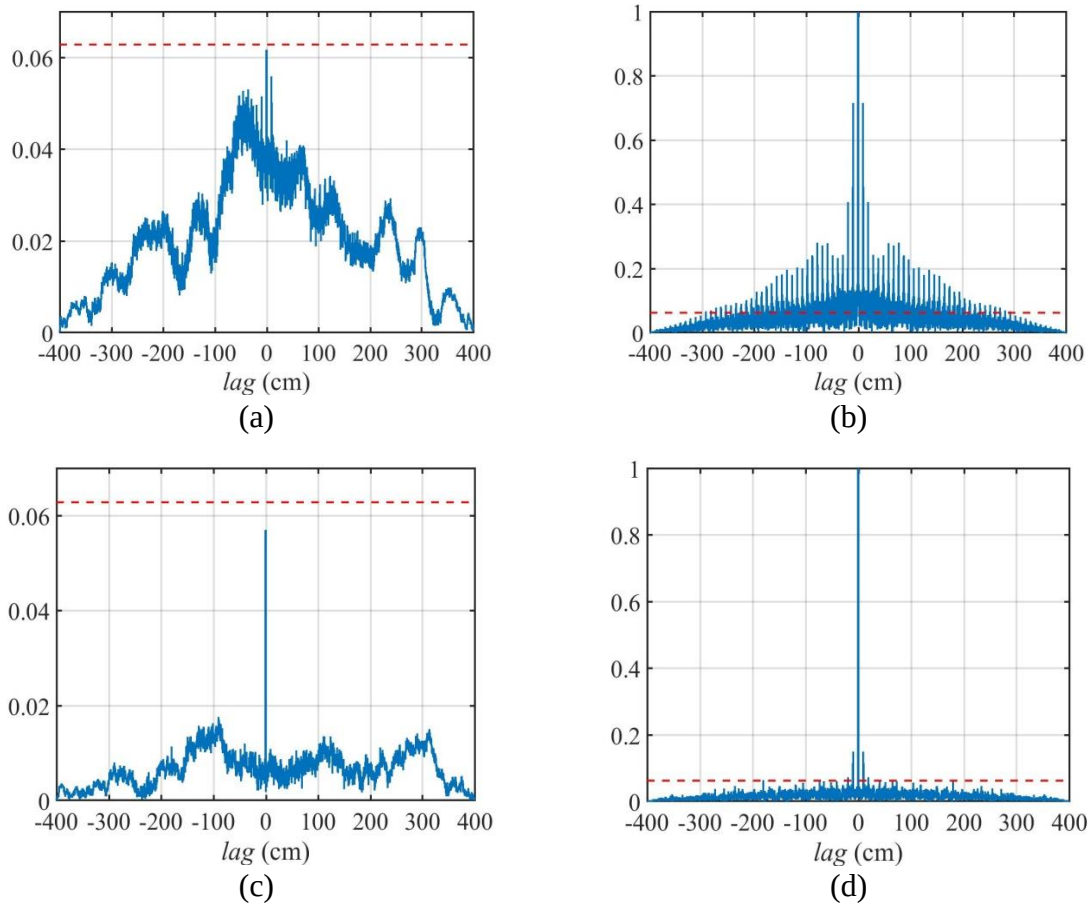

Figure 4.2 Correlation functions of the separated CO signal and CO noise components. Natural neighbor interpolation: (a) cross-correlation of signal and noise, (b) auto-correlation of noise. Nearest neighbor interpolation: (c) cross-correlation of signal and noise, (d) auto-correlation of noise. 2D data are reshaped into 1D arrays. Horizontal lines show 99% confidence interval. All sequences are normalized so that autocorrelations at zero lag equal 1.

Lastly, since we know that the signal features relatively low frequency information whereas the noise is in the higher frequencies, another approach to signal extraction could be to use the Gabor filterbank. Gabor filters have been widely used in pattern analysis

[23]-[25]. Here, we construct the Gabor multichannel filterbank analogously to [26]: the number of designed filters is 30 and they are divided into nine orientations. The MATLAB function *imgaborfilt()* with octave band and unity aspect ratio settings is used. Elapsed time is 0.07 sec. The respective results are demonstrated in Figure 4.4. It is seen that in the presented example, the quality of signal extraction with the Gabor filterbank method does not exceed that obtained using the de-noising algorithm.

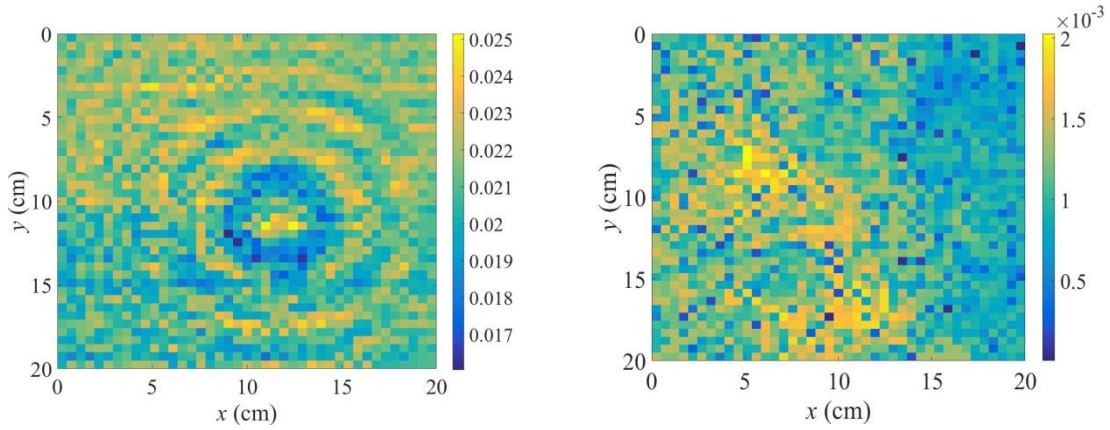

(a) (b)

Figure 4.3 Algorithm output for the CO case at 12.5 GHz: (a) signal modulus and (b) noise modulus. Nearest neighbor interpolation is used.

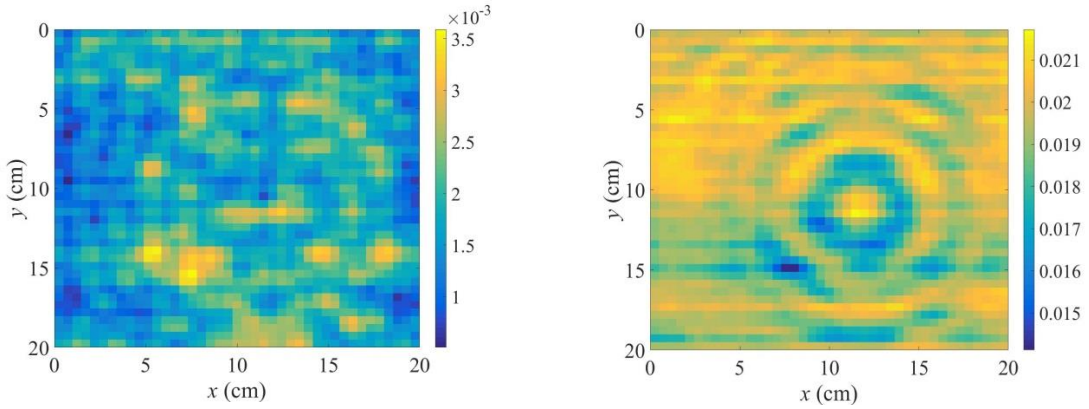

(a) (b)

Figure 4.4 Gabor filterbank outcome for the CO case at 12.5 GHz: (a) signal modulus and (b) result of subtracting signal modulus from the CO data modulus.

4.4 Application to Microwave Imaging

A de-noising algorithm has been proposed for complex *S*-parameter data used in microwave imaging. It enables the efficient estimation of the noise-free signal component and its separation from the noise component in 2D-scan data sets. Two simple 2D data extrema interpolation methods have been discussed and compared, with the nearest neighbor method yielding better quantitative results. Note that using more sophisticated 2D interpolation methods [22] could improve the algorithm's performance.

The performance of the Gabor filterbank is investigated for the purpose of the signal and noise separation in the *S*-parameters' data. By inspecting the results visually, we conclude that this method does not provide meaningful results, even though it is much faster.

4.4.1 De-noising Raw Data before Reconstruction

The proposed algorithm offers several benefits in microwave imaging. First, it can suppress noise and uncertainties in the data used as input to the reconstruction algorithms. For example, without de-noising, the SNR of the calibrated CO scattering parameters $\left(S_{\mathrm{CO}} - S_{\mathrm{RO}}\right)$ at 12.5 GHz equals 9.11 dB as per the formula given in [8]. After de-noising, the SNR improves by 2.7 dB.

In inverse problems, the classical way to filter out the high-frequency components associated with the small singular values is to apply regularization (e.g., Tikhonov regularization or the truncated singular value decomposition) [27]. On the other hand, it

can be seen that the de-noising algorithm offers a similar benefit: the de-noised *S*-parameters are the low-pass filtered forms of the raw data. At the same time, the de-noising algorithm does not require any ad hoc parameters whereas the choice of a regularization parameter and the penalty matrix (if no knowledge is available about the desired solution) is a difficult subject [27].

To maintain all of the information about the inspected object in the reconstruction examples presented in this thesis, the de-noising algorithm is applied only to the calibration measurements (RO and CO). Consequently, another notable improvement from using the de-noising algorithm is concerned with the BCCB system matrix containing the CO power maps (see (3.18)). Specifically, its condition number improves up to a few orders of magnitude (e.g., four orders of magnitude in the case of the calibration with a dielectric scattering probe embedded in the absorber sheet [28]). It is known that the ill-conditioned systems of linear equations (having matrices with large condition numbers) are a consequence of the similarity of the matrix components: graphically, equations correspond to near-parallel lines [29]. Applying the de-noising algorithm to the data to be processed alleviates this near-parallelism, thereby improving the condition number of the BCCB system matrix.

4.4.2 Quantifying the Performance of Acquisition Systems

The proposed algorithm can be also used to quantify the imaging system's dynamic range defined as

$$D = \frac{s_{\max}}{s_{\min}}, \tag{4.2}$$

where $s_{\max}$, $s_{\min}$ are the maximum and minimum measurable signals, respectively. The maximum signal is estimated as the mean RO signal modulus, whereas the minimum signal is the mean RO noise modulus. For the acquisition system used to validate the algorithm's performance in this chapter, (4.2) gives the dynamic range of 30.13 dB.

Finally, the de-noising algorithm can be instrumental in estimating the SNR of a particular data set. SNR is defined here similarly to the definition commonly used in image processing [30]-[32]:

$$\mathrm{SNR} = \frac{\mu}{\sigma}, \tag{4.3}$$

where μ is the signal mean modulus and σ is the standard deviation of the estimated noise. For example, with the CO data in Figure 4.1(b), (d) and (f), (4.3) yields the SNR value of 13.65 dB.

References

[1] N. K. Nikolova. *Introduction to Microwave Imaging*. Cambridge University Press, 2017.

[2] J. T. Bushberg, J. A. Seibert, E. M. Leidholdt Jr., J. M. Boone. *The Essential Physics of Medical Imaging*. 3rd ed. Philadelphia, USA: Lippincott Williams & Wilkins, 2012.

[3] L. Kaufman, D. M. Kramer, L. E. Crooks, and D. A. Ortendahl, "Measuring signal-to-noise ratios in MR imaging," *Radiology*, vol. 173, no. 1, pp. 265–267, Oct. 1989.

[4] M. J. Firbank, A. Coulthard, R. M. Harrison, and E. D. Williams, "A comparison of two methods for measuring the signal-to-noise ratio on MR images," *Phys. Med. Biol.*, vol. 44, no. 12, pp. N261–N264, Dec. 1999.

[5] O. Dietrich, J. G. Raya, S. B. Reeder, M. F. Reiser, and S. O. Schoenberg, "Measurement of signal-to-noise ratios in MR images: influence of multichannel coils. Parallel imaging and reconstruction filters," *J. Magn. Reson. Imaging*, vol. 26, no. 2, pp. 375–385, Aug. 2007.

[6] M. J. Firbank, R. M. Harrison, E. D. Williams, and A. Coulthard, "Quality assurance for MRI: practical experience," *British J. Radiol.*, vol. 73, no. 868, pp. 376–383, 2000.

[7] X. Song, B. W. Pogue, S. Jiang, M. M. Doyley, H. Dehghani, T. D. Tosteson, and K. D. Paulsen, "Automated region detection based on the contrast-to-noise ratio in near-infrared tomography," *Applied Optics*, vol. 43, no. 5, pp. 1053–1062, Feb. 2004.

[8] J. J. McCombe and N. K. Nikolova, "SNR assessment of microwave imaging systems," *Proc. IEEE AP-S/URSI Int. Symp. Ant. Propag.*, pp. 149–150, July 2014.

[9] N. K. Nikolova, "Microwave biomedical imaging," *Wiley Encyclopedia of Electrical and Electronics Engineering*, pp. 1–22. (published online Apr. 25, 2014).

[10] C. Eyraud, A. Litman, A. Herique, and W. Kofman, "Microwave imaging from experimental data within a Bayesian framework with realistic random noise," *Inverse Problems*, vol. 25, no. 2, 024005, 16 pp., Feb. 2009.

[11] J. G. Proakis and D. G. Manolakis. *Digital Signal Processing: Principles, Algorithms, and Applications*. 3rd ed. Englewood Cliffs, NJ: Prentice-Hall, 1996.

[12] D. L. Donoho, "De-noising by soft-thresholding," *IEEE Trans. Inf. Theory*, vol. 41, no. 3, pp. 613–627, May 1995.

[13] C. Eyraud, J.-M. Geffrin, A. Litman, P. Sabouroux, and H. Giovannini, "Drift correction for scattering measurements," *Applied Physics Lett*., vol. 89, 244104, pp. 1–3, Dec. 2006.

[14] N. E. Huang *et al*., "The empirical mode decomposition and the Hilbert spectrum for nonlinear and non-staionary time series analysis," *Proc. R. Soc. Lond. A, Math. Phys. Sci*., vol. 454, no. 1971, pp. 903–995, Mar. 1998.

[15] A.-O. Boudraa and J.-C. Cexus, "EMD-based signal filtering," *IEEE Trans. Instrum. Meas*., vol. 56, no. 6, pp. 2196–2202, Dec. 2007.

[16] A. O. Boudraa, J. C. Cexus, and Z. Saidi, "EMD-based signal noise reduction," *Int. J. Signal Process*., vol. 1, no. 1, pp. 33–37, Jan. 2005.

[17] S. Tu, J. J. McCombe, D. S. Shumakov, and N. K. Nikolova, "Fast quantitative microwave imaging with resolvent kernel extracted from measurements," *Inverse Problems*, vol. 31, no. 4, 33 pp., Mar. 2015.

[18] R. K. Amineh, J. J. McCombe, A. Khalatpour, and N. K. Nikolova, "Microwave holography using point-spread functions measured with calibration objects," *IEEE Trans. Instrum. Meas.*, vol. 64, no. 2, pp. 403–417, Feb. 2015.

[19] G. E. P. Box, W. G. Hunter, and J. S. Hunter. *Statistics for experimenters: an introduction to design, data analysis, and model building*. USA: John Wiley & Sons, 1978.

[20] MATLAB R2016a. The MathWorks Inc., Natick, MA, USA, 2016.

[21] R. Sibson, "A brief description of natural neighbor interpolation" in *Interpolating Multivariate Data*. New York: John Wiley & Sons, 1981, ch. 2, pp. 21–36.

[22] T. M. Lehmann, C. Gonner, and K. Spitzer, "Survey: interpolation methods in medical image processing," *IEEE Trans. Med. Imaging*, vol. 18, no. 11, pp. 1049–1075, Nov. 1999.

[23] C. Liu and H. Wechsler, "Gabor feature based classification using the enhanced fisher linear discriminant model for face recognition," *IEEE Trans. Image Proc*., vol. 11, no. 4, pp. 467–476, Apr. 2002.

[24] S. Meshgini, A. Aghagolzadeh, H. Seyedarabi, "Face recognition using Gabor-based direct linear discriminant analysis and support vector machine," *Comput. Electr. Eng.*, vol. 39, no. 3, pp. 727–745, Apr. 2013.

[25] M. S. Pattichis and A. C. Bovik, "Analyzing image structure by multidimensional frequency modulation," *IEEE Trans. Pattern Anal. Mach. Intell*., vol. 29, no. 5, pp. 753–766, May 2007.

[26] M. Y. Elshinawy, J. Zeng, S.-C. Lo, and M. F. Chouikha, "Breast cancer detection in mammogram with AM-FM modeling and Gabor filtering," *Proc. 7th Int. Conf. on Signal Processing (ICSP)*, vol. 3, pp. 2564–2567, Sep. 2004.

[27] P. C. Hansen, "Numerical tools for analysis and solution of Fredholm integral equations of the first kind," *Inverse Problems*, vol. 8, no. 6, pp. 849–872, 1992.

[28] D. S. Shumakov and N. K. Nikolova, "Fast quantitative microwave imaging with scattered-power maps," *IEEE Trans. Microw. Theory Techn.*, Early Access, pp. 1–11, May 2017.

[29] M. Farooq and A. Salhi, "Improving the solvability of ill-conditioned systems of linear equations by reducing the condition number of their matrices," *J. Korean Math. Soc.*, vol. 48, no. 5, pp. 939–952, 2011.

[30] R. C. Gonzalez, R. E. Woods. *Digital Image Processing*. 3rd ed. Prentice Hall, 2008, p. 354.

[31] T. Stathaki. *Image Fusion: Algorithms and Applications*. Academic Press, 2008, p. 471.

[32] J. C. Russ. *The Image Processing Handbook*. 5th ed. CRC Press, 2006.

Chapter 5

Validation of Scattered-Power Mapping

5.1 Introduction

The 2D and 3D reconstruction examples obtained with the proposed BCCB SPM and convolution-based SPM are presented in this chapter. Since the methods do not need analytical or numerical approximations of the forward model, they are particularly beneficial in near-field imaging. Both of them are direct-inversion techniques intended for the imaging of weak-scattering problems. Calibration measurements are used to obtain the resolvent kernel in the integral equation of scattering, thus providing a high-fidelity and system-specific forward model in both BCCB SPM and convolution-based SPM. The key aspect that enables their quantitative outcome is the use of a calibration object, the response of which constitutes a system PSF. The proposed methods are predominantly validated on examples employing the well-established calibration with a dielectric scattering probe. However, the reconstruction results in the case of the calibration with a metallic scattering probe are presented as well.

The near-field acquisition systems used here perform planar raster scanning of the inspected object (see Figure 5.1). Using a vector network analyzer (VNA), both reflection

and transmission *S*-parameters are measured. Note that only the transmission data are acquired when a power amplifier is connected directly to the transmitting antenna.

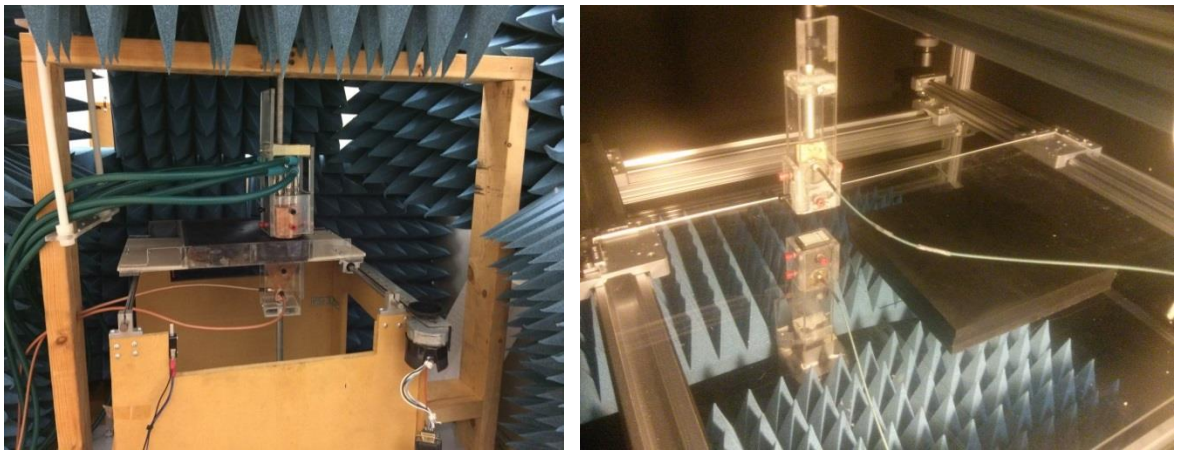

(a) (b)

Figure 5.1 Photographs of the two planar raster-scanning systems used to acquire the scattering parameters: (a) an older system and (b) a new high-precision system.

Since the acquired measurements are *S*-parameter frequency sweeps in a wide band, the optimal choice of frequencies has to be set. Low frequencies mean better penetration and thus higher signal-to-noise ratio. However, the spatial resolution is better at higher frequencies. In the microwave imaging of tissue, the preferred frequencies for direct-inversion methods in which the resolution strongly depends on the wavelength are between 2 GHz and 8 GHz [1][2]. The frequency range used in our experiments is from 3 GHz to 9 GHz with 61 sampling points.

As shown in Figure 5.1, the scattered field is sampled in a bi-static or multistatic way depending on the case. The sampling is implemented mechanically which makes the scanning time of the order of hours per object. It should be emphasized that this scanning time can be significantly reduced by exploiting electronically-switched sensor arrays.

The inspected object is placed on a positioning platform between the antennas (see Figure 5.1). The antennas' boresight is orthogonal to the platform. The platform is moved laterally (along *x* and *y*) by precision stepper motors. Thus, the scattering parameters are acquired as a function of *x* and *y*, where (*x*, *y*) is the relative lateral position of the inspected object with respect to the antennas. The vertical position of the platform (along *z*) is adjustable and fixed at a distance of about 3 mm from the aperture of the bottom antenna.

The quantitative images produced by the proposed reconstruction methods show the relative complex (real and imaginary parts) permittivity distribution as a function of *x* and *y* plotted on a linear (not logarithmic) scale. The $\exp(\mathrm{i}\omega t)$ time dependence has been employed throughout this thesis implying that the physically viable values of the relative permittivity distribution are

$$\mathrm{Re}\left\{\varepsilon_{\mathrm{OUT}}(\mathbf{r}')\right\} \geq 1,\ \mathrm{Im}\left\{\varepsilon_{\mathrm{OUT}}(\mathbf{r}')\right\} \leq 0,\ \mathbf{r}' \in V'. \tag{5.1}$$

Finally, all of the presented images are obtained by combining the respective OUT and CO power maps across the frequency range from 3 GHz to 9 GHz.

5.2 Apodization Function

Due to the specifics of the imaging setups used in our experiments, a sampled signal does not smoothly go down to zero at the edges of the acquisition aperture. As a result, leakage sidelobes are produced upon performing a discrete Fourier transform. This effect is known as apodization [3]-[5]. Such sidelobes can create ringing artifacts which are

usually mitigated by multiplying a signal (in the spatial domain or in the frequency domain) by a proper apodization function, also known as a window function [4]-[6]. It is a non-negative mathematical function that goes sufficiently rapidly toward zero outside of some given interval, so that when multiplied by the sampled signal, the product has the same feature outside of that interval.

The suppression of leakage sidelobes results in a decrease of the spatial resolution [4]. Typically used apodization functions (e.g., Gaussian apodization function) increase either the resolution or the signal-to-noise ratio (SNR), but always at a considerable expense of one or the other [5]. However, the functions that may be used to increase both the resolution and SNR simultaneously can be found in literature [5][7].

5.3 Two-Dimensional Imaging

5.3.1 Calibration with Dielectric Scattering Probe

The first validation example is similar to that presented in [8][9] when two dielectric objects embedded in the absorber sheets are imaged. We commence with such example in order to demonstrate the capabilities of the proposed BCCB SPM and convolution-based SPM compared to those of the prior method in [8][9].

5.3.1.1 Two Dielectric Cylinders Embedded in Absorbers

The specifics of the imaged setup are the same as in the experiment reported in [8][9]. The scanned area is 15 cm by 15 cm with a 5 mm spatial step. The reference object (RO) consists of 5 absorber sheets being 20 cm by 20 cm by 1 cm in size, with the relative

permittivity of $\varepsilon_{r,RO} \approx 10 - i5$. The calibration object (CO) is identical to the RO except for a dielectric cylinder of $\varepsilon_{r,sc} \approx 15$ [10] embedded in the center of the middle layer (see Figure 5.2(a)). Finally, the object under test (OUT) is identical to the RO except for two such dielectric cylinders separated by 1 cm, and embedded in the middle layer (see Figure 5.2(b)).

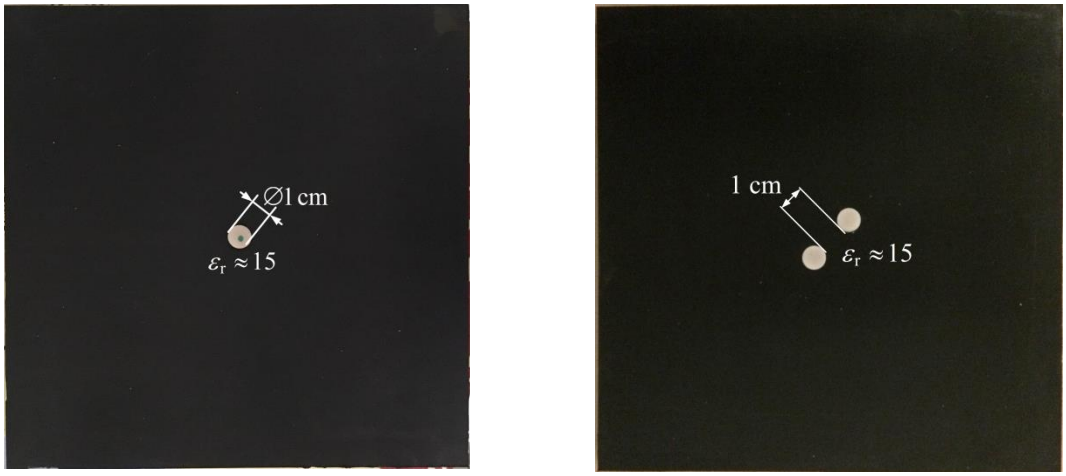

(a) (b)

Figure 5.2 Photographs of: (a) CO layer with a dielectric cylinder serving as a scattering probe; (b) middle layer of OUT with two identical dielectric cylinders.

The reconstructed results of the OUT (middle layer) obtained with the BCCB SPM are shown in Figure 5.3. The figure shows the estimated permittivity distribution when the SPM forward model is linearized with the LQL approximation. The BCCB solver with no regularization has been used. The same case is also reconstructed with the convolution-based SPM with the respective results shown in Figure 5.4. We observe a better quantitative reconstruction in Figure 5.3 and Figure 5.4 compared to the images shown in [8][9], at a much faster computational time on the order of seconds for the BCCB SPM

and about a second for the convolution-based SPM. Along with the generation and storing of the CO power maps, the prior method takes a few hours to produce the images.

Also, it is seen that the images obtained with the BCCB SPM and those obtained with the convolution-based SPM are similar. However, the images obtained with the BCCB SPM contain some nonphysical values in the imaginary part (see Figure 5.3(b)) Another important observation is that we are now able to reconstruct the whole scanned area of 15 cm by 15 cm. This is compared to the imaged area of 5.5 cm by 5.5 cm in [8][9].

In Figure 5.3 and Figure 5.4, we see that in the neighborhood of the central pixels with large values, there are a number of surrounding pixels with small values. We also notice that the reconstructed images contain artifacts at the center of the image, i.e., instead of showing two cylindrical objects, the images show three objects with the central one being an artifact. These image errors are due to considerable noise and positioning uncertainties. In such cases, it is recommended to use the de-noising algorithm presented in Chapter 4. We apply the de-noising algorithm to the scattered CO response at each frequency sample as a preprocessing step. The so-obtained images obtained with the BCCB SPM are shown in Figure 5.5: the central artifacts are gone and the cylinders are seen well. Also, note that there are no nonphysical values in the imaginary part (see Figure 5.5(b)). However, the maximum reconstructed value in the real part of the relative permittivity dropped from 17.37 to 11.71 (see Figure 5.3(a) and Figure 5.5(a)) whereas the maximum reconstructed value in the imaginary part dropped from 0.62 to –2.86 (see Figure 5.3(b) and Figure 5.5(b)). Note that the images obtained with the convolution-based SPM applied to the de-noised CO data are identical to those in Figure 5.5.

It is seen that even after de-noising the CO scattered data, weak artifacts in the form of horizontal and vertical lines intersecting at the center of the image are still present (Figure 5.5). This artifact is further referred to as a central-line artifact. It is attributed to the apodization phenomenon: the produced leakage sidelobes cause ringing artifacts, which in our case appear as spurious lines at the center of the reconstructed images. In order to mitigate this effect, we employ the commonly used Gaussian apodization function. More specifically, we multiply the scattered OUT data as well as the de-noised scattered CO data by the Gaussian apodization function [4] in the spatial domain. The respective images obtained with the BCCB SPM are shown in Figure 5.6. The quantitative values improve whereas the central-line artifact is alleviated. Following the same data pre-processing steps, the reconstruction with the convolution-based SPM is shown in Figure 5.7. The so-obtained images look identical to those in Figure 5.6.

Note that applying the same Gaussian apodization function directly to the raw data without de-noising of the CO scattered data, results in a reconstruction of poor fidelity both with the BCCB SPM and the convolution-based SPM (see Figure 5.8 and Figure 5.9). In addition to the nonphysical values present in the imaginary parts of the relative permittivity, we still see the artifacts in the center of the images. Therefore, we conclude that in this experiment, nonphysical solutions as well as the central and line artifacts are attributed to the noise and uncertainties contained in the raw data. Another important point is that the images obtained with the BCCB SPM are very similar to those obtained with the convolution-based SPM, the latter being faster.

As a last remark, we note that the condition number of the BCCB system matrix under the LQL approximation improves from 9.71e+03 to 1.34e+03 after applying the de-noising algorithm.

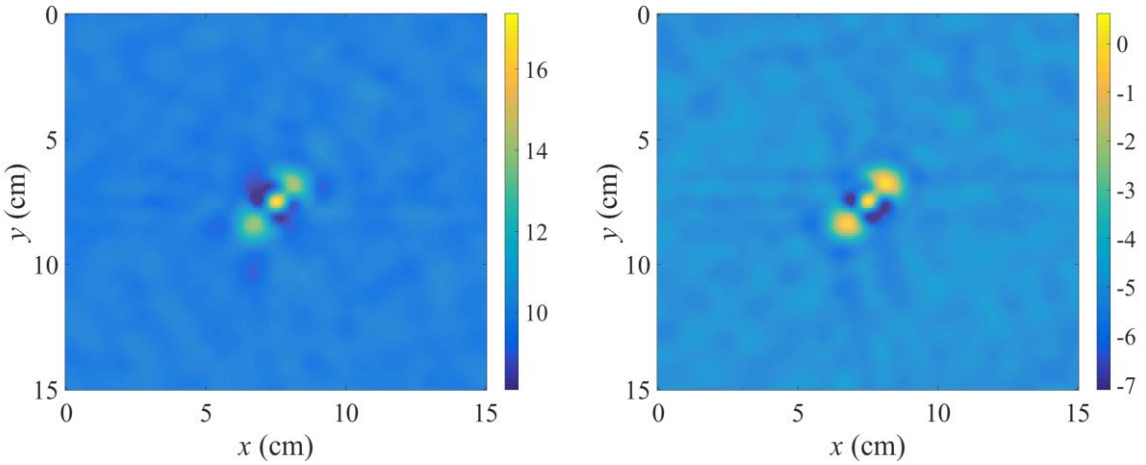

(a) (b)

Figure 5.3 Estimated relative permittivity of 2 dielectric cylinders: (a) real part, (b) imaginary part. BCCB SPM is used.

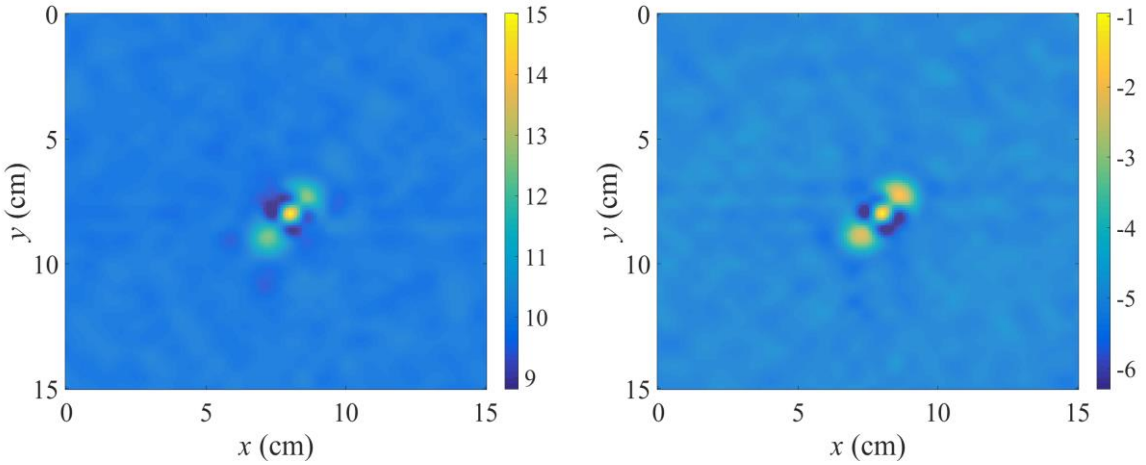

(a) (b)

Figure 5.4 Estimated relative permittivity of 2 dielectric cylinders: (a) real part, (b) imaginary part. Convolution-based SPM is used.

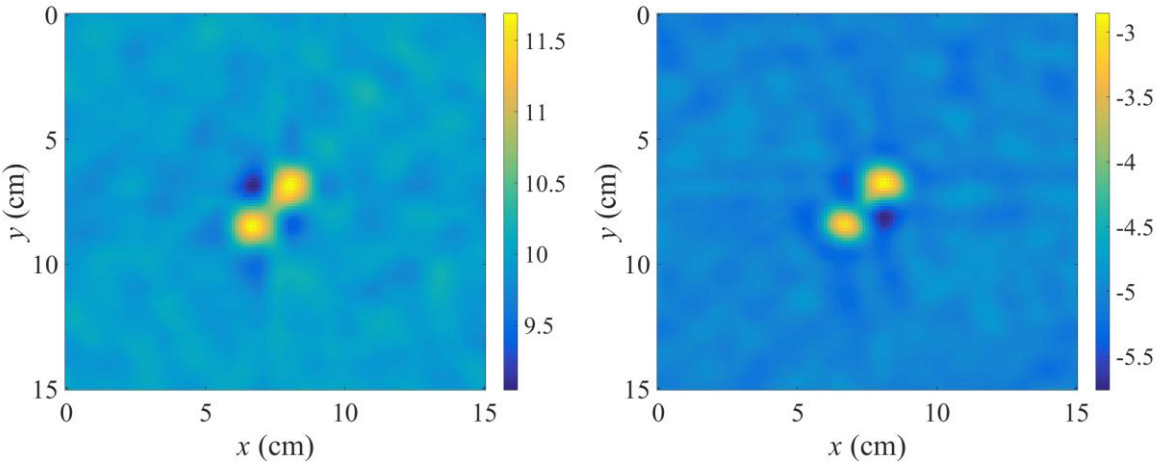

(a) (b)

Figure 5.5 Estimated relative permittivity of 2 dielectric cylinders: (a) real part, (b) imaginary part. BCCB SPM is used with the de-noising algorithm applied to the scattered CO data at each frequency sample.

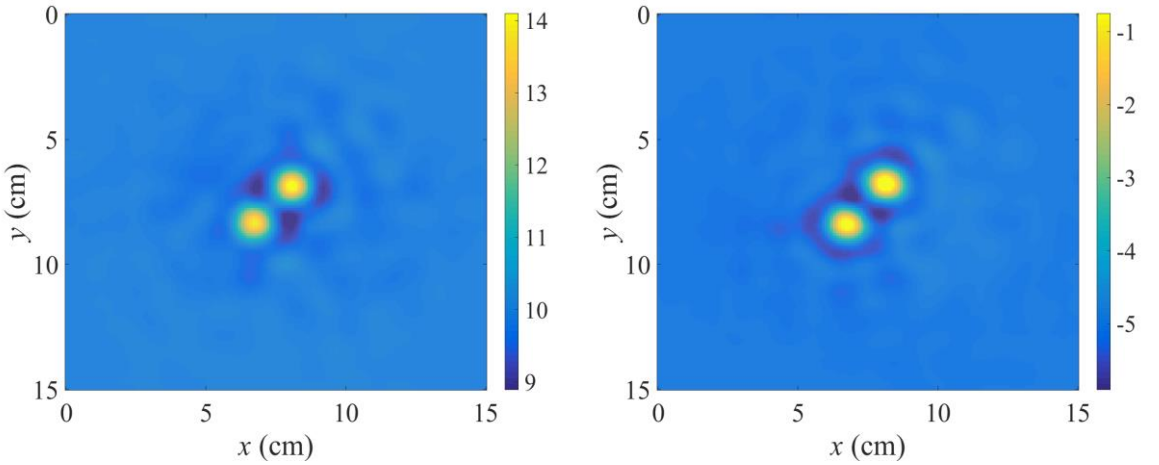

(a) (b)

Figure 5.6 Estimated relative permittivity of 2 dielectric cylinders: (a) real part, (b) imaginary part. BCCB SPM is used with the de-noised scattered CO data. Gaussian apodization function is applied.

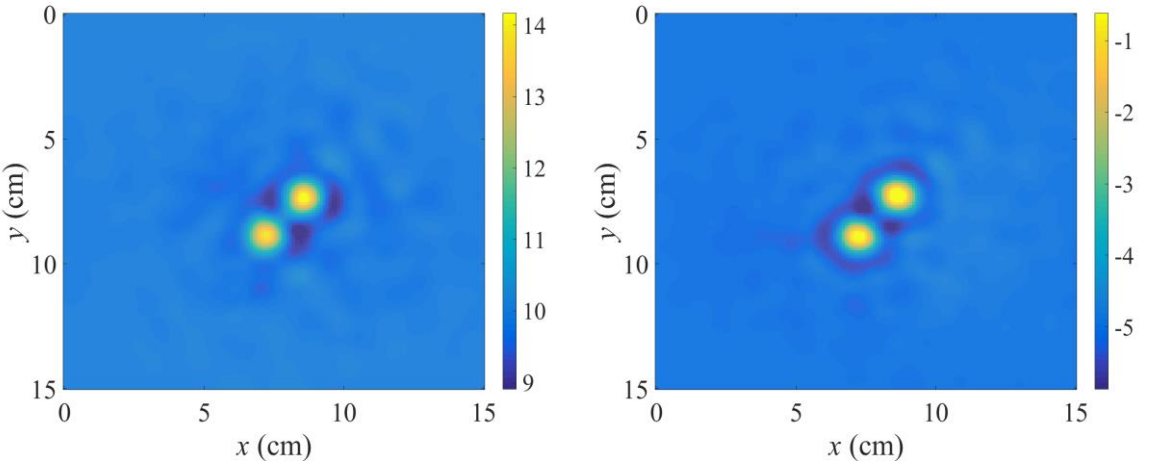

(a) (b)

Figure 5.7 Estimated relative permittivity of 2 dielectric cylinders: (a) real part, (b) imaginary part. Convolution-based SPM is used with the de-noised scattered CO data. Gaussian apodization function is applied.

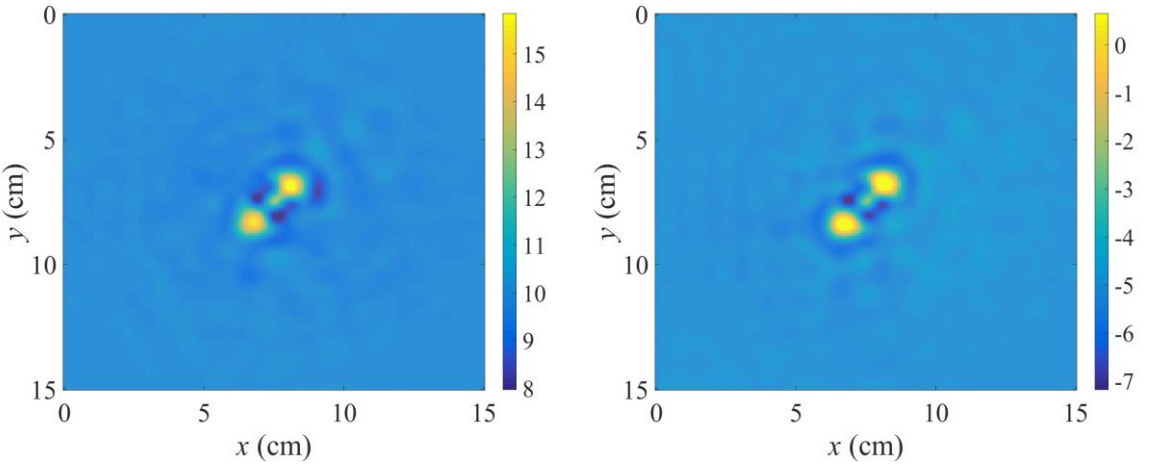

(a) (b)

Figure 5.8 Estimated relative permittivity of 2 dielectric cylinders: (a) real part, (b) imaginary part. BCCB SPM is used with Gaussian apodization function. No data de-noising is done.

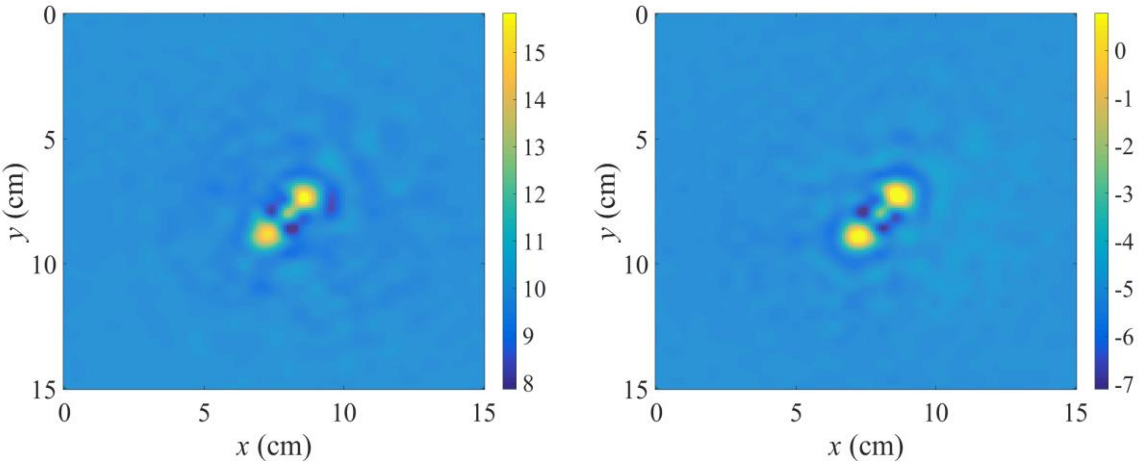

(a) (b)

Figure 5.9 Estimated relative permittivity of 2 dielectric cylinders: (a) real part, (b) imaginary part. Convolution-based SPM is used with Gaussian apodization function. No data de-noising is done.

5.3.1.2 Four Dielectric Cylinders in Air

The experimental setup consists of two X-band open-end air-filled waveguides with the waveguide at the bottom serving as a receiver only. Thus, the measured data consist of the forward-scattered signals and two reflected signals. The distance from the top antenna to the OUT is 5 cm. The imaged area is 20 cm by 20 cm. The sampling step in both lateral directions is 5 mm.

The imaged dielectric cylinders of 1 cm height and 1 cm diameter have a relative permittivity of $\varepsilon_{r,OUT} \approx 50$. They are placed as shown in Figure 5.10 with the edge-to-edge separation chosen approximately equal to $\lambda_0/4$ (6.5 mm), $\lambda_0/2$ (13 mm) and λ_0 (26 mm) at the central frequency of the X-band [11][13]. An identical dielectric cylinder with $\varepsilon_{r,sc} \approx 50$ serves as a scattering probe in the CO. The RO is comprised of air.

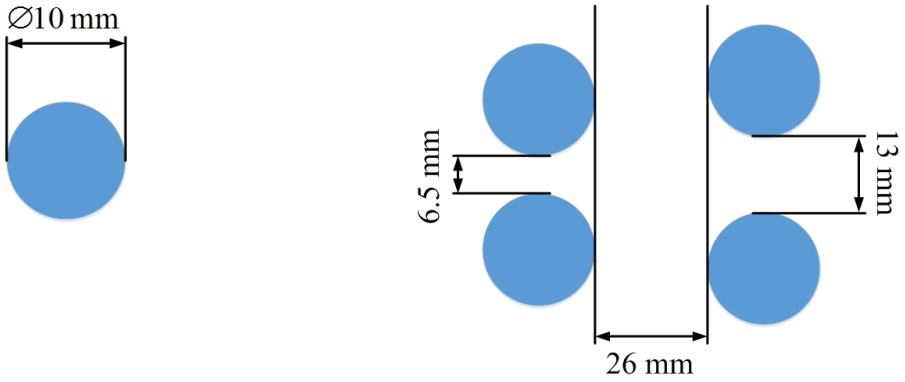

Figure 5.10 Schematic view of (a) dielectric cylinder serving as a scattering probe in the CO, and (b) the OUT consisting of four identical dielectric cylinders.

The reconstructed OUT using the BCCB SPM and the convolution-based SPM is shown in Figure 5.11 and Figure 5.12, respectively. In both cases, the LQL approximation has been used. Note that utilizing the LQLR approximation is expected to produce similar images compared to those obtained with the LQL approximation, since the size of the scatterers in the OUT is electrically small. Figure 5.13 shows an example of the LQLR images obtained with the BCCB SPM.

As in the previous experiment, BCCB SPM and convolution-based SPM produce practically identical results in the case of four dielectric cylinders in air. The computational time of the BCCB SPM is again on the order of seconds whereas the convolution-based SPM is real-time.

Next, we apply the de-noising algorithm to the RO as well as the CO data. The so-obtained images utilizing BCCB SPM with LQL approximation are shown in Figure 5.14. It is seen that the nonphysical values decrease. Also, we no longer see the artifacts in the center of the real part of the relative permittivity (see Figure 5.14(a)). The condition

number of the BCCB system matrix improves from 3.87e+05 to 5.91e+04. However, the central-line artifact becomes somewhat more pronounced after de-noising the data.

As the next step, we apply the Gaussian apodization function in the spatial domain with the respective images shown in Figure 5.15. It is seen that the nonphysical values in the imaginary part of the relative permittivity increase (see Figure 5.15(b)). Note that following the same pre-processing steps with the convolution-based SPM produces similar reconstruction results (see Figure 5.16).

In order to remove the nonphysical values in the relative permittivity distribution, we utilize the constrained solver instead of the BCCB solver. The fastest option is MOSEK (part of the CVX optimization toolbox for MATLAB [14]), which is designed for solving large optimization problems with many constraints and variables. The images obtained with MOSEK are shown in Figure 5.17 and Figure 5.18. The solutions do not contain nonphysical values and the real part of the relative permittivity is of satisfactory fidelity. However, we observe some artifacts close to the edges in the imaginary part of the relative permittivity (see Figure 5.17(b) and Figure 5.18(b)). The running time of the BCCB SPM employing MOSEK is on the order of minutes.

Another option can be to use the constrained linear least-squares solver (*lsqlin* function in MATLAB [15]). Unlike MOSEK, the *lsqlin* with *active-set* algorithm supports a starting point. Here, it is defined similarly to that in [8]:

$$\tau_p^{(0)} = \frac{M_{\mathrm{OUT}}(\mathbf{r}'_p)}{M_{\mathrm{CO},p}(\mathbf{r}'_p)},\ p = 1,\ldots,N_{\mathrm{v}}. \tag{5.2}$$

The running time is on the order of hours. The images obtained employing *lsqlin* are identical to those in Figure 5.17 and Figure 5.18.

It is clear from the presented example that the nonphysical permittivity values cannot be removed by using the de-noising algorithm. Therefore, they can only partially be attributed to the noise and uncertainties in the raw data. Note that the permittivity of the scattering probe should be on the order of that of the RO, so that the limits of the LQL approximation are observed. However, this is not the case here. Thus, the violation of the limitations of the forward model is the most likely cause for non-physicalities in the solution.

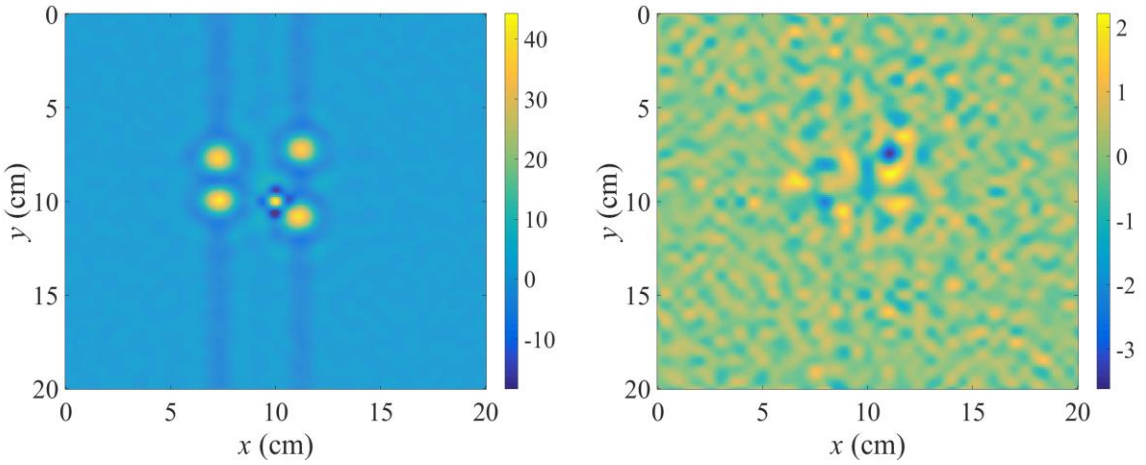

(a) (b)

Figure 5.11 Estimated relative permittivity of 4 dielectric cylinders: (a) real part, (b) imaginary part. BCCB SPM with LQL approximation and BCCB solver are used.

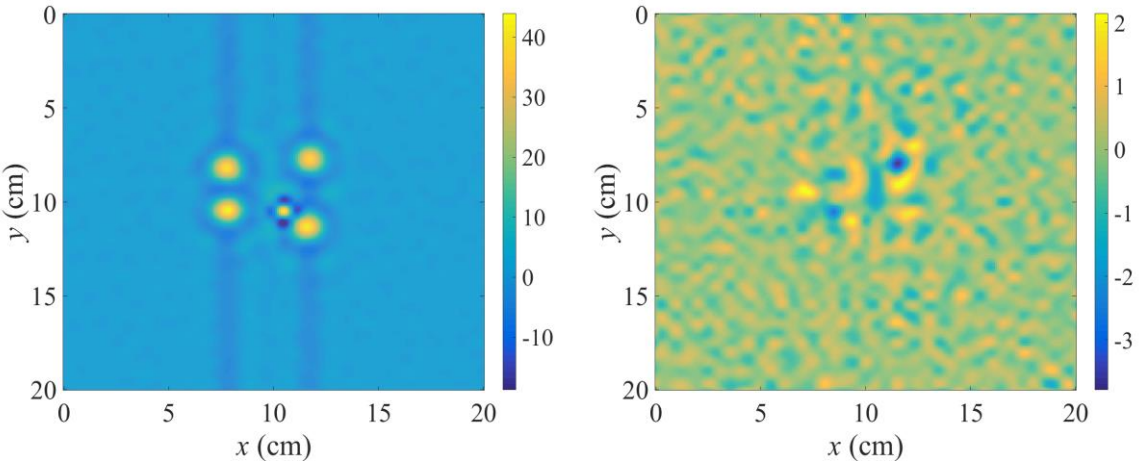

(a) (b)

Figure 5.12 Estimated relative permittivity of 4 dielectric cylinders: (a) real part, (b) imaginary part. Convolution-based SPM with LQL approximation and classical inverse filter are used.

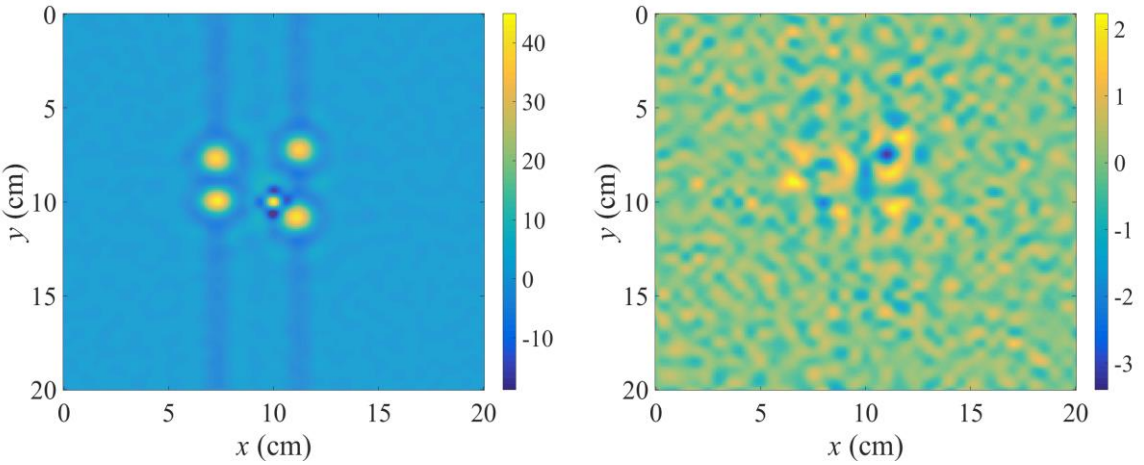

(a) (b)

Figure 5.13 Estimated relative permittivity of 4 dielectric cylinders: (a) real part, (b) imaginary part. BCCB SPM with LQLR approximation and BCCB solver are used.

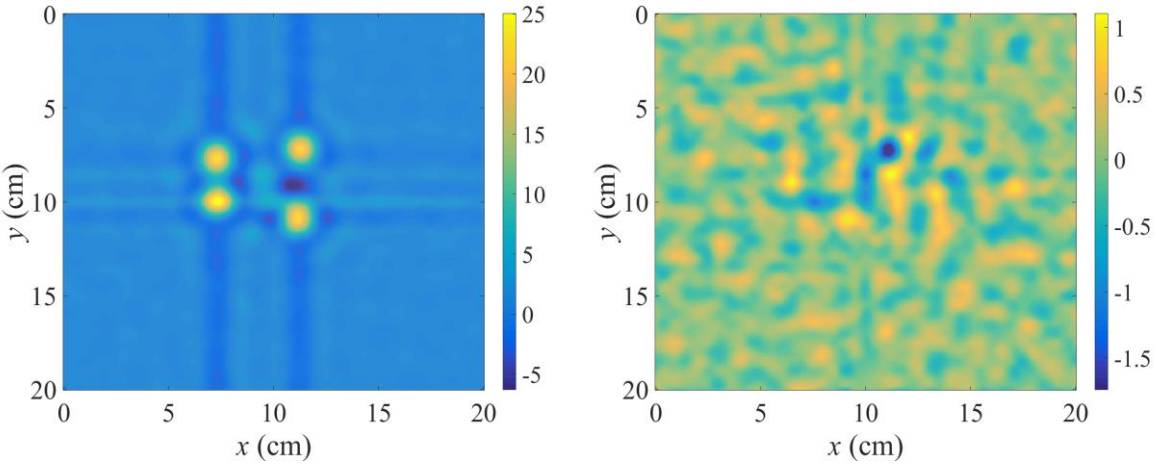

(a) (b)

Figure 5.14 Estimated relative permittivity of 4 dielectric cylinders: (a) real part, (b) imaginary part. BCCB SPM with LQL approximation and BCCB solver are used. De-noising algorithm is applied to the CO data as well as the RO data.

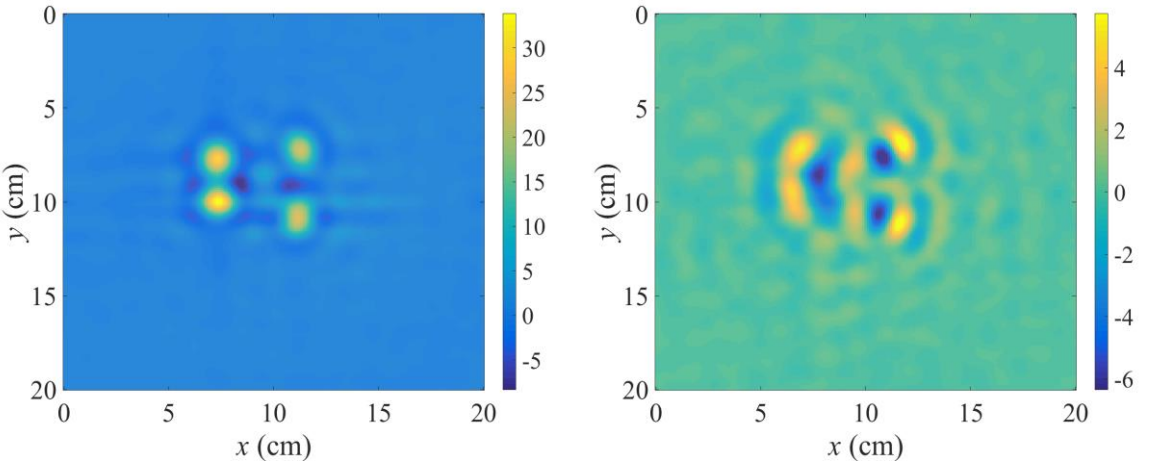

(a) (b)

Figure 5.15 Estimated relative permittivity of 4 dielectric cylinders: (a) real part, (b) imaginary part. BCCB SPM with LQL approximation and BCCB solver are used. De-noising algorithm is applied to the CO data as well as the RO data. Gaussian apodization function is used.

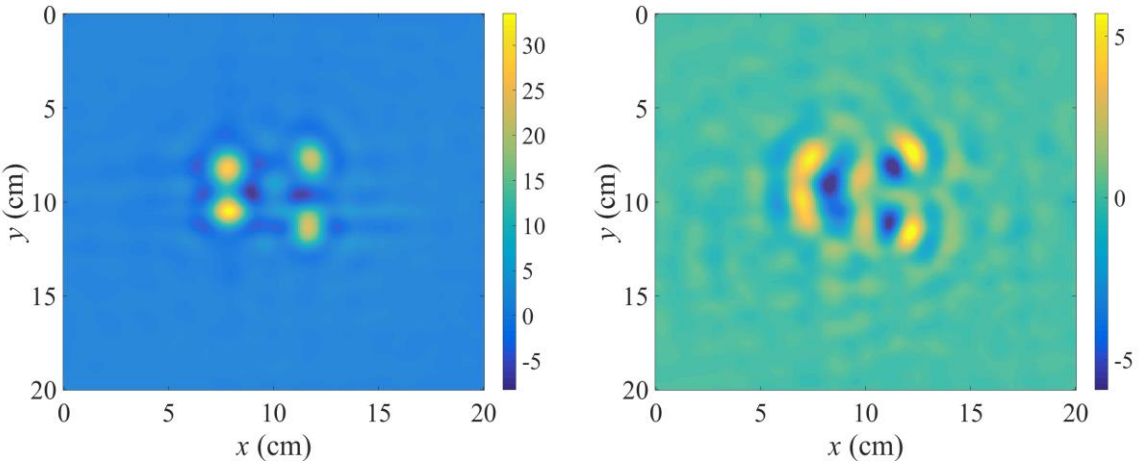

(a) (b)

Figure 5.16 Estimated relative permittivity of 4 dielectric cylinders: (a) real part, (b) imaginary part. Convolution-based SPM with LQL approximation is used. De-noising algorithm is applied to the CO data as well as the RO data. Gaussian apodization function is used.

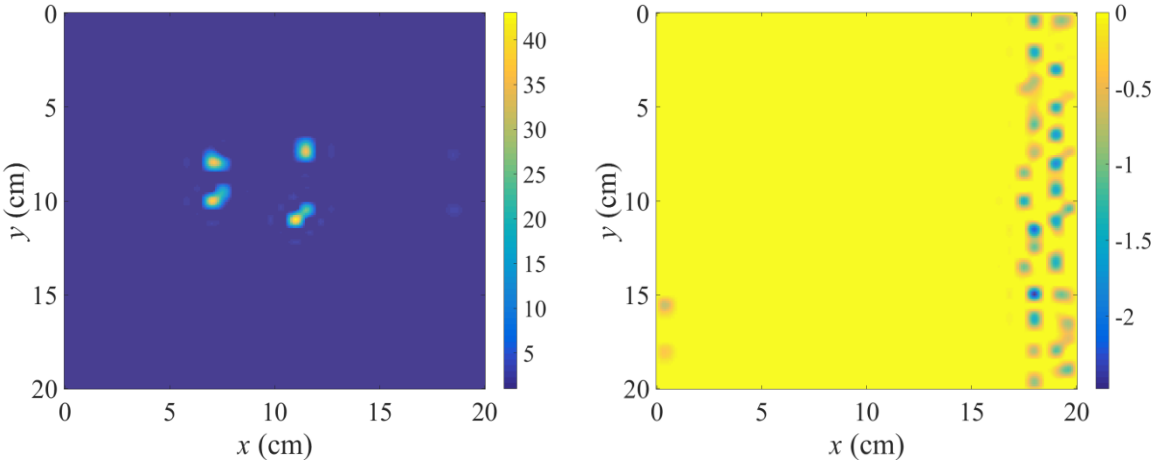

(a) (b)

Figure 5.17 Estimated relative permittivity of 4 dielectric cylinders: (a) real part, (b) imaginary part. BCCB SPM with LQL approximation and MOSEK solver are used.

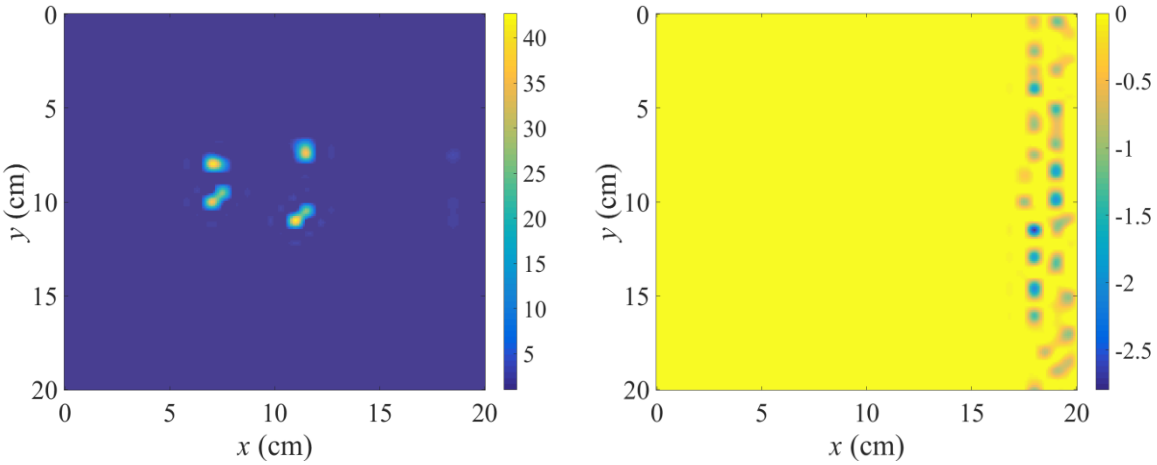

(a) (b)

Figure 5.18 Estimated relative permittivity of 4 dielectric cylinders: (a) real part, (b) imaginary part. BCCB SPM with LQLR approximation and MOSEK solver are used.

5.3.1.3 Reconstruction of Living Tissue Samples

In the next example, the imaging of living tissue is attempted. The reconstruction of such complex OUT is expected to test the limits of the SPM since they are violated by both the contrast and the size of the scattering object. The imaging setup consists of two TEM horn antennas [16] with a good impedance match between 3 GHz and 9 GHz. The antennas are aligned along each other's boresight. The imaged area is 13 cm by 13 cm with 2 mm spatial sampling step. The VNA output power is 0 dBm. The distance from the antennas' aperture to the inspected object on the platform is 3 mm.

The OUT consists of pure lard together with a chicken wing embedded in a lossy absorber sheet of 20 cm by 20 cm by 1 cm size (see Figure 5.19(a)). It is set on the 5 mm thick dielectric platform [17]. The RO is chosen to be an absorber sheet, whereas the CO contains a dielectric scattering probe in the center of the RO (see Figure 5.19(b)). It is a

cylinder of 5 mm diameter and 10 mm height. The frequency-averaged relative permittivities of the objects used in the experiment are given in Table 5.1.

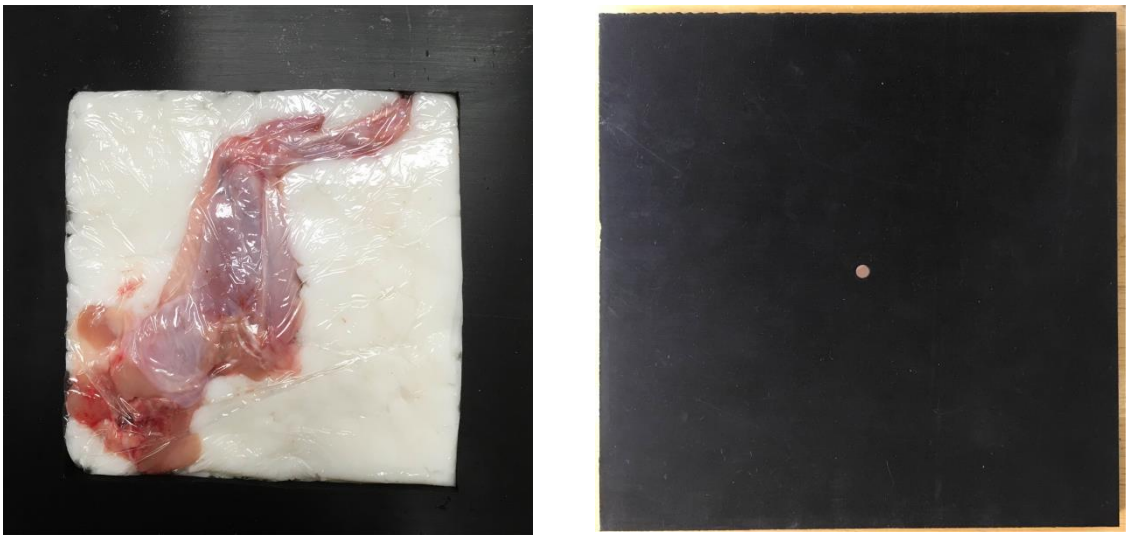

(a) (b)

Figure 5.19 Photographs of: (a) OUT and (b) CO, used in the experiment with the chicken wing.

Table 5.1

Averaged Relative Permittivities in Tissue Experiment

Object	Relative permittivity value, ε_r, averaged from 3 GHz to 9 GHz
Absorber sheet (RO)	10 – i5
Lard	3.1 – i0.4
Chicken skin	14.4 – i6.2
Chicken bone	21.5 – i10.7
Chicken muscle	47.6 – i25.9
Scatterer in the CO	43.7
Dielectric platform	10 – i0.035

Reconstruction results obtained with the BCCB SPM utilizing LQL approximation are shown in Figure 5.20. The convolution-based SPM produces identical outcome in this

case. In order to mitigate the detrimental effects of noise and uncertainties present in the images, we apply the de-noising algorithm to the CO data as well as the RO data as a pre-processing step (see Figure 5.21). The condition number of the BCCB system matrix under the LQL approximation drops from 6.06e+08 to 8.06e+04.

Even though the OUT contours are somewhat visible (Figure 5.21(a)), it is seen that the LQL model does not yield meaningful quantitative results. Moreover, employing another solver, the conjugate-gradient with circulant preconditioner (*pcg* function in MATLAB and MATLAB Structured Matrices Toolbox [18]), produces similar images to those obtained with the BCCB solver.

Finally, we employ the Gaussian apodization function in the spatial domain in order to remove the strong central-line artifacts in Figure 5.21. The resultant images are shown in Figure 5.22. The real part of the relative permittivity in Figure 5.22(a) appears somewhat worse than that in Figure 5.21(a). However, it does not contain central-line artifact or nonphysical values. Moreover, the imaginary part in Figure 5.22(b) is significantly improved: the OUT contours become visible and the nonphysical values are supressed. Nevertheless, the LQL model does not yield satisfactory quantitative images in the living tissue example, which illustrates its limitations.

On the other hand, the LQLR approximation is observed to offer a better fidelity of the reconstruction: the contours of the chicken wing are distinguishable and the quantitative values are largely correct (see Figure 5.23). Note that the de-noised data are used in this reconstruction. Better performance of the LQLR approximation is expected: the chicken

wing is an electrically large object at the given frequencies. However, we notice some nonphysical values in the reconstructed images: it is especially noticeable in the imaginary part of the relative permittivity (see Figure 5.23(b)). Note that these nonphysical values in the relative permittivity distributions for the LQL (Figure 5.21) and LQLR (Figure 5.23) approximations are close to each other. As shown above, the primary cause of this problem is the stochastic noise and measurement uncertainties present in the raw data. The de-noising algorithm is instrumental in reducing the nonphysical values substantially (see Figure 5.20 and Figure 5.21), but it cannot remove them completely. This is because the limitations of the forward model are violated in the living tissue experiment, which is yet another factor responsible for nonphysical solutions.

Again, we attempt to solve the non-physicality problem by employing the MOSEK solver with physicality constraints (5.1). It yields the same result as the *lsqlin* solver but at a faster time. We observe better image fidelity in case or the real part of the relative permittivity (see Figure 5.24(a)) compared to the one in Figure 5.23(a). The imaginary part does not improve significantly (see Figure 5.24(b)).

The challenging example of living-tissue imaging clearly demonstrates the limitations of the SPM, although reconstruction of a satisfactory fidelity is achievable due to the fact that the SPM can accommodate the Rytov forward model. The Rytov model is not limited by the target's size; therefore, the LQLR-based SPM is more likely to succeed in the near-field imaging of large tissue samples.

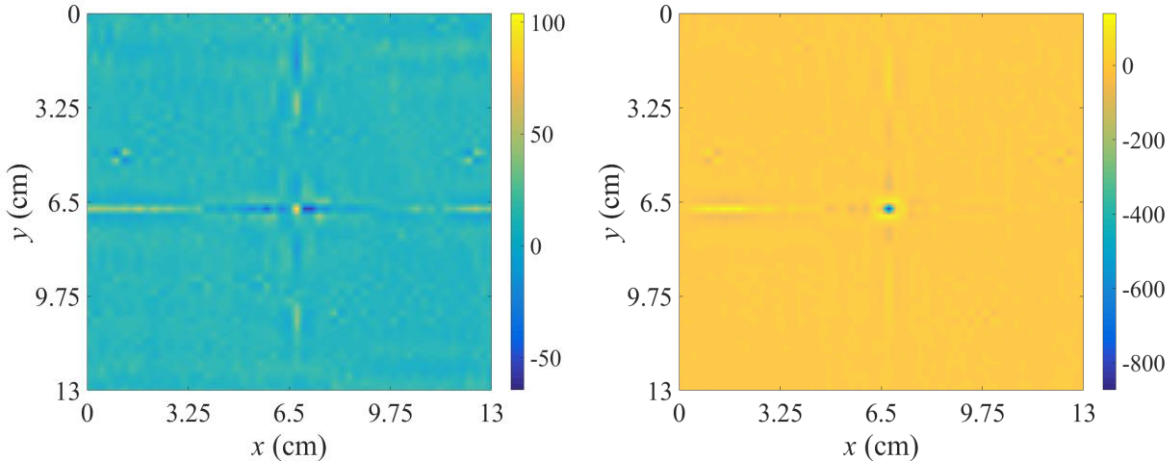

(a) (b)

Figure 5.20 Estimated relative permittivity in the living tissue experiment: (a) real part, (b) imaginary part. BCCB SPM with LQL approximation and BCCB solver are used.

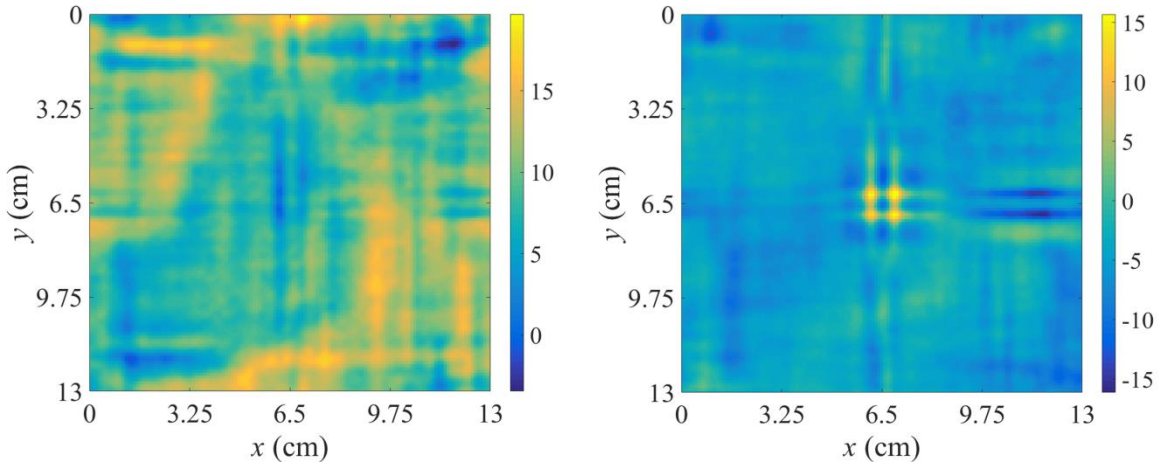

(a) (b)

Figure 5.21 Estimated relative permittivity in the living tissue experiment: (a) real part, (b) imaginary part. BCCB SPM with LQL approximation and BCCB solver are used. De-noising algorithm is applied to the CO data as well as the RO data.

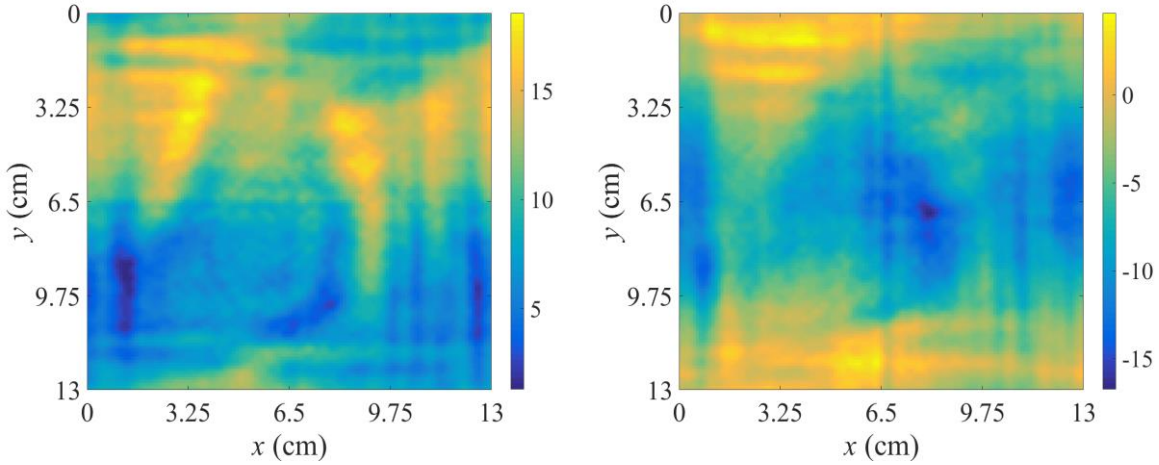

(a) (b)

Figure 5.22 Estimated relative permittivity in the living tissue experiment: (a) real part, (b) imaginary part. BCCB SPM with LQL approximation and BCCB solver are used. De-noising algorithm is applied to the CO data as well as the RO data. Gaussian apodization function is used.

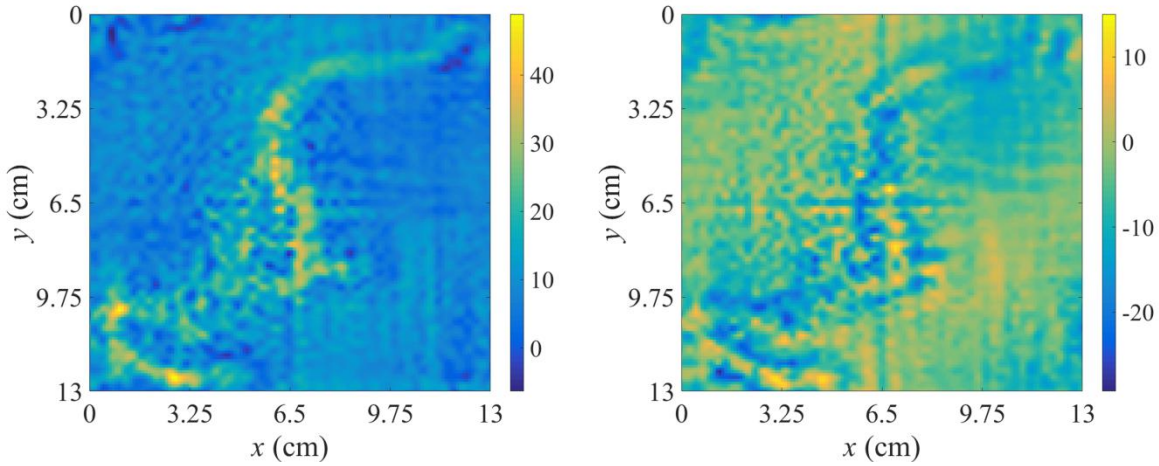

(a) (b)

Figure 5.23 Estimated relative permittivity in the living tissue experiment: (a) real part, (b) imaginary part. BCCB SPM with LQLR approximation and BCCB solver are used. De-noising algorithm is applied to the CO data as well as the RO data.

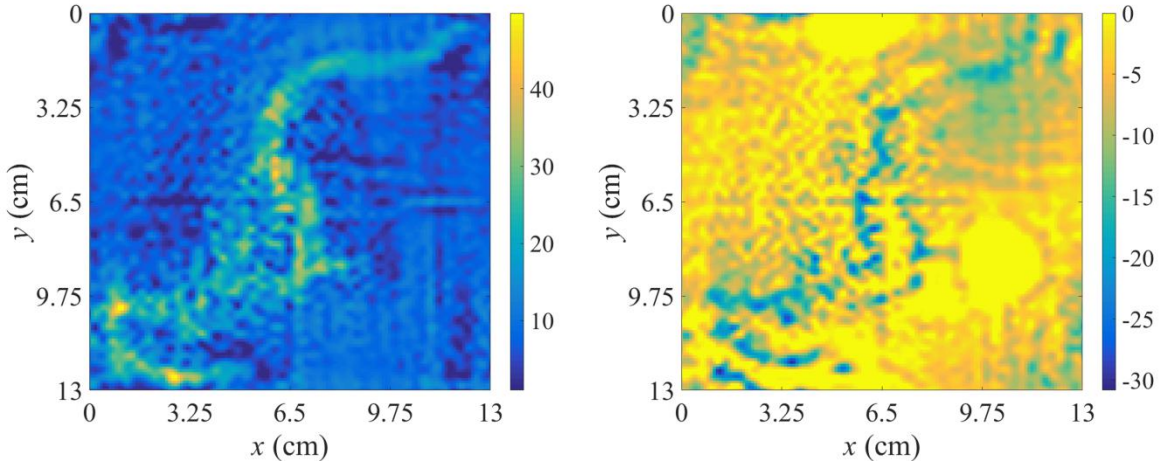

(a) (b)

Figure 5.24 Estimated relative permittivity in the living tissue experiment: (a) real part, (b) imaginary part. BCCB SPM with LQLR approximation and MOSEK solver are used. De-noising algorithm is applied to the CO data as well as the RO data.

5.3.2 Calibration with Metallic Scattering Probe

In order to achieve target-independent quantitative accuracy, the calibration strategy employing metallic scattering probe is proposed. Since its envisioned application is tissue imaging, here we report our first results in an example containing lossy media. It uses the simulated data obtained with FEKO [19].

5.3.2.1 Dielectric Objects in Lossy Medium

The imaging setup consists of two half-wavelength dipole antennas aligned along each other's boresight. The distance from the antennas' aperture to the OUT is 4 mm. The imaged area is 8 cm by 8 cm with 2 mm sampling step. The linearly spaced frequency samples are from 3 GHz to 5 GHz with 1 GHz step. Note that the physical antenna length is automatically adjusted at each frequency point.

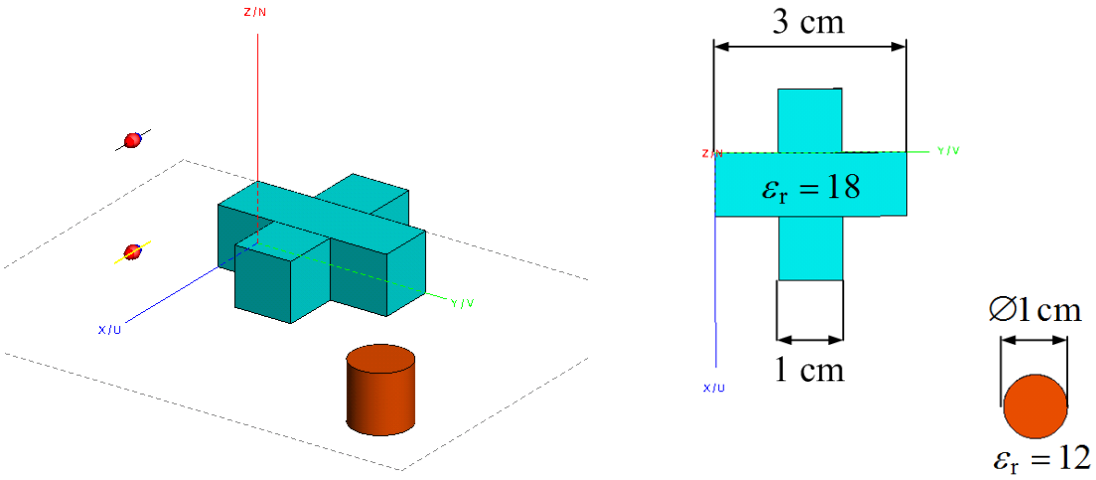

(a) (b)

Figure 5.25 Screenshots from FEKO of: (a) the simulation setup emulating the planar scan with two dipole antennas aligned along each other's boresight; (b) the top view of the OUT.

The OUT contains a dielectric cross of $\varepsilon_r \approx 18$ and a dielectric cylinder of $\varepsilon_r \approx 12$ (see Figure 5.25). The objects are 1 cm in height. The background medium in the RO is set to be of $\varepsilon_{r,RO} \approx 9.4 - i1.85$. Note that the RO relative permittivity value is required for the calculation of $\alpha^{(m)}$ in (2.11).

For the CO scan with the metallic scattering probe, we use a piece of wire of 5.5 mm length and 0.4 mm radius (see Figure 5.26(a)). It is positioned in accordance with the antennas' polarization. We also perform a CO scan with a dielectric scattering probe as shown in Figure 5.26(b). For that, a cube with 4 mm side and a relative permittivity of 15 is used.

In the case of the calibration with a metallic scattering probe, the scaling factor is calculated according to (2.29) or (2.30). Note that it is very sensitive to the parameters of the wire scatterer (e.g., length and radius) as well as the relative permittivity of the

background. In order to overcome this drawback, the controlled object with known permittivity distribution can be measured. Here, we use the dielectric cylinder of $\varepsilon_r \approx 12$ from the imaging setup shown in Figure 5.25. The value of the scaling factor can also be determined from the reconstruction of this controlled object. The so-obtained scaling factor value is in agreement with the one calculated analytically provided that the constraints for calculating $\alpha^{(m)}$ through (2.11) are met.

Since the images reconstructed with both methods are practically identical, only the results obtained with the convolution-based SPM are shown here. The LQL images in the case of the calibration with a metallic scattering probe are shown in Figure 5.27, whereas those in the case of the calibration with a dielectric scattering probe are shown in Figure 5.29. The respective LQLR images are shown in Figure 5.28 in the case of the calibration with metallic scattering probe and Figure 5.30 in the case of the calibration with dielectric scattering probe. Note that due to the specifics of the imaging setup (i.e., antenna polarization) the imaged objects do not appear symmetrical.

It is seen that the real part of the reconstructed relative permittivity is better in the case of the calibration with a metallic scattering probe (see Figure 5.27(a) and Figure 5.29(a) as well as Figure 5.28(a) and Figure 5.30(a)). Note that the scattering objects have much smaller contrast with the RO in the imaginary part of the relative permittivity compared to the real part. That is why, we observe a poor fidelity of reconstruction in the imaginary part (see Figure 5.27(b), Figure 5.28(b), Figure 5.29(b) and Figure 5.30(b)).

The presented simulation example validates the calibration with a metallic scattering probe for the quantitative reconstruction in near-field microwave imaging.

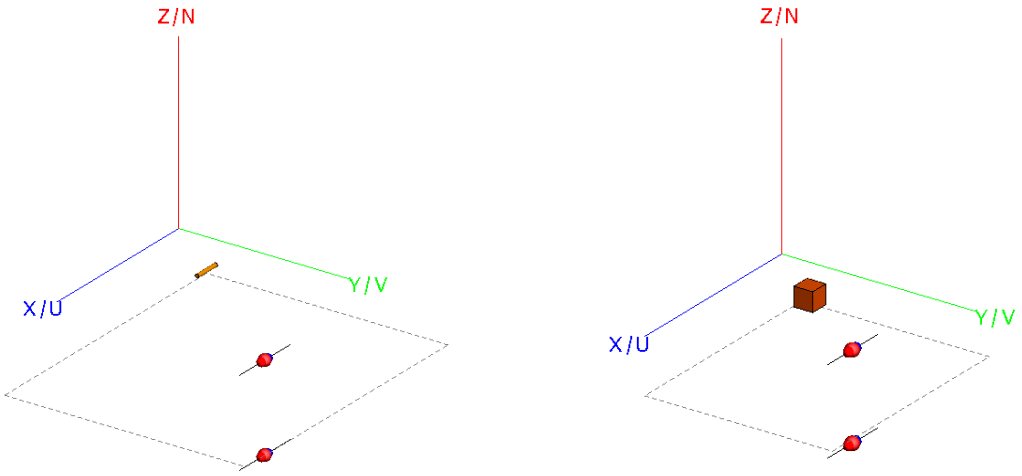

(a) (b)

Figure 5.26 Screenshots from FEKO of the simulation setup for the CO measurement with (a) metallic scattering probe and (b) dielectric scattering probe.

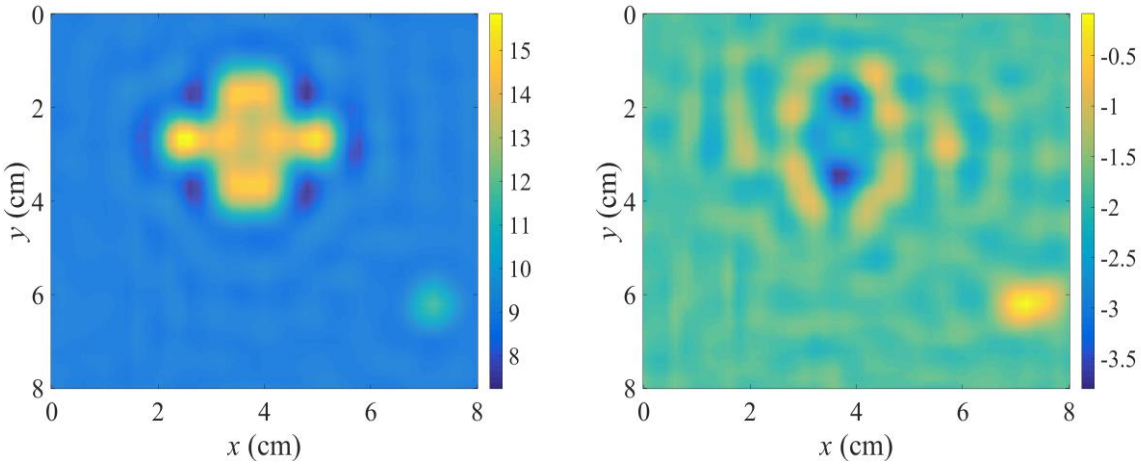

(a) (b)

Figure 5.27 Estimated relative permittivity in the case of calibration with a metallic scattering probe: (a) real part, (b) imaginary part. Convolution-based SPM with LQL approximation is used.

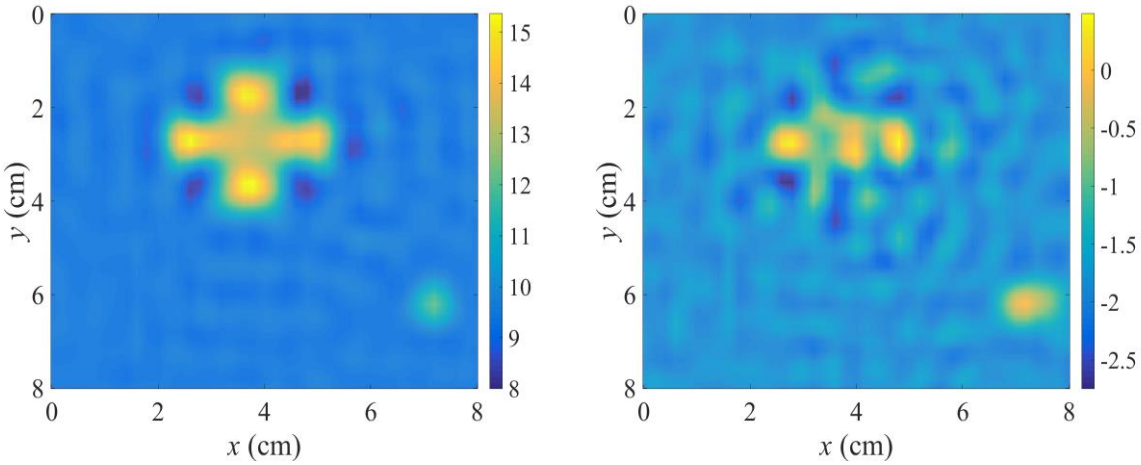

(a) (b)

Figure 5.28 Estimated relative permittivity in the case of calibration with a metallic scattering probe: (a) real part, (b) imaginary part. Convolution-based SPM with LQLR approximation is used.

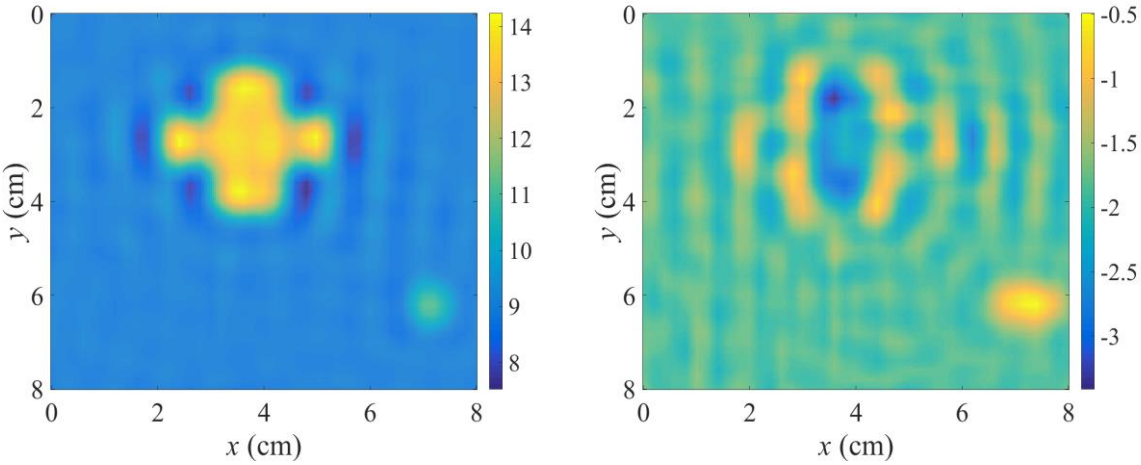

(a) (b)

Figure 5.29 Estimated relative permittivity in the case of calibration with a dielectric scattering probe: (a) real part, (b) imaginary part. Convolution-based SPM with LQL approximation is used.

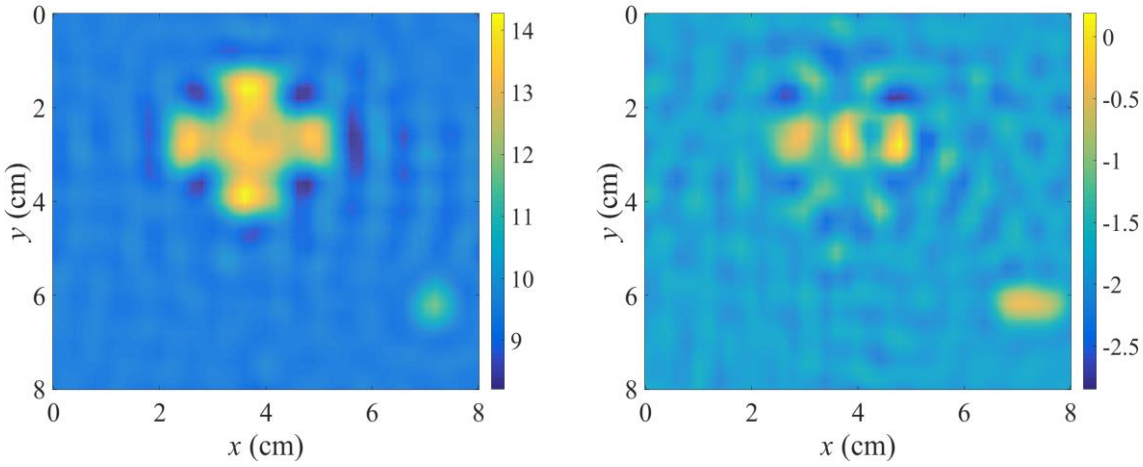

(a) (b)

Figure 5.30 Estimated relative permittivity in the case of calibration with a dielectric scattering probe: (a) real part, (b) imaginary part. Convolution-based SPM with LQLR approximation is used.

5.4 Three-Dimensional Imaging

Two 3D imaging experimental examples are presented here. Both of them employ calibration with a dielectric scattering probe. No power amplifiers are used since it prevents the acquisition of reflection coefficients. It is known that reflection data are crucial for range resolution, which is determined by the formula [13]

$$\delta_z \approx \frac{v_{\mathrm{RO}}}{2(f_{\max} - f_{\min})}, \tag{5.3}$$

where v_{RO} is the speed of light in the background medium. Note that the depth information can still be obtained with a power amplifier connected to transmitter if multiple viewing angles on the receiving side are available [20].

5.4.1 Reconstruction of Letter-Shaped Objects

The experimental setup consists of two open-ended WR42 waveguides with the distance between them being approximately 74 mm. The antennas operate in air. The data acquisition involves transmission and reflection measurements.

The OUT is suspended between the antennas. The distance from the antenna flanges to the OUT is 4 mm. It consists of the letter-shaped objects placed in a block of polystyrene with a thickness of 66 mm (see Figure 5.31). The objects shaped as letters *C* and *A* are fabricated from Eccostock HiK material [10]. As measured by a dielectric probe [12], its averaged relative permittivity value in the frequency range from 18 GHz to 25 GHz is $\varepsilon_{\mathrm{r,OUT}} \approx 4.8 - \mathrm{i}\,2.2$, whereas that of the polystyrene is $\varepsilon_{\mathrm{r,RO}} \approx 1.05 - \mathrm{i}\,0.03$. The width of the letters is 7 mm whereas the thickness is 22 mm (see Figure 5.31(a)). The maximum lateral dimension of the letter *A* is 65 mm. It is placed at the center of the bottom plane. The maximum lateral dimension of the letter *C* is 61 mm, and it is placed at the center of the top plane.

The CO is composed of the same polystyrene block with a dielectric cylinder of 5 mm diameter and 20 mm height embedded at the center of the imaged plane. The cylinder is made of a dielectric with $\varepsilon_{\mathrm{r,sc}} \approx 12$. The height of the scatterer is chosen to be approximately the same as that of the inspected objects. Since we aim at 3D reconstruction, the respective CO measurements are performed with the scattering probe at the center of each of the three *z* planes (see Figure 5.31(b)).

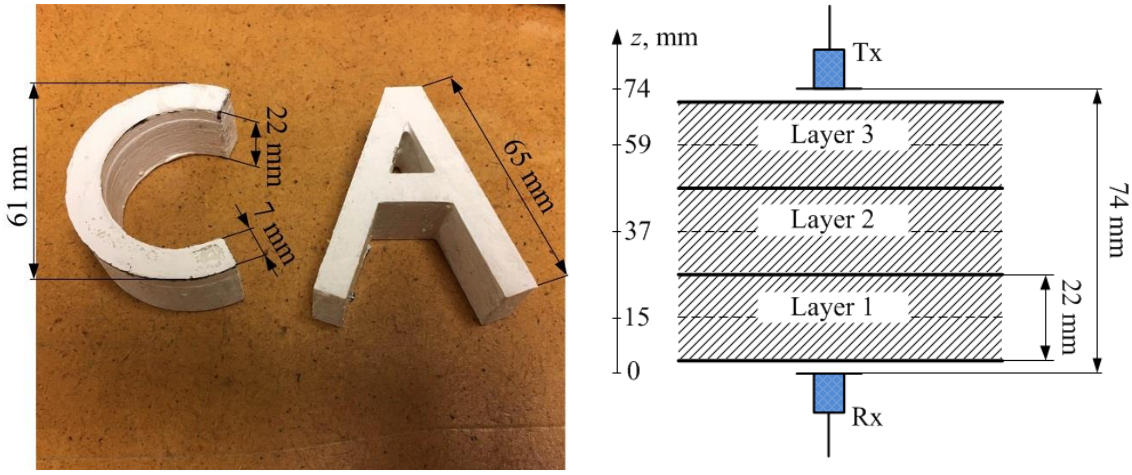

(a) (b)

Figure 5.31 (a) Photograph of the letters *C* and *A* with their respective dimensions. (b) Sketch of the imaged setup with OUT consisting of 22 mm thick layers.

The imaged area is 10 cm by 10 cm. The scanning step is 2 mm in both lateral directions. The frequency sweep is from 18 GHz to 25 GHz with 71 frequency samples. The VNA output power is 0 dBm.

Note that the calculated range resolution for the given frequency range is about 21 mm. Since the thickness of the fabricated *C* and *A* letters equals 22 mm, we should be able to distinguish them reasonably well in the range direction.

The raw data in this experiment have been acquired with the scanner shown in Figure 5.1(b). It can be seen that the metallic parts of the scanner have not been shielded. Even though these parts are not located in the immediate vicinity of the antennas, the raw data are strongly affected by the reflections from the metal (see Figure 5.32). Ideally, the resultant interference pattern should cancel when subtracting the RO signal from the CO signal. However, it is not always the case (see Figure 5.33). Consequently, the reconstruction fidelity is compromised. Some artifacts and nonphysical permittivity

values are observed in the images obtained with the convolution-based SPM (running time is about a second) shown in Figure 5.34, as well as in those obtained with the BCCB SPM (running time is several minutes) shown in Figure 5.35. We observe that the BCCB SPM reconstruction results are affected more by the background pattern in the raw data compared to the convolution-based SPM outcome.

Next, we attempt to improve the reconstruction fidelity by de-noising the measured data. The resultant images obtained with the convolution-based SPM and the BCCB SPM are shown in Figure 5.36 and Figure 5.37, respectively. The real parts of the relative permittivity are relatively similar (see Figure 5.36(a) and Figure 5.37(a)) whereas the imaginary part looks better in Figure 5.36(b). Also, we could state that the LQL reconstruction of the letter *C* with either the convolution-based SPM or the BCCB SPM is not satisfactory.

On the other hand, the LQLR approximation offers somewhat better reconstruction fidelity of the letter *C* with both methods (see Figure 5.38 and Figure 5.39). However, the imaginary part of the letter *A* is reconstructed poorly in Figure 5.38(b) and Figure 5.39(b). Also, we notice significant artifacts in the middle layer of the OUT when using the convolution-based SPM (see Figure 5.38).

Finally, since the reconstructed results contain nonphysical values, we employ the MOSEK solver with physicality constraints (5.1). The respective LQLR images are shown in Figure 5.40. It is seen that the imaginary part of the relative permittivity is

reconstructed poorly (see Figure 5.40). More importantly, using MOSEK in the case of the LQL approximation yields a non-convergent solution.

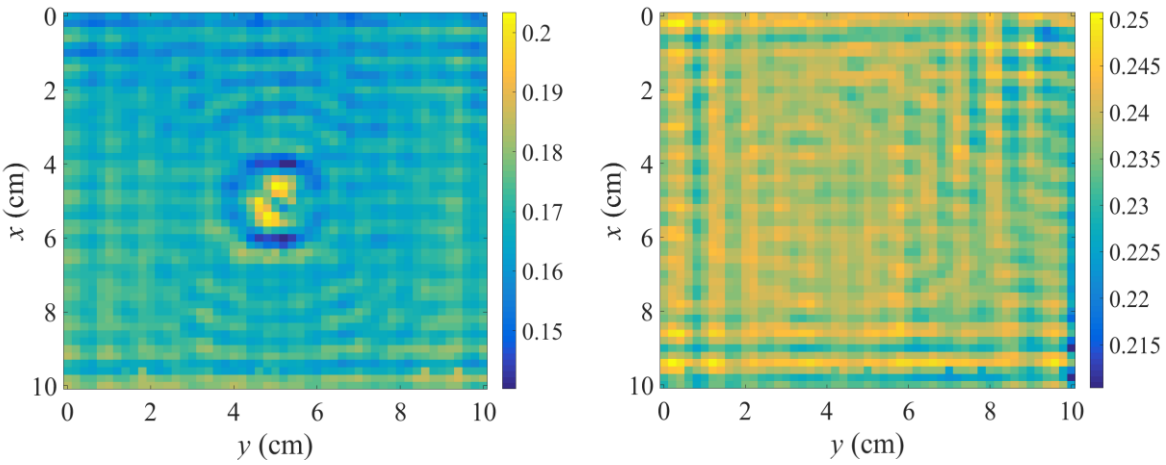

(a) (b)

Figure 5.32 Measured *S*-parameter data containing an interference pattern generated by the metallic parts of the scanner. (a) Modulus of the CO reflection (3rd layer) data at 21.9 GHz. (b) Modulus of the RO reflection data at 21.9 GHz.

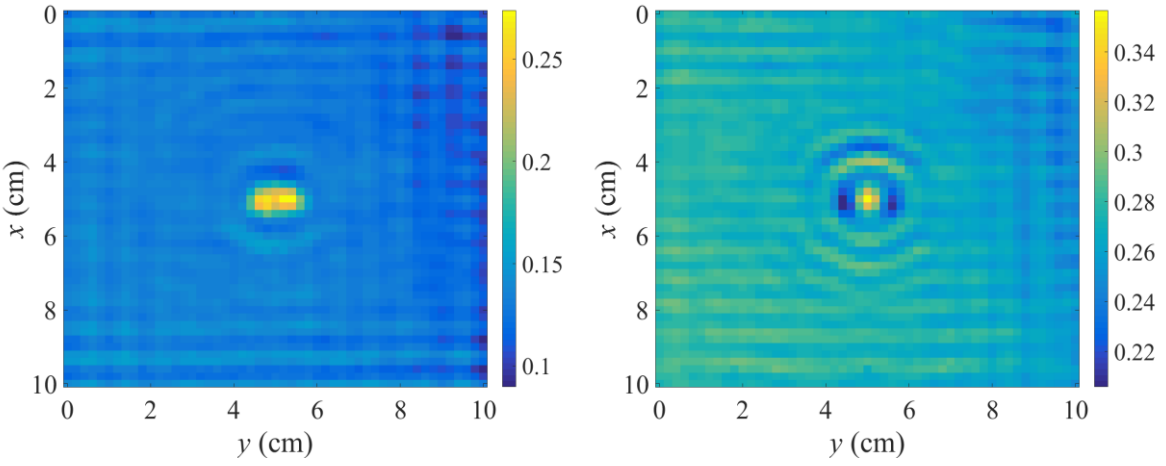

(a) (b)

Figure 5.33 Modulus of the CO scattered response obtained by subtracting the RO signal from the CO signal at: (a) 21.9 GHz and (b) 24 GHz.

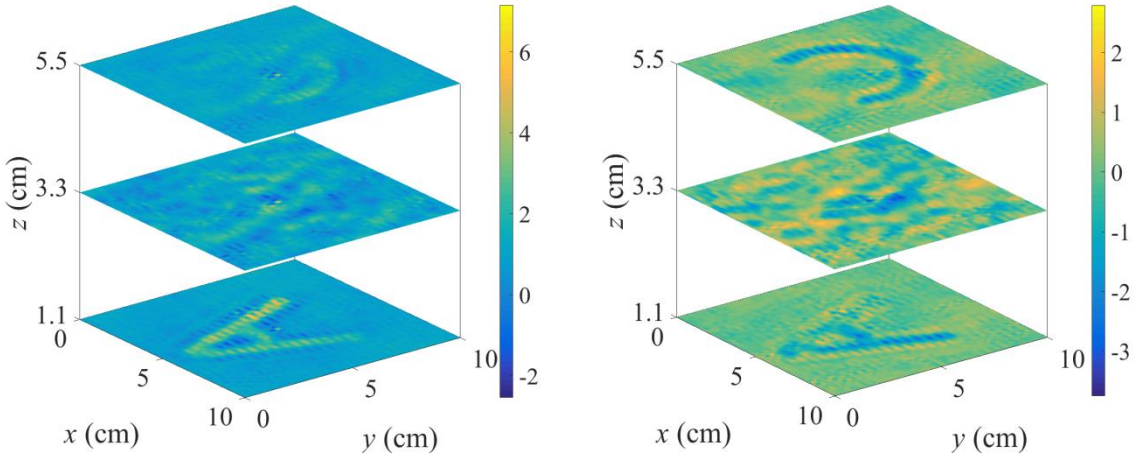

(a) (b)

Figure 5.34 Estimated relative permittivity of the letter-shaped objects using reflection data: (a) real part, (b) imaginary part. Convolution-based SPM with LQL approximation is used.

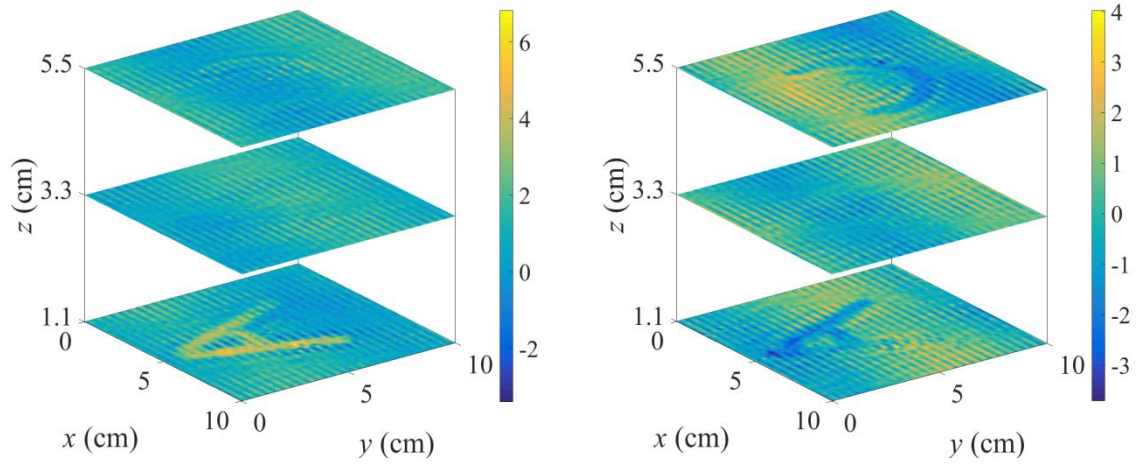

(a) (b)

Figure 5.35 Estimated relative permittivity of the letter-shaped objects using reflection data: (a) real part, (b) imaginary part. BCCB SPM with LQL approximation and BCCB solver are used.

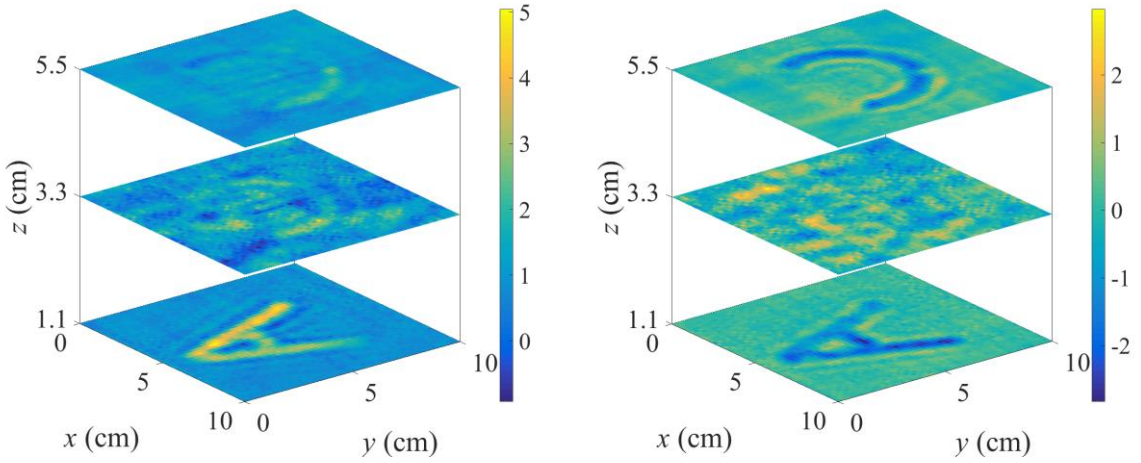

(a) (b)

Figure 5.36 Estimated relative permittivity of the letter-shaped objects using reflection data: (a) real part, (b) imaginary part. Convolution-based SPM with LQL approximation is used. De-noising algorithm is applied to the CO data as well as the RO data.

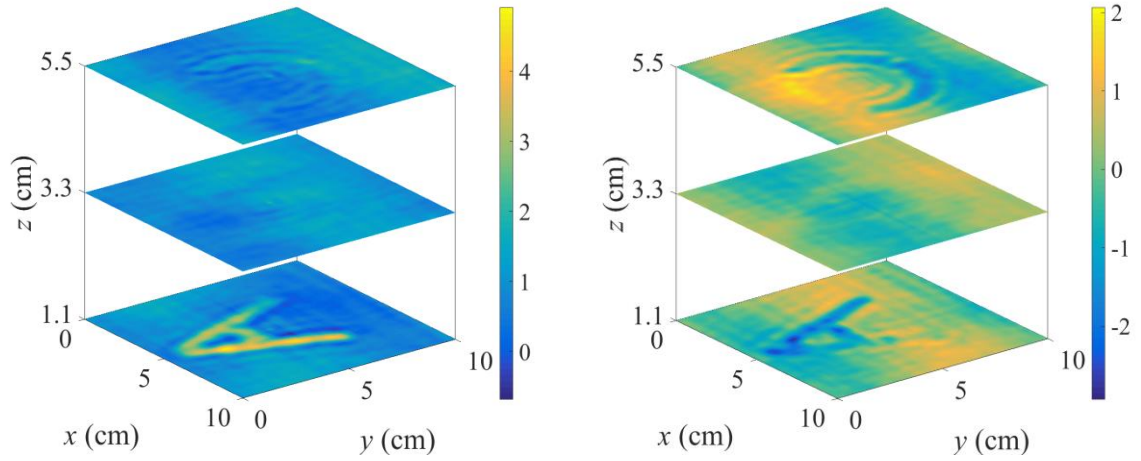

(a) (b)

Figure 5.37 Estimated relative permittivity of the letter-shaped objects using reflection data: (a) real part, (b) imaginary part. BCCB SPM with LQL approximation and BCCB solver are used. De-noising algorithm is applied to the CO data as well as the RO data.

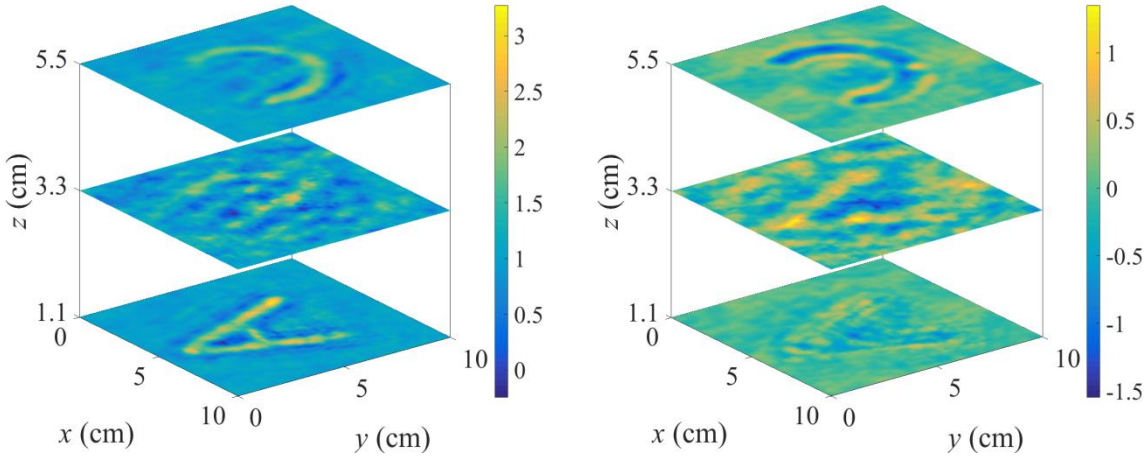

(a) (b)

Figure 5.38 Estimated relative permittivity of the letter-shaped objects using reflection data: (a) real part, (b) imaginary part. Convolution-based SPM with LQLR approximation is used. De-noising algorithm is applied to the CO data as well as the RO data.

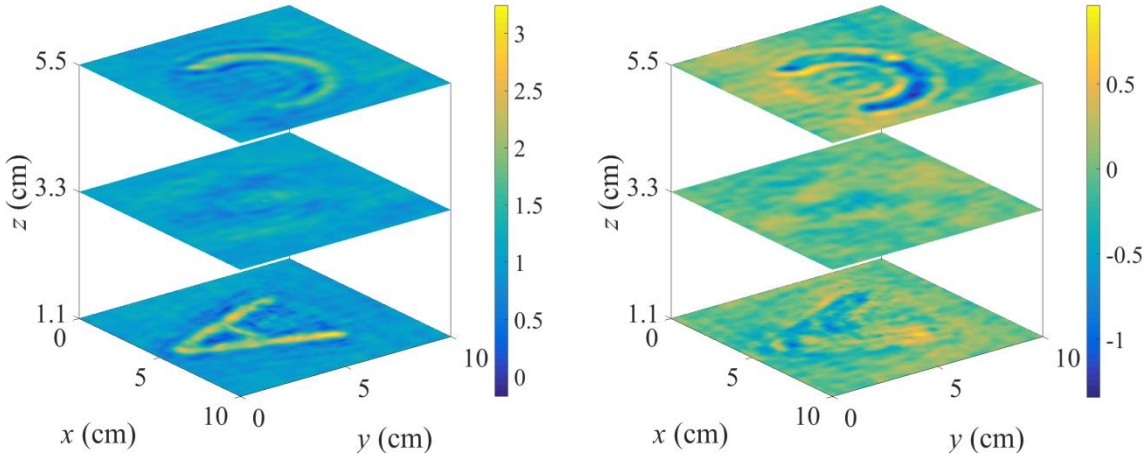

(a) (b)

Figure 5.39 Estimated relative permittivity of the letter-shaped objects using reflection data: (a) real part, (b) imaginary part. BCCB SPM with LQLR approximation and BCCB solver are used. De-noising algorithm is applied to the CO data as well as the RO data.

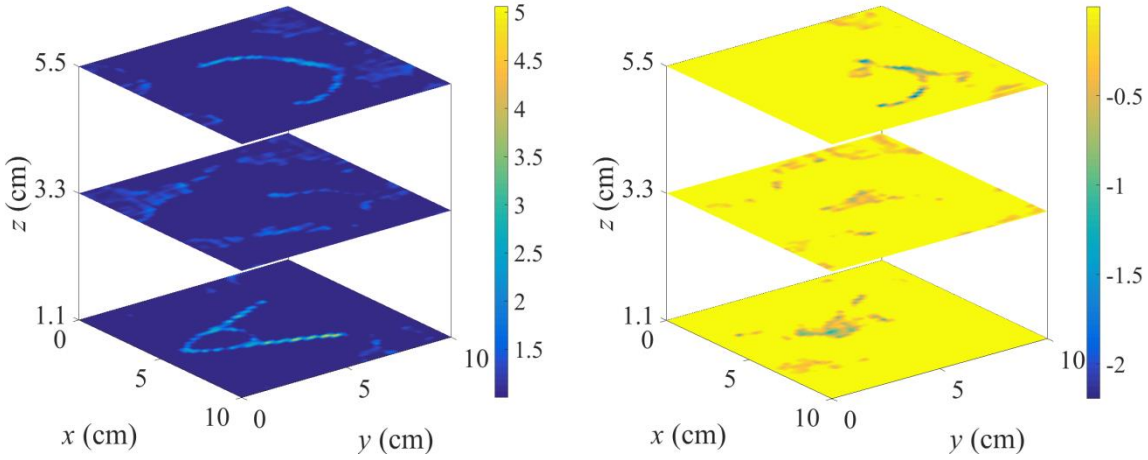

(a) (b)

Figure 5.40 Estimated relative permittivity of the letter-shaped objects using reflection data: (a) real part, (b) imaginary part. BCCB SPM with LQLR approximation and MOSEK solver are used. De-noising algorithm is applied to the CO data as well as the RO data.

5.4.2 Reconstruction of Synthetic Multilayered Object

For the next example, a five-layer synthetic object shown in Figure 5.41(a), (b) and (c) has been scanned. The top and bottom OUT layers are made of a 3 mm dielectric sheet with $\varepsilon_r \approx 12$. The other three layers are 20x20x1 cm^3 absorber sheets with relative permittivity of $\varepsilon_r \approx 10 - i5$. The second layer from the bottom contains a dielectric cross of $\varepsilon_r \approx 18$, a dielectric cylinder of $\varepsilon_r \approx 12$ and four dielectric cylinders of $\varepsilon_r \approx 15 - i0.003$ [10]. All these objects are embedded in the absorbing material with $\varepsilon_r \approx 10 - i5$ as seen in Figure 5.41(b). The third layer from the bottom does not contain inclusions. The fourth layer from the bottom contains a dielectric cross of $\varepsilon_r \approx 12$ positioned at the center (see Figure 5.41(c)). All the cylinders used in this experiment are 1 cm in diameter and 1 cm in height.

Two TEM horn antennas [16] are aligned along each other's boresight and move in a planar raster fashion. The output power of the vector network analyzer (VNA) is 5 dBm. The imaged area is 13 cm by 13 cm with 2 mm sampling step. Both reflection and transmission coefficients are acquired.

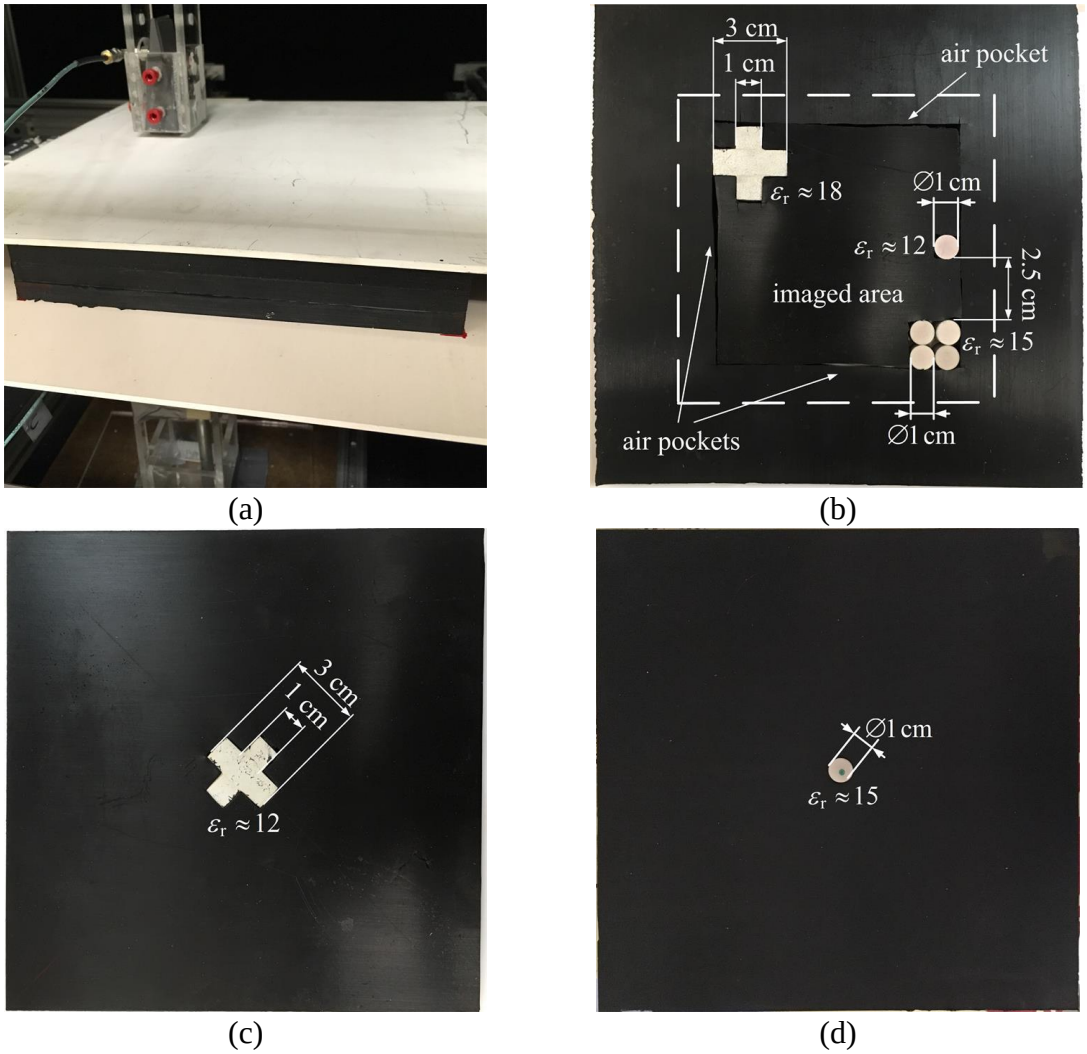

(a) (b)

(c) (d)

Figure 5.41 Photographs of (a) imaging setup with five-layer OUT, (b) second (from the bottom) layer of OUT with 13 cm by 13 cm imaged area (dashed white line), (c) fourth (from the bottom) layer of OUT with a dielectric cross, and (d) CO layer with a dielectric cylinder serving as a scattering probe.

The RO is comprised of two dielectric sheets and three absorber sheets resembling the OUT's structure with no scattering objects. For the CO scan, we use a dielectric cylinder of 1 cm diameter and 1 cm height, with the relative permittivity of $\varepsilon_{r,sc} \approx 15 - i0.003$. This cylinder is in succession embedded in the center of each of the three absorber sheets comprising the RO. These are the three CO measurements, which provide the PSFs needed to generate the images at the corresponding range locations z = 0.8 cm, 1.8 cm and 2.8 cm, with the origin being at the bottom of the OUT.

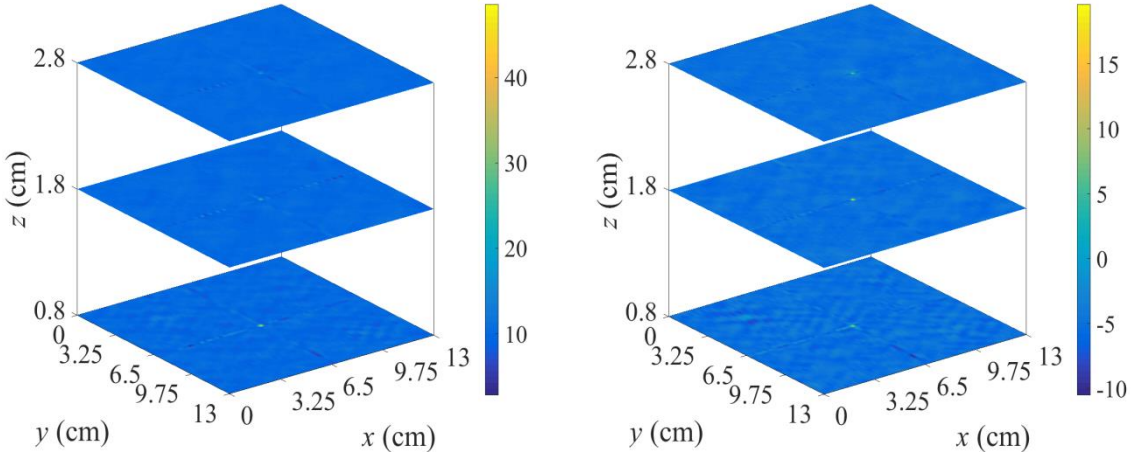

(a) (b)

Figure 5.42 Estimated relative permittivity of the five-layer OUT: (a) real part, (b) imaginary part. BCCB SPM with LQL approximation and BCCB solver are used. De-noising is not applied.

The reconstruction results obtained with the SPM employing the LQL approximation are shown in Figure 5.42. We do not see the imaged objects due to the strong artifacts present in both the real and the imaginary parts of the relative permittivity. Applying the de-noising algorithm to the RO and CO data improves the fidelity of reconstruction

significantly (see Figure 5.43). Also, note that there are no nonphysical values in the resultant images.

As the next step, we employ the LQLR approximation with the respective results shown in Figure 5.44. We observe superior quality of the reconstruction in comparison with the LQL approximation, especially in the imaginary part of the OUT permittivity (see Figure 5.43(b) and Figure 5.44(b)). Also, we are able to see the air pockets contained in the layer at $z = 0.8$ cm (see Figure 5.41(b) and Figure 5.44).

It should be noted that the LQL and LQLR results obtained with the BCCB SPM are similar to those obtained with the convolution-based SPM. However, due to the relatively large computational size of the problem, the BCCB SPM realized in MATLAB takes hours. On the other hand, the convolution-based SPM (also realized in MATLAB) requires a few seconds to produce the result, which makes it the number one tool for solving weak-scattering problems with hundreds of thousands of unknowns.

This experiment also exemplifies the limitations of the proposed linear reconstruction methodology. The reconstructed real part of the OUT permittivity with both the LQL and LQLR approximations is not satisfactory (see Figure 5.43(a) and Figure 5.44(a)). This is due to two main factors. First, the scattering objects have much less contrast with the background (the RO) in the real part of the permittivity compared to the imaginary part. Second, the RO is layered, where the top and bottom low-loss slabs differ in their permittivity from the middle three layers, which have significant loss and lower permittivity. At the same time, the top and bottom slabs are right next to the inclusions,

which leads to strong coupling with them. This effect cannot be captured by the measured PSFs (the CO measurements), neither can it be accounted for by the linearized inversions based on the LQL and the LQLR approximations.

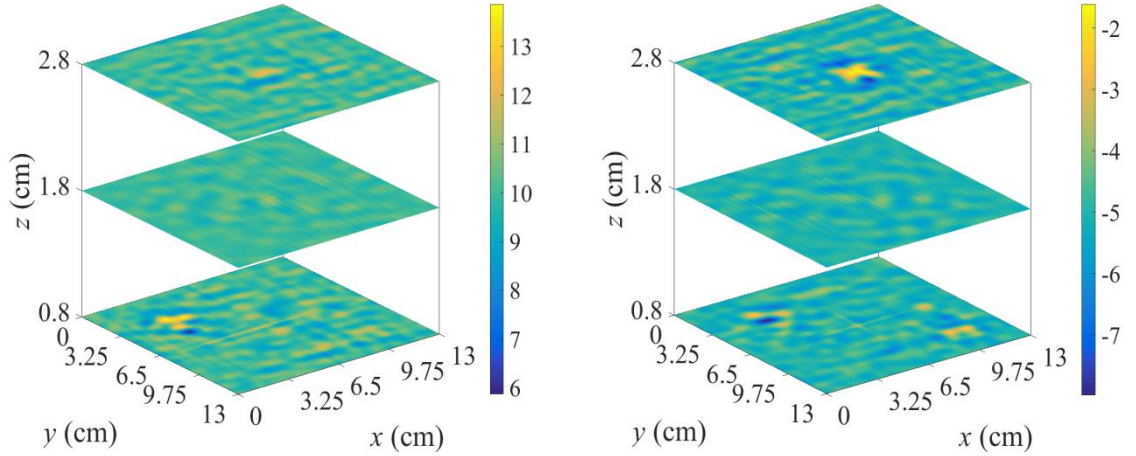

(a) (b)

Figure 5.43 Estimated relative permittivity of the five-layer OUT: (a) real part, (b) imaginary part. BCCB SPM with LQL approximation and BCCB solver are used. De-noising algorithm is applied to the CO data as well as the RO data.

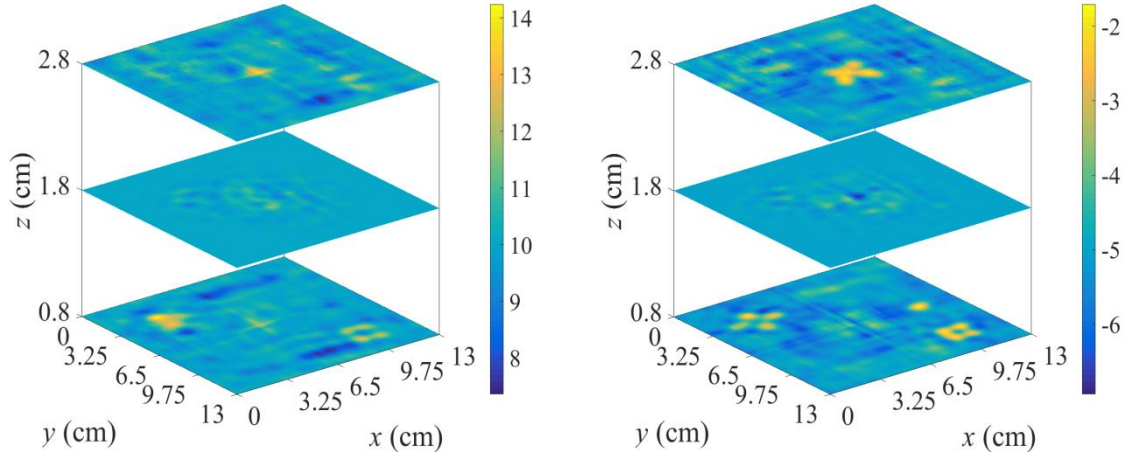

(a) (b)

Figure 5.44 Estimated relative permittivity of the five-layer OUT: (a) real part, (b) imaginary part. BCCB SPM with LQLR approximation and BCCB solver are used. De-noising algorithm is applied to the CO data as well as the RO data.

References

[1] J. C. Lin, "Frequency optimization for microwave imaging of biological tissues," *Proc. IEEE*, vol. 73, no. 2, pp. 374–375, Feb. 1985.

[2] N. K. Nikolova, "Microwave biomedical imaging," *Wiley Encyclopedia of Electrical and Electronics Engineering*, pp. 1–22. (published online Apr. 25, 2014).

[3] K. Khare. *Fourier Optics and Computational Imaging*. Chichester, U.K.: John Wiley & Sons, 2016, p. 198.

[4] E. W. Weisstein. "Apodization Function." From MathWorld–A Wolfram Web Resource. http://mathworld.wolfram.com/ApodizationFunction.html

[5] D. D. Traficante and G. A. Nemeth, "A new and improved apodization function for resolution enhancement in NMR spectroscopy," *J. Magn. Reson.*, vol. 71, no. 2, pp. 237–245, Feb. 1987.

[6] F. J. Harris, "On the use of windows for harmonic analysis with the discrete Fourier transform," *Proc. IEEE*, vol. 66, pp. 51–83, Jan. 1978.

[7] P. Giraudeau and S. Akoka, "Sensitivity and lineshape improvement in ultrafast 2D NMR by optimized apodization in the spatially encoded dimension," *Magnet. Reson. Chem.*, vol. 49, no. 6, pp. 307–313, Jun. 2011.

[8] S. Tu, J. J. McCombe, D. S. Shumakov, and N. K. Nikolova, "Fast quantitative microwave imaging with resolvent kernel extracted from measurements," *Inverse Problems*, vol. 31, no. 4, 33 pp., Mar. 2015.

[9] D. S. Shumakov, S. Tu, and N. K. Nikolova, "Fast quantitative microwave imaging based on measured point spread functions and inversion in real space," *IEEE AP-S/URSI Int. Symp. Antennas Propag.*, pp. 687–688, Jul. 2015.

[10] Emerson & Cuming Microwave Products Inc. Randolph, MA, USA. Unit of Laird Technologies.

[11] D. S. Shumakov, A. S. Beaverstone, D. Tajik, and N. K. Nikolova, "Experimental investigation of axial-null and axial-peak illumination schemes in microwave imaging," *IEEE AP-S/URSI Int. Symp. Antennas Propag*., pp. 849–850, Jun.-Jul. 2016.

[12] Agilent 85070E Dielectric Probe Kit, Keysight Technologies Inc., USA (www.keysight.com).

[13] D. S. Shumakov, A. S. Beaverstone, and N. K. Nikolova, "Optimal illumination schemes for near-field microwave imaging," *Progress In Electromagnetics Research*, vol. 157, pp. 93–110, 2016.

[14] CVX Research Inc., 2012. http://web.cvxr.com/cvx/beta/doc/mosek.html#mosek

[15] MATLAB R2016a. The MathWorks Inc., Natick, MA, USA, 2016.

[16] R. K. Amineh, M. Ravan, A. Trehan, and N. K. Nikolova, "Near-field microwave imaging based on aperture raster scanning with TEM horn antennas," *IEEE Trans. Antennas Propag*., vol. 59, no. 3, pp. 928–940, Mar. 2011.

[17] Taconic CER-10 RF & Microwave Laminate, High DK Material.

[18] M. Redivo-Zaglia, and G. Rodriguez, "SMT: a MATLAB toolbox for structured matrices," *Numer. Algor*., vol. 59, no. 4, pp. 639–659, Apr. 2012.

[19] FEKO Suite 7.0.1 for Altair. EM Software & Systems – S. A. (Pty) Ltd., USA (www.feko.info).

[20] R. K. Amineh, M. Ravan, J. McCombe, and N. K. Nikolova, "Three-dimensional microwave holographic imaging employing forward-scattered waves only," *Int. J. Antennas Propag*., vol. 2013, Article ID 897287, 15 pp., 2013.

Chapter 6

Axial-Null Illumination for Near-Field Microwave Imaging

6.1 Introduction

Recent efforts in microwave imaging target a variety of short-range applications such as concealed weapon detection, through-the-wall imaging, non-destructive testing and evaluation, biomedical diagnostics, etc. [1]-[6]. The scanning hardware usually employs acquisition surfaces of canonical shapes: planar, cylindrical, or hemispherical, which simplifies the reconstruction process. The data (back-scattered and/or forward-scattered signals) can be acquired either through mechanical scanning or through electronically-switched arrays. The transmitting antennas are designed to conform to the respective surface shape and to have the radiation maximum more or less along boresight and aiming at the center of the examined volume. This design choice achieves stronger scattering signals from possible targets—the stronger the illumination is, the stronger the scattered field. Further, in forward-scattered (transmission coefficient) data acquisition, it is customary to align at least one of the receiving antennas (the sensors) along the transmitters' boresight in order to minimize the signal path, thereby maximizing the signal strength. In back-scattered (reflection coefficient) data acquisition, it is customary

to use the same antenna as a transmitter and a receiver along with a duplexing device that separates the incoming (reflected) signal from the outgoing (transmitted) one.

Multi-illumination configurations, also known as illumination-diversity techniques, have been used widely in microwave imaging [7]-[15]. At the expense of increased hardware complexity, such configurations allow for more accurate target shape reconstruction and localization. This is a consequence of collecting data from multiple perspectives. Illumination diversity along with frequency diversity can drastically improve the performance of microwave imaging provided the design of the system is optimal.

It is known that multi-illumination data improve the spatial resolution [8]-[15]. Since the object under test (OUT) is simultaneously illuminated by multiple sources, the scattered signals produce a coherent summation of the field due to a scattering center. For example, in diffraction tomography, this improves the image angular resolution, which is equivalent to reducing the necessary rotation angles [8][9]. In the quasi-monostatic frequency-swept imaging system in [8], three transmitting antennas are used, the boresight axes of which are at 0°, 30° and -30° angles with respect to the radial line through the center of the imaged plane. At the same time, the receiving antenna boresight is at an angle of 0°. This leads to three-fold improvement in the spatial resolution compared to a single-source illumination using the same angular sampling rate.

Microwave multi-static tomography systems such as [11]-[15] can also achieve improvement in resolution due to the multiple viewing angles. Such systems employ

circular switched arrays where, at each measurement, one antenna transmits and all others receive. However, due to reciprocity, the acquired signals can also be interpreted as due to multiple transmitters with a single receiver. Similarly, the reciprocity concept has been exploited in the ultrawideband (UWB) radar systems such as that in [10] where only one antenna transmits and 24 antennas receive back-scattered signals. A major advantage of the radar-based imaging over the tomographic imaging is its relatively simple and robust signal processing [16]. Some examples of the multi-static UWB radar microwave imaging systems are presented in [17] and [18]. They employ 31 antennas which can operate as transmitters or as receivers: while one antenna transmits, the measured field is acquired by the remaining 30 antennas.

Finally, the different strategies can be combined in order to achieve an improved resolution. These strategies can be algorithmic such as multi-resolution iterative inversion or edge preserving regularization, and hardware-oriented such as multi-illumination or multi-frequency excitation. For example, a multi-illumination setup used in conjunction with the multi-resolution iterative inversion is discussed in [19]-[21].

This chapter starts with the presentation of a rigorous theory of the spatial resolution for the case of multi-illumination schemes. The cross-range resolution limits with planar scanning are derived analytically in the far zone allowing for a comparison between the conventional single-source illumination and the double-source illumination. These limits are then validated through an inversion with SPM. The reconstruction is applied to two sets of simulated data acquired by a four-antenna array and by the conventional illumination. The respective images provide the estimated resolution limits in both cases.

Next, the axial-null illumination for near-field microwave imaging is introduced. In addition to the improved cross-range resolution, the important advantage of the proposed illumination scheme is that it eliminates the need for background (or baseline) measurements, thus simplifying the system calibration.

6.2 Analytical Investigation of Spatial Resolution Limits

6.2.1 Cross-Range Resolution

To estimate the cross-range resolution limit, consider the planar scanning scenario depicted in Figure 6.1. The scan is along *x* and *y* whereas *z* is the depth (or range) direction. It is assumed that the scatterer lies in a fixed cross-range plane $z = z_0$ where its contrast function is given by $f(x', y', z_0)$. Under the linear Born approximation, a signal in a planar acquisition can be viewed as the 2D convolution of the contrast function and the point-spread function (PSF) of the measurement system S_0 [22]:

$$S(x, y, z_A) = \int_{x'} \int_{y'} f(x', y', z_0) \cdot S_0(x - x', y - y', z_0)\, dx' dy' , \tag{6.1}$$

where z_A is the fixed *z*-coordinate of the acquisition plane whereas *x* and *y* indicate the location of the measurement point. $S_0(x, y, z_0)$ is a short-hand notation for

$$S_0(x, y, z_0) \equiv S_\delta(x, y, z_A; 0, 0, z_0) \tag{6.2}$$

and it describes the system's centered PSF, i.e., the signal recorded at (x, y, z_A), when a point (δ-function) scatterer is located at the center $(0, 0, z_0)$ of the imaged plane. The subscript in S_δ emphasizes that this signal is due to a point scatterer.

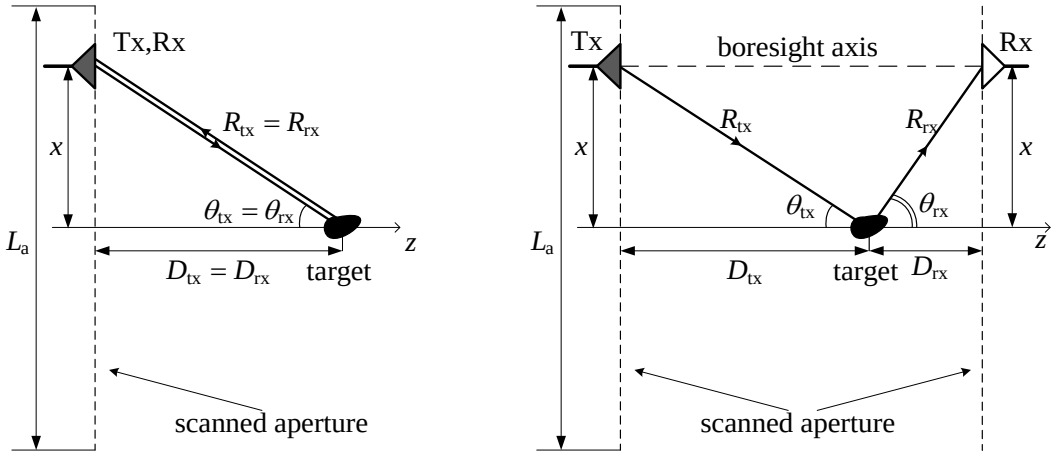

Figure 6.1 Illustration of the antenna and target positions in planar raster scanning in the case of conventional single antenna illumination: (a) monostatic, (b) bi-static.

In Fourier (or *k*) space, (6.1) can be written as

$$\tilde{S}(k_x, k_y, z_A) = \tilde{f}(k_x, k_y, z_0) \cdot \tilde{S}_0(k_x, k_y, z_0), \tag{6.3}$$

which allows for expressing the 2D Fourier transform (FT) of the unknown contrast function as

$$\tilde{f}(k_x, k_y, z_0) = \frac{\tilde{S}(k_x, k_y, z_A)}{\tilde{S}_0(k_x, k_y, z_0)}. \tag{6.4}$$

Here, $\tilde{S}$ and $\tilde{S}_0$ denote the 2D FTs of S and S_0, respectively. It should be noted that (6.4) is not used directly in practical inversion schemes because $\tilde{S}_0(k_x, k_y, z_0)$ may have near-zero values, or a system of equations based on (6.3) may be ill-posed and/or over-determined. Here, (6.4) is used only to illustrate the impact of the limits of the signal extent in *k*-space on the spatial resolution and to estimate the limits of this resolution.

Assuming that (6.4) is valid, the contrast function can be reconstructed using

$$\hat{f}(x, y, z_0) = \mathcal{F}_{2D}^{-1}\left\{\frac{\tilde{S}(k_x, k_y, z_A)}{\tilde{S}_0(k_x, k_y, z_0)}\right\}, \tag{6.5}$$

where $\mathcal{F}_{2D}^{-1}$ denotes the 2D inverse FT and $\hat{f}$ is the estimate of *f*.

Consider a point scatterer at (x_0, y_0) in the z_0 plane. Its contrast function is defined as

$$f_\delta(x, y) = \delta(x - x_0)\delta(y - y_0). \tag{6.6}$$

In 2D *k*-space, this scatterer appears as:

$$\tilde{f}_\delta(k_x, k_y, z_0) = e^{-\mathrm{i}k_x x_0 - \mathrm{i}k_y y_0}. \tag{6.7}$$

From (6.3), the FT of the system PSF is obtained as

$$\tilde{S}_\delta(k_x, k_y, z_A) = e^{-\mathrm{i}k_x x_0 - \mathrm{i}k_y y_0} \cdot \tilde{S}_0(k_x, k_y, z_0). \tag{6.8}$$

Substituting (6.8) into (6.5) produces the reconstructed contrast function, which is in the form of a 2D *sinc* function (centered at x_0, y_0) due to the finite spectral range limited

between $-k_\xi^{\max}$ and $+k_\xi^{\max}$, $\xi = x, y$. These limits depend on the spectral content of $\tilde{S}_0$, which in turn depends on the size of the scanned aperture as well as the transmitting and receiving antenna radiation patterns. The first null of the *sinc* function, which estimates the actual δ-function contrast, determines the cross-range resolution limits as:

$$\delta_x = \frac{\pi}{k_x^{\max}},\ \delta_y = \frac{\pi}{k_y^{\max}}. \tag{6.9}$$

Thus, the available spectral width in *k*-space is critical in improving the cross-range resolution. Also, note that (6.5) is an approximation that yields the best possible resolution for the given spectral limits. As the scatterer moves from the center of the imaged scene and toward the edge of the acquisition aperture, the cross-range resolution will deteriorate.

6.2.1.1 Conventional Boresight Illumination

In order to compare the spectral width of the signals acquired with the conventional boresight illumination and those acquired with ANI, it is beneficial to analyze the simplified problem of a linear scan along the *x*-axis where the target is in the far zone of the transmitting (Tx) and the receiving (Rx) antennas. Let *x* be the position of the Tx/Rx antenna pair with respect to the target (see Figure 6.1). The faster the acquired signal *S*(*x*) changes with *x*, the broader its spectrum is in k_x space. Thus, increasing the sensitivity of the signal dS/dx is equal to increasing the spectral width $k_x^{\max}$, which in turn means better resolution.

As discussed before, the available spectral range in Fourier space is determined by that of the system PSF, $S_0(x, z_0)$, which is the signal acquired at x when a point scatterer is located at $(x_0 = 0, z_0)$; see (6.2). Let z_0 be such that the range distances from the scatterer to the planes of the transmitter and the receiver are D_{tx} and D_{rx}, respectively; see Figure 6.1. For simplicity, we consider the scenario where the receiving and transmitting antennas are co-located (see the monostatic-case illustration in Figure 6.1(a)) or they are on the opposite sides of the target but scan together the x-line while remaining aligned along each other's boresight (see the bistatic-case illustration in Figure 6.1(b)). The scanned aperture has length L_{a} so that $x \in [-0.5L_{\text{a}}, 0.5L_{\text{a}}]$.

The far-zone assumption allows for neglecting the amplitude variation of the received signal, so that

$$S_0(x) \approx S_{\text{a}}(x) = e^{-\text{i}k(R_{\text{tx}} + R_{\text{rx}})}. \tag{6.10}$$

Here, $R_{\text{tx}}(x) = \sqrt{D_{\text{tx}}^2 + x^2}$ and $R_{\text{rx}}(x) = \sqrt{D_{\text{rx}}^2 + x^2}$. The subscript in S_{a} emphasizes that the expression is only approximate. The signal derivative with respect to x is found as

$$\frac{dS_{\text{a}}}{dx} = -\text{i}k(\sin\theta_{\text{tx}} + \sin\theta_{\text{rx}}) \cdot S_{\text{a}}(x), \tag{6.11}$$

where $\sin\theta_{\text{tx}} = x / R_{\text{tx}}$ and $\sin\theta_{\text{rx}} = x / R_{\text{rx}}$. It is apparent that the maximum derivative occurs at the largest values of θ_{tx} and θ_{rx}, i.e., when the antennas are at the edge of the aperture:

$$\sin\theta_{\text{tx}}^{\max} = \frac{L_{\text{a}}}{2R_{\text{tx}}};\ \sin\theta_{\text{rx}}^{\max} = \frac{L_{\text{a}}}{2R_{\text{rx}}}. \tag{6.12}$$

Therefore, the signals acquired at the aperture's edge contribute to the highest spectral content of $\tilde{S}_0(k_x)$. The spatial frequencies of this content can be estimated by taking the Fourier transform of (6.11) where $\sin\theta_{\text{tx}}$ and $\sin\theta_{\text{rx}}$ are assumed relatively constant (with respect to *x*) close to their maximum values. This yields the estimate of the maximum spatial frequency as

$$\left|k_x^{\max}\right| \approx k(\sin\theta_{\text{tx}}^{\max} + \sin\theta_{\text{rx}}^{\max}). \tag{6.13}$$

In the best-case scenario, $\theta_{\text{tx}}^{\max} \to 90^\circ$ and $\theta_{\text{rx}}^{\max} \to 90^\circ$. Then, $\left|k_x^{\max}\right| \approx 2k$ and, according to (6.9),

$$\delta_x = \frac{\pi}{\left|k_x^{\max}\right|} \approx \frac{\lambda}{4}. \tag{6.14}$$

This is the well-known diffraction limit of imaging with far-zone data. More generally,

$$\delta_x \approx \frac{\lambda}{2(\sin\theta_{\text{tx}}^{\max} + \sin\theta_{\text{rx}}^{\max})}. \tag{6.15}$$

Here, $\theta_{\text{tx}}^{\max}$ and $\theta_{\text{rx}}^{\max}$ are determined by the size of the acquisition aperture, see (6.12) or by the antenna beamwidths, whichever is less. It is clear that wide-beamwidth antennas (e.g., omnidirectional antennas) are preferable as they provide wider viewing angles of the imaged object thereby improving the spatial resolution. Also, we recognize that larger

values of $\theta_{\text{tx}}^{\max}$ and $\theta_{\text{rx}}^{\max}$ imply longer signal paths in the planar acquisition considered here. In a lossy propagation medium, this means loss of information at larger angles, which would degrade the resolution performance additionally.

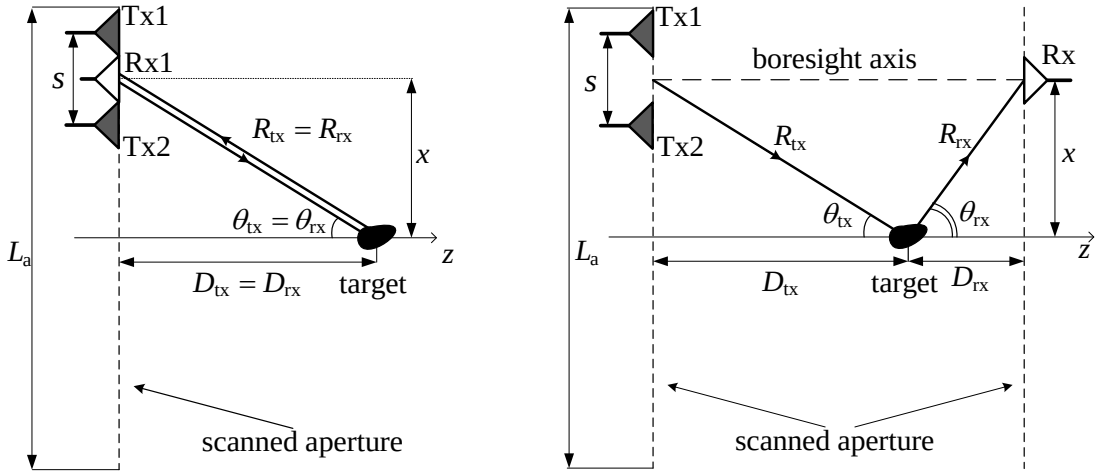

Figure 6.2 Illustration of the antenna and target positions in planar raster scanning in the case of differential illumination: (a) monostatic, (b) bi-static.

6.2.1.2 Double-Source Illumination

In the case of a double-source illumination, the scattered signal due to a point scatterer in the differential case is approximated as

$$S_{0,\text{d}}^{-}(x) \approx S_{\text{da}}^{-}(x) = \left(e^{-\text{i}kR_{\text{tx}1}} - e^{-\text{i}kR_{\text{tx}2}}\right)e^{-\text{i}kR_{\text{rx}}}, \tag{6.16}$$

whereas in the in-phase case, it is

$$S_{0,\text{d}}^{+}(x) \approx S_{\text{da}}^{+}(x) = \left(e^{-\text{i}kR_{\text{tx}1}} + e^{-\text{i}kR_{\text{tx}2}}\right)e^{-\text{i}kR_{\text{rx}}}. \tag{6.17}$$

Here, R_{tx1} and R_{tx2} are the distances from sources 1 and 2 to the scatterer, respectively (see Figure 6.2). If the angle defined by the vectors $\mathbf{R}_{\text{tx1}}$ and $\mathbf{R}_{\text{tx2}}$ (i.e., the angle supported by the double source when the vertex is at the scatterer's center) is sufficiently small, then

$$\begin{aligned} R_{\text{tx1}} &\approx R_{\text{tx}} + 0.5s \cdot \sin\theta_{\text{tx}}, \\ R_{\text{tx2}} &\approx R_{\text{tx}} - 0.5s \cdot \sin\theta_{\text{tx}}. \end{aligned} \tag{6.18}$$

This condition is fulfilled in the far zone of the double-source array or when θ_{tx} and θ_{rx} tend to 90°. Then, $S_{\text{da}}^{-}(x)$ and $S_{\text{da}}^{+}(x)$ can be written in terms of S_{a}, see (6.10), as

$$S_{\text{da}}^{-}(x) = S_{\text{a}}(x) \cdot 2\text{i}\sin\left(0.5ks\sin\theta_{\text{tx}}\right). \tag{6.19}$$

Analogously, from (6.17) we get

$$S_{\text{da}}^{+}(x) = S_{\text{a}}(x) \cdot 2\cos\left(0.5ks\sin\theta_{\text{tx}}\right). \tag{6.20}$$

The argument $0.5ks\sin\theta_{\text{tx}}$ can also be written as

$$\frac{ks}{2}\sin\theta_{\text{tx}} = \frac{ks}{2R_{\text{tx}}} \cdot x. \tag{6.21}$$

This result indicates an increase in the spectral content of $\tilde{S}_{\text{da}}^{-}$ and $\tilde{S}_{\text{da}}^{+}$ as compared to $\tilde{S}_{\text{a}}$ by $ks/(2R_{\text{tx}})$. This increase would be insignificant if $R_{\text{tx}} >> s$. However, in near-field imaging, where $R_{\text{tx}} \approx s$, the spectral width would double. Note that the highest spectral components in the system PSF arise when the receiver/transmitter pair is at the edge of

the acquisition aperture, in which case the approximations in (6.18) hold in the near zone as well.

To appreciate this effect in real (x) space, we can write explicitly the derivatives of the differential and the in-phase PSFs as

$$\frac{dS_{\mathrm{da}}^{-}}{dx} = -\mathrm{i}k(\sin\theta_{\mathrm{tx}} + \sin\theta_{\mathrm{rx}})S_{\mathrm{da}}^{-} + \mathrm{i}\frac{ks}{D_{\mathrm{tx}}}\cos\left(\frac{ks}{2}\sin\theta_{\mathrm{tx}}\right)\cdot\cos^3\theta_{\mathrm{tx}}\cdot S_{\mathrm{a}} \tag{6.22}$$

and

$$\frac{dS_{\mathrm{da}}^{+}}{dx} = -\mathrm{i}k(\sin\theta_{\mathrm{tx}} + \sin\theta_{\mathrm{rx}})S_{\mathrm{da}}^{+} - \frac{ks}{D_{\mathrm{tx}}}\sin\left(\frac{ks}{2}\sin\theta_{\mathrm{tx}}\right)\cdot\cos^3\theta_{\mathrm{tx}}\cdot S_{\mathrm{a}}\,. \tag{6.23}$$

In the right-hand sides of (6.22) and (6.23), the first terms indicate the presence of high spectral components due to signals at the aperture's edge such that $|k_x^{\max}| \approx k(\sin\theta_{\mathrm{tx}}^{\max} + \sin\theta_{\mathrm{rx}}^{\max})$. This is a result equivalent to the case of the single-source illumination considered above. On the other hand, when $\theta_{\mathrm{tx}}, \theta_{\mathrm{rx}} \to 0^{\circ}$, the response sensitivity with the single-source illumination is zero as per (6.11), i.e., the response is insensitive to variations in the cross-range position of the target. This is also the case with the in-phase double-source illumination, i.e., $dS_{\mathrm{da}}^{+}/dx \to 0$ for $x \to 0$. However, the signal sensitivity with the differential illumination remains nonzero:

$$\left.\frac{dS_{\mathrm{da}}^{-}}{dx}\right|_{\theta_{\mathrm{tx}},\theta_{\mathrm{rx}}\to 0} \approx \mathrm{i}\frac{ks}{D_{\mathrm{tx}}}\cdot S_{\mathrm{a}}(x=0)\,. \tag{6.24}$$

In summary, the cross-range resolution can be improved by at least a factor of 2 in near-field imaging by using the double-source illumination such that the element separation is comparable to the range distance. The improvement is due to the introduction of incident field patterns that vary spatially faster than the one obtained with a single source. The effect can be further enhanced by using arrays consisting of more than 2 elements. This finding is particularly important in the imaging of lossy objects often encountered in non-destructive testing and medical (tissue) imaging. In this case, near-field data acquisition is a necessity since the signals attenuate fast and must be captured close to the abnormalities that generate them. Moreover, the angles $\theta_{\text{tx}}^{\max}$ and $\theta_{\text{rx}}^{\max}$ are severely limited by the attenuation associated with longer signal paths. Thus, it is important to have high signal sensitivity to target positions centered on and around the aperture's axis, which is not the case with the single-source illumination. In this respect, an optimal choice is the differential (or the ANI) array configuration. The ANI configuration offers the added and very important advantage of eliminating the need to acquire the baseline (or reference) system response as this response is simply zero (or nearly so).

6.2.2 Range Resolution

It is well known that the range resolution limit with far-zone measurements is given by [23]:

$$\delta_z \approx \frac{v_{\text{RO}}}{2(f_{\max} - f_{\min})}, \tag{6.25}$$

where v_{RO} is the speed of light in the background medium.

It is clear that the range resolution depends primarily on the frequency bandwidth. Therefore, the double-source illumination is not expected to bring substantial improvement in this regard. This can also be understood by considering the signal sensitivity with respect to variations in the range position of a target. The double-source illumination introduces a rapidly-varying incident field in the lateral direction thus improving the cross-range resolution. However, it does not change significantly the field's behavior along range in comparison with the conventional illumination. We briefly note that the range resolution could be improved by introducing 3D illuminating arrays or multiple planes of acquisition along range. This problem's solution is not pursued here.

6.3 Background De-Embedding

Figure 6.3(a) shows a simple example of the conventional illumination scheme. Two antennas, aligned along each other's boresight, form a two-port network together with the imaged volume. Each antenna may operate as a transmitter (Tx) and as a receiver (Rx) thus allowing for the acquisition of two reflection and two transmission coefficients. This configuration can be expanded into an electronically-switched array or can be scanned mechanically. Often, both electronic switching and mechanical scanning are employed since the spatial sampling rate of electronically-switched arrays may not be sufficient.

In both transmission and reflection measurements, the single-source illumination scheme results in relatively strong received signals even when the scatterer-free background is measured. These signals are referred to as the *baseline* signals, which are

representative of the incident-field component in the scattering equations. The baseline signals are clearly significant with forward measurements, since in this scenario, the transmitter and at least one sensor are aligned along each other's boresight while operating without any obstruction. The baseline reflected signals may also be strong relative to the reflection from a weak scatterer since achieving a perfect impedance match of the antenna is difficult, especially in a wide frequency range.

In view of the above, it is clear that when an object under test (OUT) is examined, the acquired signal S_{OUT} contains two components: one due to the baseline signal, which can be interpreted as the incident-field signal component, and one due to the signal scattered from the OUT, which can be interpreted as the scattered-field component. We are interested in the scattered-field component S_{sc} as it carries information about the target.

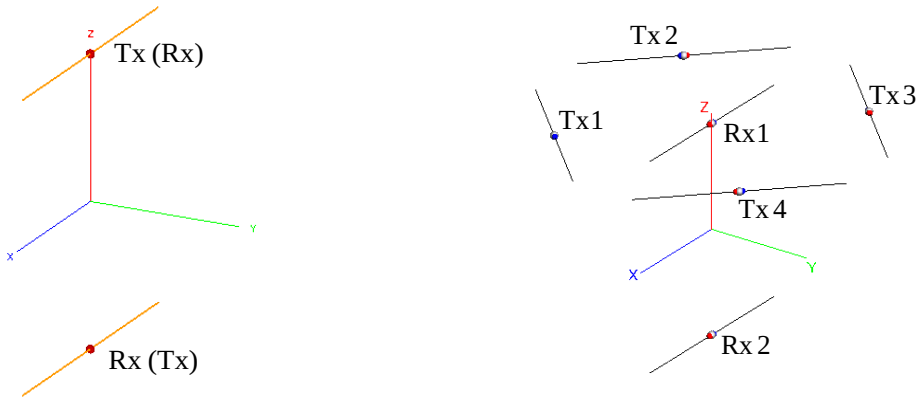

(a) (b)

Figure 6.3 (a) Conventional measurement setup consisting of two half-wavelength dipoles along with (b) a transmitting ANI arrangement of dipoles (Tx1 to Tx4) together with two receiving antennas (Rx1 and Rx2) centered on the ANI central axis.

The baseline signal S_{RO} is acquired with a measurement in the background medium, here referred to as the *reference object* (RO). The acquisition of S_{RO} is part of the system calibration and is, in principle, independent of any subsequent OUT measurements. Then, the baseline signal S_{RO} is subtracted from S_{OUT} to obtain an estimate of S_{sc}, $S_{\mathrm{sc}} = S_{\mathrm{OUT}} - S_{\mathrm{RO}}$. This simple approach to background de-embedding is based on the assumption that the mutual coupling between the acquisition hardware and the target can be neglected and the OUT signal is simply a superposition of the baseline and the scattered signals.

Two main problems ensue due to the need to estimate the baseline signal S_{RO}. First, the respective calibration measurements are needed—often performed before each OUT measurement. Second, the baseline signal contains systematic and stochastic noise and uncertainties at levels comparable to those contained in S_{OUT}. Provided the baseline measurement is performed under exactly the same circumstances as those of the OUT—a challenging requirement on its own—the systematic errors should cancel. Unfortunately, stochastic noise and uncertainties in the positioning do not cancel.

To address the above problems, here we propose a new axial-null illumination (ANI) scheme (see Figure 6.3(b)). The ANI can be viewed as the 2D extension of the differential illumination discussed above. It is inspired by the same illumination concept used in optical lithography for improving the spatial resolution [24][25]. An alternative term, "off-axis illumination" (OAI), is also used in the optical literature. In principle, ANI

can be used in planar, cylindrical and spherical scanners, although in this work we focus on its application with planar scanning.

Since ANI is a multi-source illumination, it has an enhanced cross-range resolution in near-field measurements as proved above. However, an additional advantage of such illumination is in reducing the noise and uncertainty in the data by decreasing significantly the strength of the baseline signals. Ideally, these signals should be zero due to the intrinsic antisymmetry of the illumination. In practice, they are suppressed down to the noise floor of the receiver or the measurement uncertainties. Most importantly, near-zero baseline signals allow to forego the calibration measurements in the background medium.

It should be noted that due to a null along the central axis, ANI may be viewed as somewhat similar to null steering antennas (NSA) used in the wireless communications industry [26][27]. GPS systems, for example, are vulnerable to electromagnetic jamming because of the wide angular coverage. By reconfiguring the radiation pattern, NSA can generate a null in a given direction where the interference source is located. However, steering of the radiation pattern null is not needed in microwave imaging. Also, ANI has only one fixed null along its central axis for the purpose of having near-zero baseline signals as well as the large gradient of the incident field, which makes it different from the NSA applications.

6.4 ANI: Setup and Design Requirements

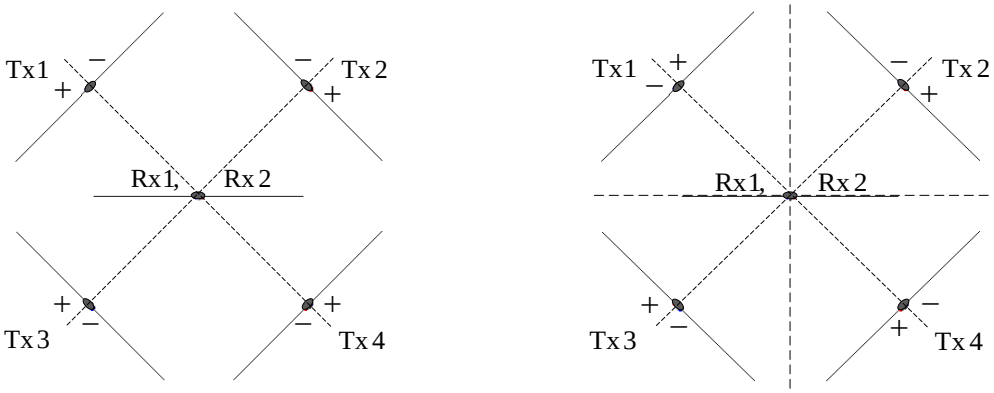

(a) (b)

Figure 6.4 Top view of the two cases of the ANI design with dipoles: (a) with 2 antisymmetry planes, and (b) with 4 antisymmetry planes. The planes of antisymmetry are shown with dash lines.

A simulation example of an ANI transmitting arrangement using FEKO [28] is illustrated in Figure 6.3(b). This particular configuration consists of 4 transmitting and 2 receiving dipoles. Both receiving antennas are centered on the axis of the ANI. The dipole Rx1 is used to acquire back-scattered signals whereas the antenna along the ANI axis but on the opposite side of the imaged volume (Rx2) acquires the forward-scattered signals.

The goal of ANI, as explained earlier, is to ensure zero baseline signals, i.e., zero field along the ANI's axis, in a background medium that is uniform or layered. Depending on the antenna elements, there are at least two planar arrangements that can achieve this goal. These are illustrated in Figure 6.4 where dipoles are used. These two arrangements have the same geometry, i.e., the dipoles' spacing and orientations are the same, but their phasing differs. The first arrangement (in Figure 6.4(a)) features 2 mutually orthogonal planes of antisymmetry intersecting at the ANI's center. The second one (shown in Figure 6.4(b)) has two pairs of such planes of antisymmetry.

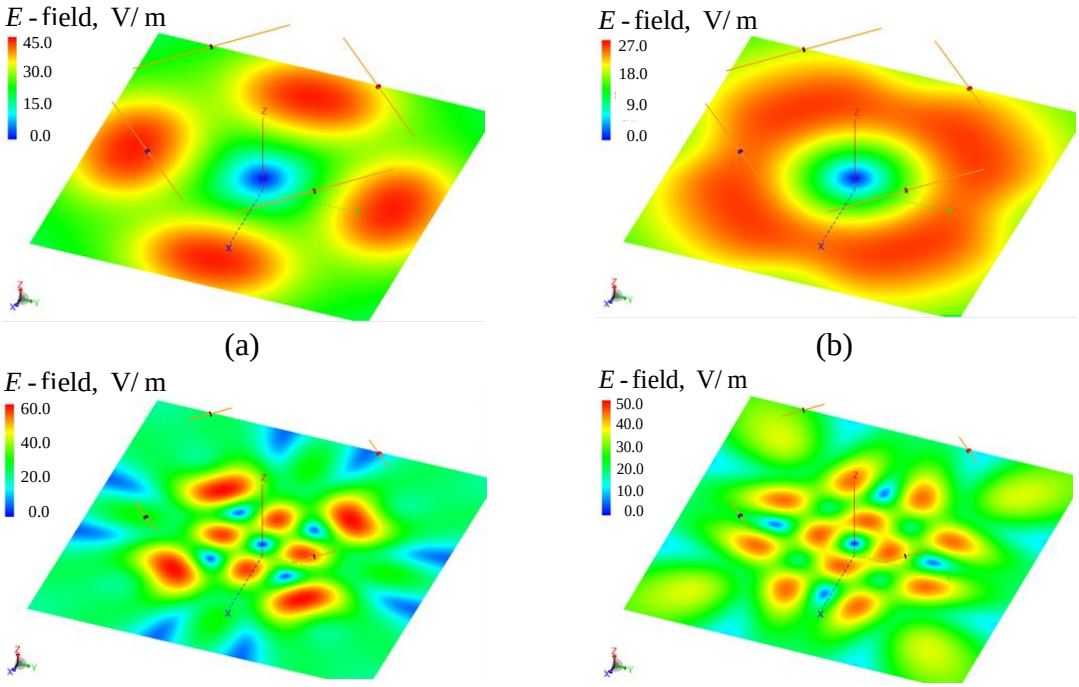

Figure 6.5 Screenshot from a FEKO simulation showing the *E*-field strength in a plane intersecting the RO (background medium) at a distance of 20 mm from the plane of the ANI in the case of the configuration in: (a) Fig. 5-a (2 antisymmetry planes) at 3 GHz; (b) Fig. 5-b (4 antisymmetry planes) at 3 GHz; (c) Fig. 5-a (2 antisymmetry planes) at 11 GHz; (d) Fig. 5-b (4 antisymmetry planes) at 11 GHz. The separation between the ANI elements is 70 mm.

The proposed illumination scheme may appear counter-intuitive as it is clear that if a target is located along the ANI's axis, it is not going to be detected—it is not illuminated, therefore, it does not scatter. However, ANI creates an illumination interference pattern (see Figure 6.5). While a null of this pattern lies at its center, maxima reside nearby. Depending on the separation between the ANI elements, the distance to the target and the wavelength, the field maxima can be anywhere between one and two times stronger than the boresight maximum created by a single element provided comparable power is fed to each of the ANI array elements. If the interference pattern changes sufficiently fast in

space, even a slight displacement of a target from the center disturbs the field antisymmetry and results in a non-zero received signal. This signal is a purely scattered signal, i.e., ideally, it does not have an incident-field component ($S_{RO} = 0$).

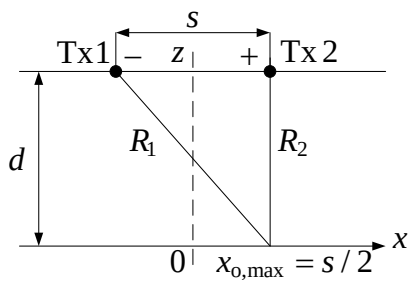

Figure 6.6 The differential illumination as a 2D ANI version.

The design of the ANI array depends on the choice of its antenna elements. With the antenna elements known, the design involves choosing the separation distance between them as well as determining their orientation, which is dependent mostly on the antenna polarization. The ANI array can be optimized for best sensitivity by requiring that: (i) the field along the central axis (the *z* axis in Figure 6.3) is zero; (ii) within the square area defined by the centers of the ANI elements, there are at least four maxima of the interference pattern. The latter requirement ensures that the strength of the scattered signal is no less than that in conventional illumination since the signal path from a maximum of the interference pattern to the receiving antenna is not much longer compared to the signal path along the boresight axis. It also ensures large field gradient at the ANI array axis leading to high sensitivity to the position of the scatterer.

We approach the problem of choosing the optimal separation of the ANI elements by considering the simpler 2D differential arrangement, which consists of two out-of-phase

transmitters. This arrangement is shown in Figure 6.6, where *d* is the focusing distance, i.e., the distance between the line of the transmitters (Tx1 and Tx2) and the line of the imaged points. The two lines are parallel. In Figure 6.6, x_o is the observation point, s is the separation between the two elements, R_i $(i = 1, 2)$ is the distance between the *i*-th transmitter and the observation point. To obtain an analytical estimate, the problem is further simplified by assuming point sources. The point sources approximation (also known as isotropic source approximation) is commonly exploited in far-field estimations and analyses of antenna arrays since the results can be easily augmented to represent realistic antennas via a simple multiplication with the antenna pattern. Therefore, the point-source simplification is valid as long as the focusing plane is not in the reactive near field of the antenna element.

For the case illustrated in Figure 6.6, the field at the observation point x_o can be written as the superposition

$$E_x^{\text{inc}}(x_o) \propto e^{-\mathrm{i}kR_1} - e^{-\mathrm{i}kR_2}, \tag{6.26}$$

where *k* is the wavenumber of the background medium. Note that when the background medium is lossy, it can be properly accounted for in the expression for *k*. A maximum of the interference pattern is required at $x_o \le s/2$ at the lowest frequency (or the largest wavelength $\lambda_{\max}$). The distances from Tx1 and Tx2 to $x_{o,\max} = s/2$ are

$$R_1 = \sqrt{d^2 + s^2} \text{ and } R_2 = d. \tag{6.27}$$

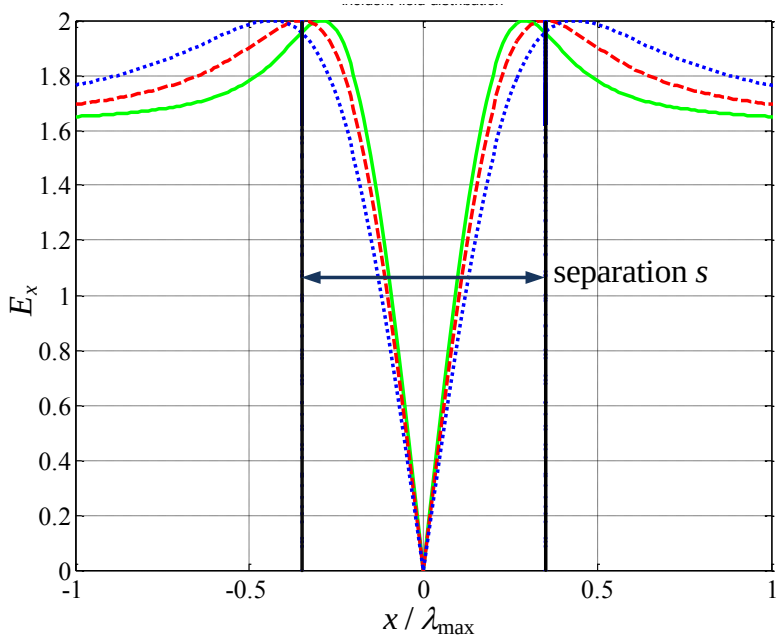

Figure 6.7 Magnitude distribution of the incident field for three different values of the distance d to the observation plane: d = 15 mm (solid), 24 mm (dash) and 35 mm (dot) in the case of differential illumination at 3 GHz. The separation s = 70 mm.

The constructive interference occurs when

$$kR_2 = kR_1 + \pi(2n+1),\ n = 0,1,\ldots, \tag{6.28}$$

where $n = 0$ corresponds to the first maximum. Therefore, with $n = 0$, the equation for a maximum at $x_{o,max} = s/2$ is

$$\sqrt{\bar{d}^2 + \bar{s}^2} - \bar{d} = 0.5, \tag{6.29}$$

where $\bar{d} = d/\lambda_{max}$, $\bar{s} = s/\lambda_{max}$. The relation between $\bar{s}$ and $\bar{d}$ can then be found as

$$\bar{d} = \bar{s}^2 - 0.25,\ \bar{s} > 0.5 \text{ or } s > \frac{\lambda_{max}}{2}. \tag{6.30}$$

The requirements for dense sampling and large gradient of the incident-field distribution demand as small separation $\bar{s}$ as possible. On the other hand, the separation is limited from below by the size of the ANI elements and the need to minimize mutual coupling. Thus, the requirement $s \geq \lambda_{\max}/2$ is usually met in practice. Conversely, if a specific focusing distance d is required (typically centered in the middle of the imaged volume), then s can be determined using (6.30). Note that the choice of $\bar{s}$ and $\bar{d}$ has implications for the spatial resolution as well. These were discussed in the previous section.

Figure 6.7 illustrates the field distribution at 3 GHz obtained analytically using (6.26). The longest wavelength (in air) is $\lambda_{\max} \approx 100$ mm. The separation is set at s = 70 mm. Three distributions are shown corresponding to d = 15 mm, 24 mm and 35 mm. According to (6.30), at $d_0 = 24$ mm, the field-strength peaks are aligned with the separation s. This is indeed the case as is evident from Figure 6.7. For $d < d_0$, the peaks shift inward within the interval defined by s, which is a desirable effect. For $d > d_0$ they move out of s, which is not desirable. In summary, for maximum sensitivity, the focusing distance d has to be kept smaller than or approximately equal to d_0, where d_0 is determined according to (6.30).

In the case of far-zone measurements, i.e., $\bar{d} > \bar{s}$ ($\bar{d} > 1, \bar{s} > 1$), it can be shown that the same requirement leads to $\bar{s}^2 \approx \bar{d}$. We note that this requirement ensures the maximum possible field gradient at the axis of ANI and therefore the maximum

sensitivity. However, even if the above conditions are not met, the benefits of a zero on-axis incident field remain.

6.5 Validation with Scattered-Power Mapping

6.5.1 Cross-Range Resolution Study

The investigation of the resolution limits for both the conventional and axial-null illuminations is carried out here with the BCCB SPM presented in Chapter 3. For that, we simulate the OUT consisting of 2 dielectric cubes of 5 mm^3 volume with the relative permittivity of $\varepsilon_{r,OUT} = 1.2$ (Figure 6.8). The RO is chosen to be air, while the CO has a small dielectric cube of 5 mm^3 volume with the relative permittivity of $\varepsilon_{r,sc} = 1.1$, placed in the center of the imaged plane. Note that the RO data have been used for reconstruction only in the conventional illumination case.

The ANI array has a separation s = 70 mm. The distance between the transmitting and receiving planes is 50 mm. The focusing distance from the transmitters to the middle of imaged objects is 15 mm. In both illumination schemes, the transmitters and the receivers are half-wavelength dipoles (the physical length is adjusted at each frequency) at frequencies from 5 GHz to 9 GHz.

To investigate the cross-range resolution, three cases are considered: dielectric cubes at edge-to-edge distances of $\Delta y = 20$ mm, 10 mm and 5 mm (Figure 6.8).

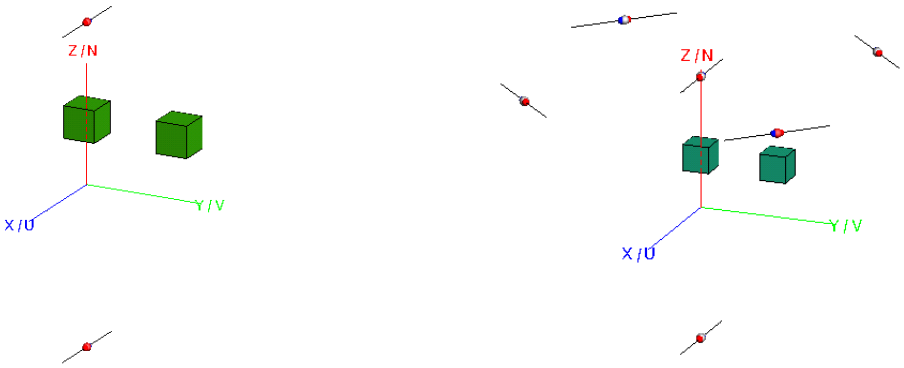

(a) (b)

Figure 6.8 Illumination setup in FEKO for the imaging of 2 dielectric cubes in the cross-range (*xy*) plane: (a) conventional case and (b) ANI case.

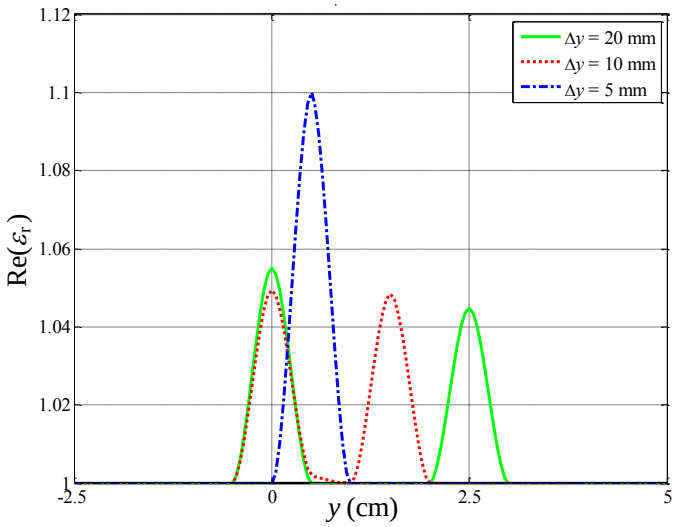

Figure 6.9 Real part of the reconstructed relative permittivity of the two cubes along the *y* axis at 8 GHz for the conventional illumination case. The edge-to-edge distances between the cubes are: 20 mm (solid), 10 mm (dot) and 5 mm (dash-dot).

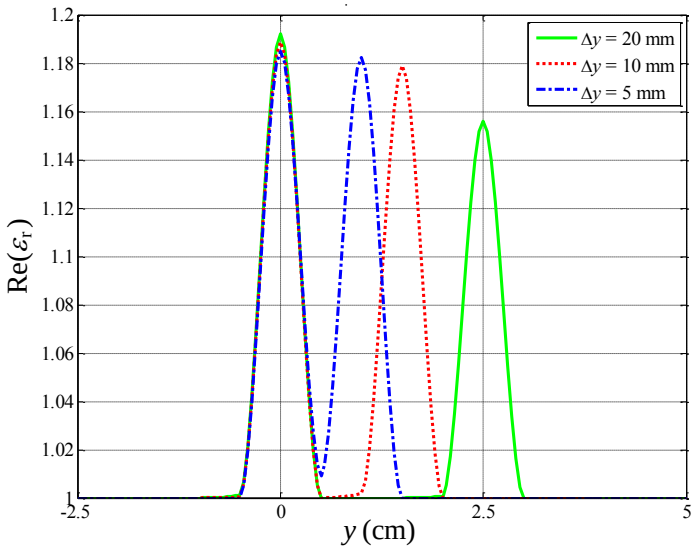

Figure 6.10 Real part of the reconstructed relative permittivity of the two cubes along the *y* axis at 7 GHz for the ANI case. The edge-to-edge distances between the cubes are: 20 mm (solid), 10 mm (dot) and 5 mm (dash-dot).

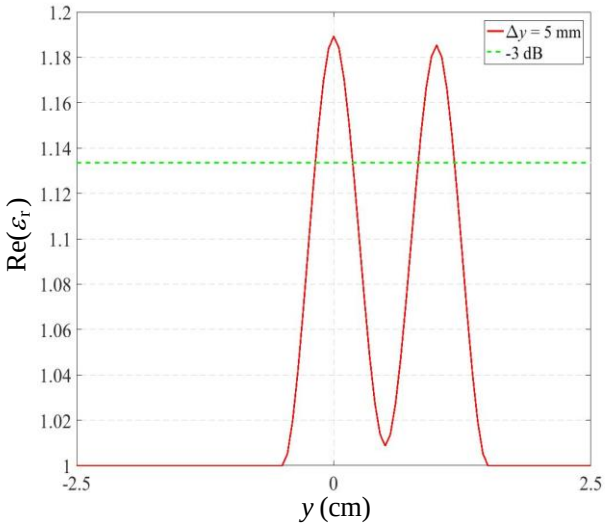

Figure 6.11 Real part of the reconstructed relative permittivity of the two cubes along the *y* axis at 5.7 GHz for the ANI case (red solid) and -3dB level (green dashed). The edge-to-edge distance between the cubes is 5 mm (center-to-center distance is 10 mm).

Figure 6.9 shows a cut of the reconstructed relative permittivity of two dielectric cubes along the *y* axis in the case of conventional illumination. It is evident that at 8 GHz the

two objects merge into one when the edge-to-edge distance is 5 mm. Thus, the estimated resolution limit is about $\lambda/4$, where $\lambda = 37.5$mm is the free-space wavelength at 8 GHz. This result is in agreement with the estimated cross-range resolution in the conventional illumination case given in (6.14).

In the case of ANI, the reconstructed relative permittivities of the imaged cubes at 7 GHz are shown in Figure 6.10. In all three cases, it is possible to differentiate the two objects. Figure 6.11 shows that in the case of ANI and when $\Delta y = 5$ mm, the two objects can still be distinguished well at 5.7 GHz. Therefore, the estimated cross-range resolution is approximately $\lambda/10$, where $\lambda = 52.6$ mm is the free-space wavelength at 5.7 GHz. This result is in agreement with the theory presented above where it has been shown that the cross-range resolution for the ANI case can be improved by at least a factor of 2 in comparison with the conventional illumination.

6.5.2 Experimental Example 1

The experimental setup consists of five identical open-end waveguides at the top and one at the bottom as shown in Figure 6.12. The four waveguides at the corners of the top array realize an ANI, whereas the central waveguide serves as a conventional single-source illumination element. The waveguide at the bottom serves as a receiver only. We acquire only forward-scattered signals with both illumination schemes. The ANI elements are connected to separate vector network analyzer ports and the respective transmission coefficients to the receiving open waveguide at the bottom plane are acquired. These transmission coefficients are added to produce a total response that emulates

simultaneous illumination. Note that the four elements of the ANI array are oriented so that this total response is near zero in the baseline measurement; in practice, it varies from −60 dB to −53 dB across the X-band range.

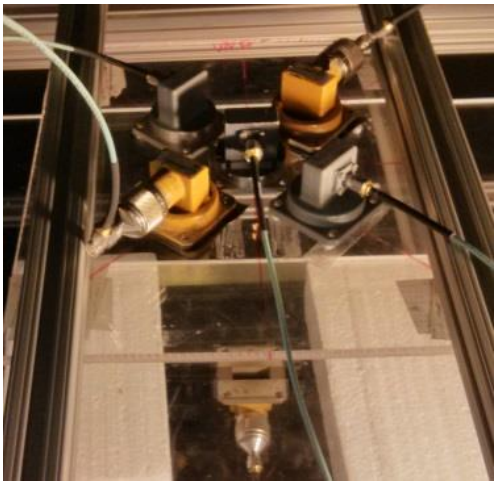

Figure 6.12 ANI array consisting of four transmitting X-band open-end waveguides (at the top plane) plus a conventional single-source illumination element at the center. Receiver is located at the bottom.

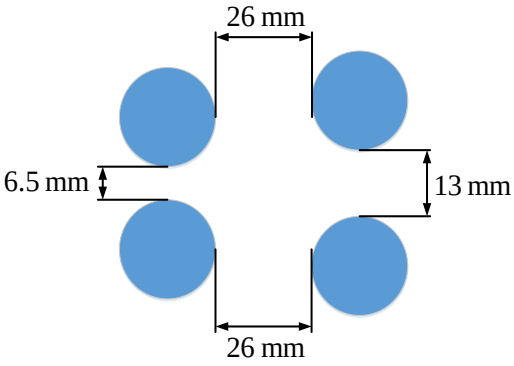

Figure 6.13 Schematic view of four identical dielectric cylinders serving as OUT. The separation distances are chosen approximately equal to $\lambda_0/4$ (6.5 mm), $\lambda_0/2$ (13 mm) and λ_0 (26 mm) at the central frequency of the X-band.

The ANI array has a separation of 95 mm and the focusing distance equals 50 mm as calculated from (6.30) for the 8 GHz frequency. The presented illumination structure in Figure 6.12 is part of the planar-raster acquisition system. The imaged area is 20 cm by 20 cm. The sampling step in both lateral directions is 5 mm.

The imaged dielectric cylinders of 1 cm height and 1 cm diameter have the relative permittivity of $\varepsilon_{r,OUT} \approx 50$ (Figure 6.13). The CO used consists of air with a dielectric cylinder identical to those in OUT, placed in the center of the imaged plane.

The reconstructed OUT using the BCCB SPM with the conventional illumination and ANI is shown in Figure 6.14. Notice that the RO data have not been used in neither of the reconstructions. It is observed that the quality of the reconstructed images in the ANI case is much better since the detrimental effect of the baseline signal is minimized by ANI. On the contrary, Figure 6.14(a) demonstrates the conventional-case scenario where the reconstructed image is obtained from the OUT data being a superposition of the baseline and scattered signals. We emphasize that the same reconstruction method is used in generating both images in Figure 6.14. The improvement observed in Figure 6.14(b) is entirely due to the proposed axial-null illumination scheme.

As a final observation, we note that the dynamic range of the reconstructed images is larger in the ANI case compared to that in the conventional illumination case (Figure 6.14).

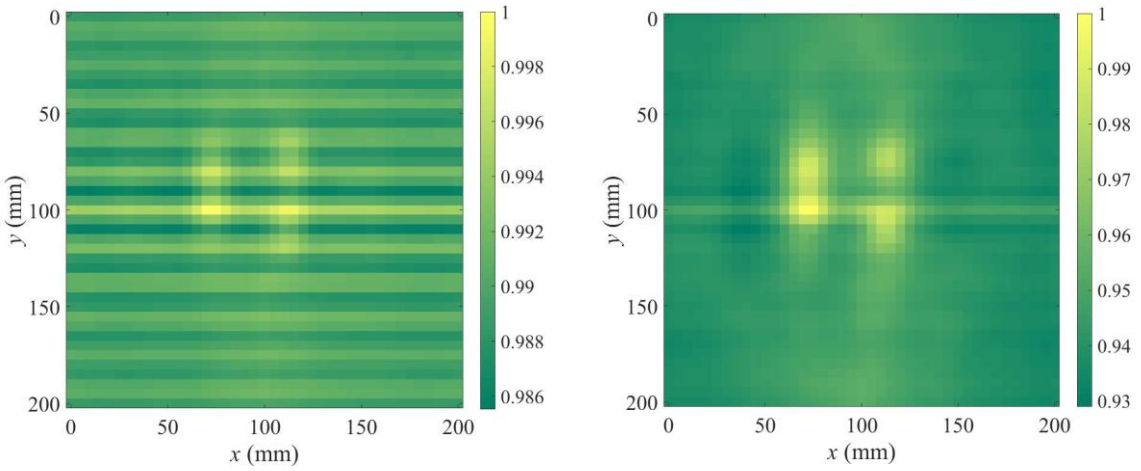

(a) (b)

Figure 6.14 Qualitative reconstruction results of four dielectric cylinders for the frequency sweep from 8 GHz to 12 GHz: (a) with conventional illumination and (b) with ANI. Transmission coefficients only are processed in this example. The results are normalized to 1.

6.5.3 Experimental Example 2

For the second example, we attempt to image objects behind drywall with ANI and with conventional illumination. Photos of the OUT and some of its components are shown in Figure 6.15. The OUT consists of a piece of drywall of size 47 cm by 36 cm by 1.3 cm, a dry-wood stud of size 47 cm by 8.8 cm by 3.7 cm and a plastic water pipe of 1.6 cm diameter together with an insulated three-wire electric cable. Since the dielectric permittivity of the drywall is relatively small ($\varepsilon_r \approx 2.2$, $\tan\delta \approx 0.01$ as per [29]), we use the same experimental setup consisting of X-band air-filled waveguides as in the previous experiment (see Figure 6.12). However, this time we are interested in the reflection measurements only since such scenarios admit only single-side access. Thus, the receiver at the bottom has been removed. In the case of ANI, the central element of the top array

transmits with the respective four transmission coefficients acquired. We use a 4-port test set allowing for a multi-port acquisition. It has been observed that this 4-port test set carries a considerable amount of attenuation, on the order of 5 dB to 10 dB depending on frequency. In order to ensure that the measurements with the ANI setup are reasonable, we include amplification to counteract the loss of power.

The CO is chosen to be a metallic cylinder attached to the bottom of the drywall and placed at the center of the imaged plane. The cylinder is 1 cm in height and 1 cm in diameter.

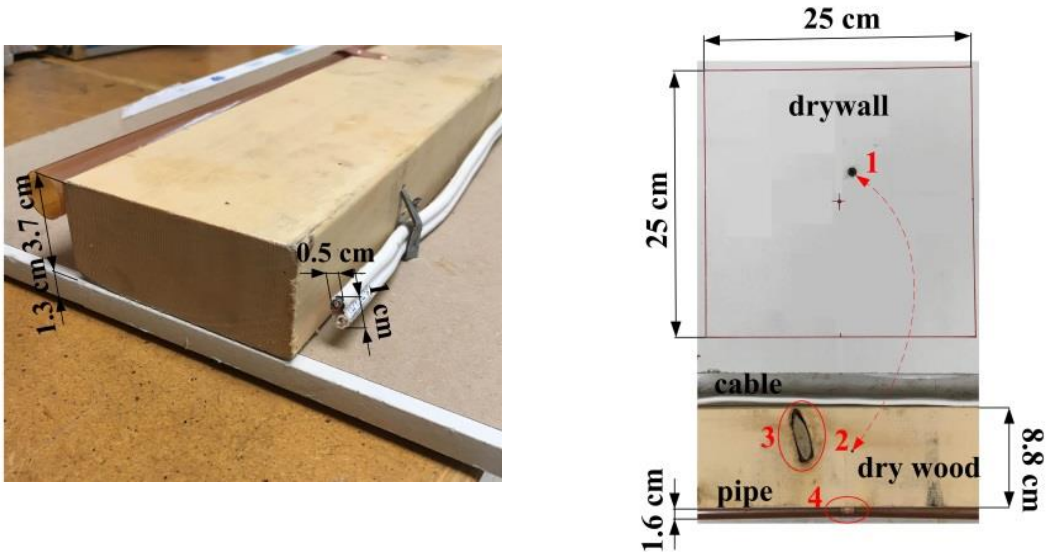

(a) (b)

Figure 6.15 The OUT consisting of drywall of size 47 cm by 36 cm by 1.3 cm, a piece of dry-wood stud of size 47 cm by 8.8 cm by 3.7 cm, a water pipe of 1.6 cm in diameter attached to the left side of the stud, and a three-wire electric cable attached to the right side of the stud: (a) the isometric view of the whole OUT upside down and (b) the top view of the disassembled OUT (part to be imaged is shown only). The imaged area is shown with a red square. The correspondence between the screw 1 and its hole 2 in the dry wood is shown with the red dashed arrow. The wood knot is shown as object 3 whereas the metallic brace attaching the pipe to dry wood is shown as object 4.

In the conventional illumination case, only the reflection coefficient at the central element of the array is acquired (Figure 6.12). Therefore, the 4-port test set is not used in this case. Also, since it is a reflection measurement, an amplifier cannot be used. Ultimately, the output power is –2 dBm in the conventional illumination case whereas the output power in the ANI case is 14 dBm.

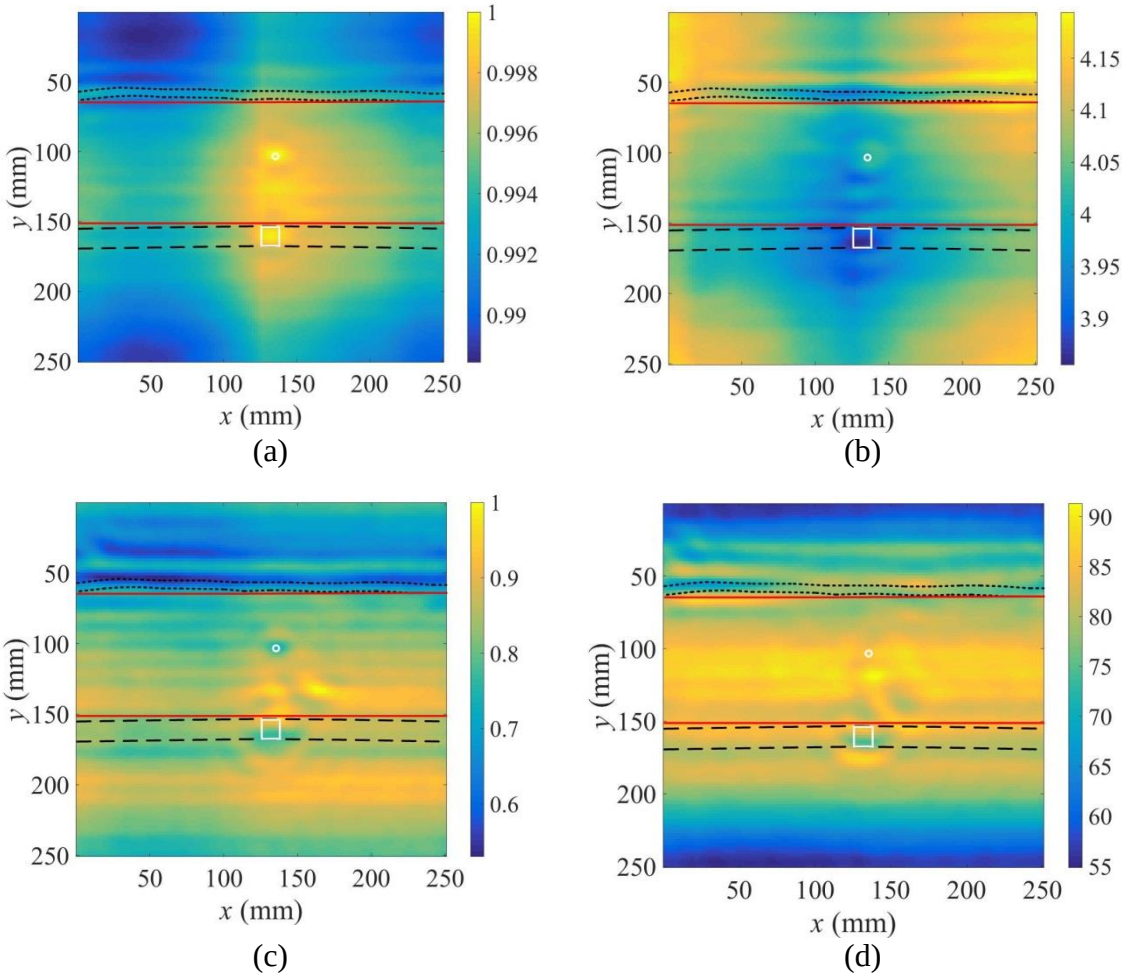

Figure 6.16 Qualitative reconstruction results for the second experiment: with conventional illumination (a) normalized magnitude and (b) phase in degrees, and with ANI (c) normalized magnitude and (d) phase in degrees. The frequency sweep is from 8 GHz to 12 GHz. The contour lines of the cable are dot black, the contour lines of the dry wood are solid red, the contour lines of the pipe are dashed black, and the contour lines of metallic objects are solid white (a circle and a square).

The ANI array has a separation of 95 mm and the focusing distance is 5 mm which is in agreement with (6.30) for the 8 GHz frequency. The planar-raster acquisition system is used with the imaged area being 25 cm by 25 cm. The sampling step in both lateral directions is 2 mm.

Using the BCCB SPM, the imaged OUT in the conventional illumination case and in the ANI case is shown in Figure 6.16. We observe a more detailed reconstruction with all of the objects being distinguishable in the case of ANI. In the conventional illumination case, there is a significant artifact along the *x* and *y* axes. Also, the water pipe cannot be seen.

As in the previous example, the dynamic range of the images in the ANI case exceeds that in the conventional illumination case. However, this time such a significant difference in the dynamic ranges is explained by using an amplifier for the measurements with ANI.

References

[1] J. Nanzer. *Microwave and Millimeter-wave Remote Sensing for Security Applications*. Norwood, MA: Artech House, 2012.

[2] M. G. Amin. *Through-the-Wall Radar Imaging*. Boca Raton, FL: CRC Press, 2011.

[3] R. Zoughi. *Microwave Non-destructive Testing and Evaluation*. Dordrecht, The Netherlands: Kluwer Academic, 2000.

[4] A. V. Vorst, A. Rosen, and Y. Kotsuka. *RF/Microwave Interaction with Biological Tissues*. Hoboken, NJ: Wiley, 2006.

[5] N. K. Nikolova, "Microwave biomedical imaging," *Wiley Encyclopedia of Electrical and Electronics Engineering*, pp. 1–22. (published online Apr. 25, 2014).

[6] M. Pastorino. *Microwave Imaging*. Hoboken, NJ: Wiley, 2010.

[7] S. Caorsi, G. L. Gragnani, and M. Pastorino, "An electromagnetic approach using a multi-illumination technique," *IEEE Trans. Biomed. Eng*., vol. 41, no. 4, pp. 406–409, Apr. 1994.

[8] C.-H. Tseng and T.-H. Chu, "Improvement of quasi-monostatic frequency-swept microwave imaging of conducting objects using illumination diversity technique," *IEEE Trans. Antennas Propag*., vol. 53, no. 1, pp. 305–312, Jan. 2005.

[9] L. Helaoui, J. Bel Hadj Tahar, and F. Choubani, "Multi-source illumination approach for buried objects exploration," *2008 2nd Int. Conf. Dig. Soc*., pp. 146–149, Sainte Luce, Feb. 2008.

[10] Y. Zhao, W. Shao, and G. Wang, "UWB microwave imaging for early breast cancer detection: effect of two synthetic antenna array configurations," *2004 IEEE Int. Conf. Syst., Man and Cybern*., vol. 5, pp. 4468–4473, Oct. 2004.

[11] P. M. Meaney, M. W. Fanning, D. Li, S. P. Poplack, and K. D. Paulsen, "A clinical prototype for active microwave imaging of the breast," *IEEE Trans. Microw. Theory Techn*., vol. 48, no. 11, pp. 1841–1853, Nov. 2000.

[12] A. Zakaria, C. Gilmore, and J. LoVetri, "Finite-element contrast source inversion method for microwave imaging," *Inverse Problems*, vol. 26, no. 11, 115010, 21 pp., Sep. 2010.

[13] P. Mojabi, M. Ostadrahimi, L. Shafai, and J. LoVetri, "Microwave tomography techniques and algorithms: a review," *Antenna Technol. Applied Electromagn. (ANTEM)*, pp. 1–4, Toulouse, France, Jun. 2012.

[14] S. Y. Semenov, R. H. Svenson, A. E. Bulyshev, A. E. Souvorov, A. G. Nazarov, Y. E. Sizov, V. G. Posukh, A. V. Pavlovsky, P. N. Repin, and G. P. Tatsis, "Spatial resolution of microwave tomography for detection of myocardial ischemia and infarction – experimental study on two-dimensional models," *IEEE Trans. Microw. Theory Techn.*, vol. 48, no. 4, pp. 538–544, Apr. 2000.

[15] C. Gilmore, P. Mojabi, A. Zakaria, S. Pistorius, and J. LoVetri, "On super-resolution with an experimental microwave tomography system," *IEEE Antennas Wireless Propag. Lett.*, vol. 9, pp. 393–396, May 2010.

[16] M. Klemm, I. J. Craddock, J. A. Leendertz, A. Preece, and R. Benjamin, "Radar-based breast cancer detection using a hemispherical antenna array – experimental results," *IEEE Trans. Antennas Propag.*, vol. 57, no. 6, pp. 1692–1704, Jun. 2009.

[17] M. Donelli, I. Craddock, D. Gibbins, and M. Sarafianou, "A three-dimensional time domain microwave imaging method for breast cancer detection based on an evolutionary algorithm," *Progress In Electromagnetics Research*, vol. 18, pp. 179–195, 2011.

[18] M. Klemm, J. A. Leendertz, D. Gibbins, I. J. Craddock, A. Preece, and R. Benjamin, "Microwave radar-based breast cancer detection: imaging in inhomogeneous breast phantoms," *IEEE Antennas Wireless Propag. Lett*., vol. 8, pp. 1349–1352, Nov. 2009.

[19] P. Rocca, M. Donelli, G. L. Gragnani, and A. Massa, "Iterative multi-resolution retrieval of non-measurable equivalent currents for the imaging of dielectric objects," *Inverse Problems*, vol. 25, no. 5, 15 pp., Feb. 2009.

[20] F. Viani, M. Donelli, P. Rocca, R. Azaro, and A. Massa, "A multi-resolution three-dimensional approach based on SVM for breast cancer detection," *24th Int. Review Progr. Applied Computat. Electromagn*., pp. 479–482, ACES, Niagara Falls, Canada, 2008.

[21] M. Donelli, D. Franceschini, A. Massa, M. Pastorino, and A. Zanetti, "Multi-resolution iterative inversion of real inhomogeneous targets," *Inverse Problems*, vol. 21, no. 6, pp. S51–S63, Nov. 2005.

[22] M. Ravan, R. K. Amineh, and N. K. Nikolova, "Two-dimensional near-field microwave holography," *Inverse Problems*, vol. 26, no. 5, 21 pp., May 2010.

[23] D. M. Sheen, D. L. McMakin, and T. E. Hall, "Three-dimensional millimeter-wave imaging for concealed weapon detection," *IEEE Trans. Microw. Theory Techn*., vol. 49, no. 9, pp. 1581–1592, Sep. 2001.

[24] M. Fritze, B. M. Tyrell, D. K. Astolfi, R. D. Lambert, D. W. Yost, A. R. Forte, S. G. Cann, and B. D. Wheeler, "Subwavelength optical lithography with phase-shift photomasks," *Lincoln Laboratory Journal*, vol. 14, no. 2, pp. 237–250, 2003.

[25] A. K.-K. Wong. *Resolution Enhancement Techniques in Optical Lithography*. Bellingham, WA: SPIE, 2001.

[26] C. Deng, Y. Li, Z. Zhang, and Z. Feng, "A hemispherical 3-D null steering antenna for circular polarization," *IEEE Antennas Wireless Propag. Lett.*, vol. 14, pp. 803–806, 2015.

[27] C. Sun, A. Hirata, T. Ohira, and N. C. Karmakar, "Fast beamforming of electronically steerable parasitic array radiator antennas: theory and experiment," *IEEE Trans. Antennas Propag.*, vol. 52, no. 7, pp. 1819–1832, Jul. 2004.

[28] FEKO Suite 7.0.1 for Altair. EM Software & Systems – S. A. (Pty) Ltd., USA (www.feko.info).

[29] R. Wilson, "Propagation losses through common building materials: 2.4 GHz vs. 5 GHz," E10589 Magis Networks, Inc., 27 pp., Aug. 2002.

Chapter 7

Conclusions and Future Work

In this thesis, the results of an ongoing development of a near-field microwave imaging system are presented. The thesis mainly focuses on the image reconstruction theory and more specifically, on the linear inversion methods. Another important aspect, namely, the preprocessing of the measured data with a novel de-noising algorithm, has been investigated.

In terms of the hardware part, a calibration strategy with metallic scattering probe is developed for near-field quantitative linear inversion methods. The axial-null illumination scheme for near-field microwave imaging is also proposed. Rigorous proof of the improvement in cross-range resolution in the multi-illumination case compared to the conventional single-source illumination is presented as well.

Here, the conclusions related to the proposed developments are further discussed and summarized. Recommendations for future research are also provided.

7.1 Scattered-Power Mapping (SPM) as a Linear-Inversion Module

The BCCB SPM and the convolution-based SPM have been proposed as direct-inversion methods for fast quantitative imaging. Two key advantages of these methods

compared to the work reported in [1][2] are the computational speed and the reduced area of the calibration scan. In addition, the BCCB SPM and the convolution-based SPM are more general since they accommodate a forward model of scattering cast either as a linearized Born model or as a Rytov model. It is known that compared to the Born approximation, the Rytov approximation is not limited by the target's size. Therefore, the Rytov-based SPM is more likely to succeed in the near-field imaging of large tissue samples.

It has been shown that the BCCB SPM and the convolution-based SPM produce similar images. However, the convolution-based SPM proves to be superior in terms of computational time: it provides quantitative images practically instantaneously. That is why convolution-based SPM is considered to be our first choice for solving weak-scattering problems.

Both the BCCB SPM and the convolution-based SPM are limited by the linearizing approximations of the forward model of scattering. Consequently, they are incapable of accounting for mutual coupling and multiple scattering. Such effects dominate the scattering in complex heterogeneous objects such as living tissue, luggage items, structural components in civil engineering, etc. Often, from a qualitative point of view, the SPM images are valuable even with strongly heterogeneous scattering objects that feature high contrast. Yet, these results lack quantitative accuracy. Future work aims at incorporating the quantitative SPM method inside nonlinear reconstruction schemes such as the Born iterative method [3] or the distorted Born iterative method [4] (equivalent to the Newton-Kantorovich [5] and Levenberg-Marquardt [6] methods). The distinguishing

feature of these algorithms is that they employ the Born series to successively improve the accuracy of the contrast estimate and that of the total field. Since they utilize linear reconstruction modules inside the iterative loop, they can greatly benefit from the quantitative real-time performance of either the BCCB SPM or the convolution-based SPM.

7.2 Target-Independent Calibration for Quantitative Linear-Inversion Methods

The calibration strategy previously used by SPM imposes limitations. In this thesis, it is referred to as the calibration with a dielectric scattering probe. For accurate quantitative results, the relative permittivity of a voxel in the object under test must be close to that of the scattering probe in the calibration object. Since the permittivity of the scattering probe is fixed, the quantitative reconstruction of objects with widely varying permittivity distribution (e.g., living tissue) is not likely to be accurate. That is why, a new calibration strategy employing a metallic scattering probe has been proposed here. It allows achieving target-independent quantitative accuracy of the reconstruction.

The calibration with a metallic scattering probe is also beneficial in nonlinear reconstruction methods where Green's function and the incident field distribution are subjected separately to iterative updates. It has been shown that these two quantities comprising the kernel, $\mathbf{E}_{\mathrm{RO},i}^{(m)}$ and $\mathbf{E}_{\mathrm{RO},j}^{(m)}$ (see (2.13)), can be mapped individually by *S*-parameter measurements of the wire probe. Note that, with a wire scatterer, only one field component may be resolved at a time. This is in fact desirable when full polarimetric

information is required. In contrast, the sphere, for example, is incapable of discriminating the waves based on their polarization.

On the other hand, the calibration with a metallic scattering probe has a disadvantage. The scaling factor enabling quantitative imaging is very sensitive to the parameters of the wire scatterer (its length and radius) as well as the relative permittivity of the background (see (2.29) or (2.30)). At the same time, the only theoretical guideline for choosing the wire's parameters is to ensure the wire is electrically short and very thin. That is why, using a controlled object embedded within the OUT volume can serve as a practical alternative to the calculation of the scaling factor. In this way, information about the wire scatterer is no longer needed: the scaling factor can be determined from the known permittivity distribution of the controlled object. The measurement of such controlled object can be done as a part of the measurement of the inspected object, or as a separate step during the system calibration. Both scenarios have to be thoroughly investigated in order to determine the optimal one to be used in the future.

7.3 De-noising Raw Data before Reconstruction

An algorithm has been proposed for the de-noising of *S*-parameter data used in microwave imaging. The complex *S*-parameter frequency-sweep data are collected through scans over an acquisition surface and the algorithm separates efficiently the resultant 2D responses (one frequency at a time) into a signal and a noise component. The separation is performed with an iterative procedure similar to the empirical mode decomposition. The signal component estimates the noise-free data whereas the

remaining data content estimates the noise and uncertainty in the measurement. The algorithm performance has been verified with measured data.

It has been shown that the proposed algorithm has several benefits in microwave imaging. First, it can supress noise and uncertainties in the data used as an input to the reconstruction algorithms. Second, the condition number of the BCCB system matrix containing the CO power maps improves significantly after applying the de-noising algorithm to the respective raw data. In some cases, reconstruction with the SPM failed without de-noising the data. Due to all these reasons, it is strongly recommended to use the de-noising algorithm as a preprocessing step within linear and nonlinear reconstruction methods.

7.4 Optimal Illumination Schemes for Near-Field Microwave Imaging

Rigorous proof of the improvement in the cross-range resolution in the multi-illumination case compared to the conventional single-source illumination has been developed. Based on this, an optimized axial-null illumination (ANI) scheme for near-field microwave imaging is proposed. Due to the intrinsic antisymmetry of such illumination, the baseline signals are supressed down to the noise level of the measurement system. Therefore, the proposed axial-null illumination simplifies the calibration process by eliminating the need to acquire the responses in the scatterer-free background. On the other hand, the sharp gradient of the field magnitude within the separation distance provides high sensitivity to the position of a scatterer.

The discussed improvements are expected to occur not only for the SPM imaging method used here for validation purposes, but also for any other imaging technique that exploits wave-like physical fields. This is because the improvement results from the geometrical configuration of emitters and sensors as well as the fast-changing incident field distribution, and not the specifics of the reconstruction method.

The initial experimental results obtained with four X-band open-end waveguides show that is it extremely difficult to implement the ANI array for ultra-wideband microwave systems. For example, a relatively small phase unbalance as well as a misalignment of the array elements results in a shift of the radiation null from the center of the ANI array [7]. However, we note that in a frequency range from 3.3 GHz to 8 GHz, ANI can be implemented with a single antenna introduced in [8]. Also, it should be emphasized that in principle, the field distribution with zero field at the center can be achieved at the step of processing the data coming from multiple sensors. In this way, there is no need for a complicated hardware while all the benefits of ANI can still be preserved. As the next step, we plan to undertake an extensive experimental study of the so-called synthetic ANI.

References

[1] S. Tu, J. J. McCombe, D. S. Shumakov, and N. K. Nikolova, “Fast quantitative microwave imaging with resolvent kernel extracted from measurements,” *Inverse Problems*, vol. 31, no. 4, 33 pp., Mar. 2015.

[2] D. S. Shumakov, S. Tu, and N. K. Nikolova, "Fast quantitative microwave imaging based on measured point spread functions and inversion in real space," *IEEE AP-S/URSI Int. Symp. Antennas Propag.*, pp. 687–688, Jul. 2015.

[3] Y. M. Wang and W. C. Chew, "An iterative solution of the two-dimensional electromagnetic inverse scattering problem," *Int. J. Imaging Syst. Technol.*, vol. 1, no. 1, pp. 100–108, 1989.

[4] W. C. Chew and Y. M. Wang, "Reconstruction of two-dimensional permittivity distribution using the distorted Born iterative method," *IEEE Trans. Med. Imag.*, vol. 9, no. 2, pp. 218–225, Jun. 1990.

[5] N. Joachimowicz, C. Pichot, and J.-P. Hugonin, "Inverse scattering: an iterative numerical method for electromagnetic imaging," *IEEE Trans. Antennas Propag.*, vol. 39, no. 12, pp. 1742–1752, Dec. 1991.

[6] A. Franchois and C. Pichot, "Microwave imaging – complex permittivity reconstruction with a Levenberg-Marquardt method," *IEEE Trans. Antennas Propag.*, vol. 45, no. 2, pp. 203–215, Feb. 1997.

[7] J. J. McCombe, "The impact of phase and position errors on the field pattern of the fully anti-symmetric waveguide illumination," CEM-R-74, McMaster University, Canada, Nov. 2015.

[8] C. H. J. Jenks, "Dielectric pyramid antenna for GPR applications," *10th European Conference on Antennas and Propagation (EuCAP)*, Davos, Switzerland, pp. 1–3, Apr. 2016.

BIBLIOGRAPHY

Abubakar, A., and T. M. Habashy, "A Green function formulation of the extended Born approximation for three-dimensional electromagnetic modelling," *Wave Motion* 41, no. 3 (Mar. 2005): 211–227.

Abubakar, A., P. M. van den Berg, and J. J. Mallorqui, "Imaging of biomedical data using a multiplicative regularized contrast source inversion method," *IEEE Trans. Microw. Theory Techn.* 50, no. 7 (Jul. 2002): 1761–1771.

Agilent 85070E Dielectric Probe Kit. USA: Keysight Technologies Inc., 2013.

Akinci, M. N., et al., "Qualitative microwave imaging with scattering parameters measurements," *IEEE Trans. Microw. Theory Techn.* 63, no. 9 (Sep. 2015): 2730–2740.

Amin, M. G. *Through-the-Wall Radar Imaging.* Boca Raton, FL: CRC Press, 2011.

Amineh, R. K., A. Khalatpour, H. Xu, Y. Baskharoun, and N. K. Nikolova, "Three-dimensional near-field microwave holography for tissue imaging," *Int. J. Biomed. Imaging* 2012, no. Article ID 291494 (2012): 1–11.

Amineh, R. K., J. J. McCombe, A. Khalatpour, and N. K. Nikolova, "Microwave holography using point-spread functions measured with calibration objects," *IEEE Trans. Instrum. Meas* 64, no. 2 (Feb. 2015): 403–417.

Amineh, R. K., J. J. McCombe, and N. K. Nikolova, "Microwave holographic imaging using the antenna phaseless radiation pattern," *IEEE Antennas and Wireless Propag. Lett.* 11 (2012): 1529–1532.

Amineh, R. K., M. Ravan, A. Trehan, and N. K. Nikolova, "Near-field microwave imaging based on aperture raster scanning with TEM horn antennas," *IEEE Trans. Antennas Propag.* 59, no. 3 (Mar. 2011): 928–940.

Amineh, R. K., M. Ravan, J. McCombe, and N. K. Nikolova, "Three-dimensional microwave holographic imaging employing forward-scattered waves only," *Int. J. Antennas Propag.* 2013 (2013): 1–15.

Banham, M. R., and A. K. Katsaggelos, "Digital image restoration," *IEEE Sign. Proc. Mag.* 14, no. 2 (Mar. 1997): 24–41.

Beaverstone, A. S., D. S. Shumakov, and N. K. Nikolova, "Frequency-domain integral equations of scattering for complex scalar responses," *IEEE Trans. Microw. Theory Techn.* 65, no. 4 (Apr. 2017): 1120–1132.

Bertero, M., M. Miyakawa, P. Boccacci, F. Conte, K. Orikasa, and M. Furutani, "Image restoration in chirp-pulse microwave CT (CP-MCT)," *Trans. Biomed. Eng.* 47, no. 5 (May 2000): 690–699.

Biggs, D. S. C. *Accelerated Iterative Blind Deconvolution.* Auckland, New Zealand: PhD Thesis. University of Auckland, Dec. 1998.

Bolomey, J. C., A. Izadnegahdar, L. Jofre, C. Pichot, G. Peronnet, and M. Solaimani, "Microwave diffraction tomography for biomedical applications," *Trans. Microw. Theory Techn.* 30, no. 11 (Nov. 1982): 1998–2000.

Born, M., and E. Wolf. *Principles of Optics.* New York: Pergamon, 1980.

Boudraa, A. -O., and J. -C. Cexus, "EMD-based signal filtering," *IEEE Trans. Instrum. Meas.* 56, no. 6 (Dec. 2007): 2196–2202.

Boudraa, A. O., J. C. Cexus, and Z. Saidi, "EMD-based signal noise reduction," *Int. J. Signal Process.* 1, no. 1 (Jan. 2005): 33–37.

Box, G. E. P., W. G. Hunter, and J. S. Hunter. *Statistics for experimenters: an introduction to design, data analysis, and model building.* USA: John Wiley & Sons, 1978.

Bushberg, J. T., J. A. Seibert, E. M. Leidholdt Jr., and J. M. Boone. *The Essential Physics of Medical Imaging.* Philadelphia, USA: Lippincott Williams & Wilkins, 2012.

Caorsi, S., G. L. Gragnani, and M. Pastorino, "An electromagnetic approach using a multi-illumination technique," *IEEE Trans. Biomed. Eng.* 41, no. 4 (Apr. 1994): 406–409.

Chen, B., and J. J. Stamnes, "Validity of diffraction tomography based on the first Born and the first Rytov approximations," *Applied Optics* 37, no. 14 (May 1998): 2996–3006.

Chew, W. C. *Waves and Fields in Inhomogeneous Media.* Piscataway, NJ: IEEE Press, 1995.

Chew, W. C., and Y. M. Wang, "Reconstruction of two-dimensional permittivity distribution using the distorted Born iterative method," *IEEE Trans. Med. Imag.* 9, no. 2 (Jun. 1990): 218–225.

Cui, T. J., W. C. Chew, A. A. Aydiner, and S. Chen, "Inverse scattering of two-dimensional dielectric objects buried in lossy earth using the distorted Born iterative method," *IEEE Trans. Geosci. Remote Sens.* 39, no. 2 (Feb. 2001): 339–346.

CVX Research Inc., "Using MOSEK with CVX," 2012. http://web.cvxr.com/cvx/beta/doc/mosek.html#mosek (accessed May 14, 2017).

Daniels, D. J. *EM Detection of Concealed Targets.* Hoboken, NJ: Wiley-IEEE Press, 2009.

Davis, P. J. "Circulant matrices." In *Circulant Matrices*, 66–189. New York: Wiley, 1979.

Deng, C., Y. Li, Z. Zhang, and Z. Feng, "A hemispherical 3-D null steering antenna for circular polarization," *IEEE Antennas Wireless Propag. Lett.* 14 (2015): 803–806.

Devaney, A. J. *Mathematical Foundations of Imaging, Tomography and Wavefield Inversion.* Cambridge, UK: Cambridge University Press, 2012.

Diener, L. "Microwave near-field imaging with open-ended waveguide – Comparison with other techniques of non-destructive testing," *Res. Nondestruct. Eval.* 7, no. 2 (1995): 137–152.

Dietrich, O., J. G. Raya, S. B. Reeder, M. F. Reiser, and S. O. Schoenberg, "Measurement of signal-to-noise ratios in MR images: influence of multichannel coils. Parallel imaging and reconstruction filters," *J. Magn. Reson. Imaging* 26, no. 2 (Aug. 2007.): 375–385.

Donelli, M., D. Franceschini, A. Massa, M. Pastorino, and A. Zanetti, "Multi-resolution iterative inversion of real inhomogeneous targets," *Inverse Problems* 21, no. 6 (Nov. 2005): S51–S63.

Donelli, M., G. Franceschini, A. Martini, and A. Massa, "An integrated multiscaling strategy based on a particle swarm algorithm for inverse scattering problems," *IEEE Trans. Geosci. Remote Sens.* 44, no. 2 (Feb. 2006): 298–312.

Donelli, M., I. Craddock, D. Gibbins, and M. Sarafianou, "A three-dimensional time domain microwave imaging method for breast cancer detection based on an

evolutionary algorithm," *Progress In Electromagnetics Research* 18 (2011): 179–195.

Donoho, D. L. "De-noising by soft-thresholding," *IEEE Trans. Inf. Theory* 41, no. 3 (May 1995): 613–627.

Elsdon, M., D. Smith, M. Leach, and S. J. Foti, "Experimental investigation of breast tumor imaging using indirect microwave holography," *Microw. Opt. Technol. Lett* 48 (Jan. 2006): 480–482.

Elshinawy, M. Y., J. Zeng, S. -C. Lo, and M. F. Chouikha, "Breast cancer detection in mammogram with AM-FM modeling and Gabor filtering," *7th Int. Conf. on Signal Processing (ICSP).* Sep. 2004.

EM Software & Systems – S. A. (Pty) Ltd. "FEKO Suite 7.0.1 for Altair." USA, 2016.

Emerson & Cuming Microwave Products Inc. Randolph, MA, USA: Unit of Laird Technologies, 2012.

Estatico, C., M. Pastorino, and A. Randazzo, "An inexact-Newton method for short-range microwave imaging within the second-order Born approximation," *IEEE Trans. Geosci. Remote Sens.* 43, no. 11 (Nov. 2005): 2593–2605.

Eyraud, C., A. Litman, A. Herique, and W. Kofman, "Microwave imaging from experimental data within a Bayesian framework with realistic random noise," *Inverse Problems* 25, no. 2 (Feb. 2009): 1–16.

Eyraud, C., A. Litman, A. Herique, and W. Kofman, "Microwave imaging from experimental data within a Bayesian framework with realistic random noise," *Inverse Problems* 25, no. 2 (Feb. 2009): 1–16.

Eyraud, C., J. -M. Geffrin, A. Litman, P. Sabouroux, and H. Giovannini, "Drift correction for scattering measurements," *Applied Physics Lett.* 89, no. 24 (Dec. 2006): 1–3.

Farhat, N. "Microwave holography and coherent tomography," *Medical Applications of Microwave Imaging*, 1986: 66–81.

Farooq, M., and A. Salhi, "Improving the solvability of ill-conditioned systems of linear equations by reducing the condition number of their matrices," *J. Korean Math. Soc.* 48, no. 5 (2011): 939–952.

Fear, E. C., X. Li, S. C. Hagness, and M. A. Stuchly, "Confocal microwave imaging for breast cancer detection: localization of tumors in three dimensions," *IEEE Trans. Biomed. Eng.* 49, no. 8 (Aug. 2002): 812–822.

Feleppa, E. J. "Holography and medicine," *IEEE Trans. Biomed. Eng.* BME-19, no. 3 (May 1972): 194–205.

Firbank, M. J., A. Coulthard, R. M. Harrison, and E. D. Williams, "A comparison of two methods for measuring the signal-to-noise ratio on MR images," *Phys. Med. Biol.* 44, no. 12 (Dec. 1999): N261–N264.

Firbank, M. J., R. M. Harrison, E. D. Williams, and A. Coulthard, "Quality assurance for MRI: practical experience," *British J. Radiol.* 73, no. 868 (2000): 376–383.

Franchois, A., and C. Pichot, "Microwave imaging – complex permittivity reconstruction with a Levenberg-Marquardt method," *IEEE Trans. Antennas Propag.* 45, no. 2 (Feb. 1997): 203–215.

Fritze, M., et al., "Subwavelength optical lithography with phase-shift photomasks," *Lincoln Laboratory Journal* 14, no. 2 (2003): 237–250.

Gilmore, C., P. Mojabi, A. Zakaria, S. Pistorius, and J. LoVetri, "On super-resolution with an experimental microwave tomography system," *IEEE Antennas Wireless Propag. Lett.* 9 (May 2010): 393–396.

Giraudeau, P., and S. Akoka, "Sensitivity and lineshape improvement in ultrafast 2D NMR by optimized apodization in the spatially encoded dimension," *Magnet. Reson. Chem.* 49, no. 6 (Jun. 2011): 307–313.

Gonzalez, R. C., and R. E. Woods. *Digital Image Processing.* Upper Saddle River, New Jersey: Prentice Hall, 2008.

Goodman, J. W. *Introduction to Fourier Optics.* New York, NY: McGraw-Hill, 1996.

Habashy, T. M., R. W. Groom, and B. Spies, "Beyond the Born and Rytov approximations: a nonlinear approach to electromagnetic scattering," *J. Geophys. Res.* 98, no. B2 (Feb. 1993): 1759–1775.

Harada, H., D. J. N. Wall, T. Takenaka, and M. Tanaka, "Conjugate gradient method applied to inverse scattering problem," *IEEE Trans. Antennas Propag.* 43, no. 8 (Aug. 1995): 784–792.

Harris, F. J. "On the use of windows for harmonic analysis with the discrete Fourier transform," *Proc. IEEE* 66 (Jan. 1978): 51–83.

Haynes, M., and M. Moghaddam, "Multipole and S-parameter antenna and propagation model," *IEEE Trans. Antennas Propag.* 59, no. 1 (Jan. 2011): 225–235.

Haynes, M., and M. Moghaddam, "Vector Green's function for S-parameter measurements of the electromagnetic volume integral equation," *IEEE Trans. Antennas Propag.* 60, no. 3 (Mar. 2012): 1400–1413.

Helaoui, L., J. Bel Hadj Tahar, and F. Choubani, "Multi-source illumination approach for buried objects exploration," *2nd Int. Conf. Dig. Soc.* Sainte Luce, Feb. 2008.

Huang, N. E., and et al., "The empirical mode decomposition and the Hilbert spectrum for nonlinear and non-staionary time series analysis," *Proc. R. Soc. Lond. A, Math. Phys. Sci.* 454, no. 1971 (Mar. 1998): 903–995.

Jenks, C. H. J. "Dielectric pyramid antenna for GPR applications," *10th European Conference on Antennas and Propagation (EuCAP).* Davos, Switzerland, Apr. 2016. 1–3.

Joachimowicz, N., C. Pichot, and J. -P. Hugonin, "Inverse scattering: an iterative numerical method for electromagnetic imaging," *IEEE Trans. Antennas Propag.* 39, no. 12 (Dec. 1991): 1742–1752.

Kaufman, L., D. M. Kramer, L. E. Crooks, and D. A. Ortendahl, "Measuring signal-to-noise ratios in MR imaging," *Radiology* 173, no. 1 (Oct. 1989): 265–267.

Keller, J. B. "Accuracy and validity of the Born and Rytov approximations," *J. Opt. Soc. Am.* 59, no. 8 (1969): 1003–1004.

Khare, K. *Fourier Optics and Computational Imaging.* Chichester, U.K.: John Wiley & Sons, 2016.

Klemm, M., I. J. Craddock, J. A. Leendertz, A. Preece, and R. Benjamin, "Radar-based breast cancer detection using a hemispherical antenna array – experimental results," *IEEE Trans. Antennas Propag.* 57, no. 6 (Jun. 2009): 1692–1704.

Klemm, M., J. A. Leendertz, D. Gibbins, I. J. Craddock, A. Preece, and R. Benjamin, "Microwave radar-based breast cancer detection: imaging in inhomogeneous breast phantoms," *IEEE Antennas Wireless Propag. Lett.* 8 (Nov. 2009): 1349–1352.

Kosmas, P., and C. M. Rappaport, "Time reversal with the FDTD method for microwave breast cancer detection," *IEEE Trans. Microw. Theory Techn.* 53, no. 7 (Jul. 2005): 2317–2323.

Lehmann, T. M., C. Gonner, and K. Spitzer, "Survey: interpolation methods in medical image processing," *IEEE Trans. Med. Imaging* 18, no. 11 (Nov. 1999): 1049–1075.

Lim, H. B., N. T. T. Nhung, E. P. Li, and N. D. Thang, "Confocal microwave imaging for breast cancer detection: delay-multiply-and-sum image reconstruction algorithm," *IEEE Trans. Biomed. Eng.* 55, no. 6 (Jun. 2008): 1697–1704.

Lin, J. C. "Frequency optimization for microwave imaging of biological tissues," *Proc. IEEE* 73, no. 2 (Feb. 1985): 374–375.

Liu, C., and H. Wechsler, "Gabor feature based classification using the enhanced fisher linear discriminant model for face recognition," *IEEE Trans. Image Proc.* 11, no. 4 (Apr. 2002): 467–476.

Liu, L., A. Trehan, and N. K. Nikolova, "Near-field detection at microwave frequencies based on self-adjoint response sensitivity analysis," *Inverse Problems* 26, no. 10 (Aug. 2010): 1–28.

MATLAB R2016a. Natick, MA, USA: The MathWorks Inc., 2016.

McCombe, J. J. *The impact of phase and position errors on the field pattern of the fully anti-symmetric waveguide illumination.* CEM-R-74, Hamilton, Canada: McMaster University, Nov. 2015.

McCombe, J. J., and N. K. Nikolova, "SNR assessment of microwave imaging systems," *IEEE AP-S/URSI Int. Symp. Ant. Propag.* Jul. 2014.

Meaney, P. M., M. W. Fanning, D. Li, S. P. Poplack, and K. D. Paulsen, "A clinical prototype for active microwave imaging of the breast," *IEEE Trans. Microw. Theory Techn.* 48, no. 11 (Nov. 2000): 1841–1853.

Meshgini, S., A. Aghagolzadeh, and H. Seyedarabi, "Face recognition using Gabor-based direct linear discriminant analysis and support vector machine," *Comput. Electr. Eng.* 39, no. 3 (Apr. 2013): 727–745.

Mojabi, P., M. Ostadrahimi, L. Shafai, and J. LoVetri, "Microwave tomography techniques and algorithms: a review," *Antenna Technology and Applied Electromagnetics (ANTEM).* Toulouse, France, Jun. 2012.

Mudanyali, O., and et al., "A microwave tomographic approach for nondestructive testing of dielectric coated metallic surfaces," *IEEE Geosci. Rem. Sens. Lett.* 5, no. 2 (Apr. 2008): 180–184.

Nanzer, J. *Microwave and Millimeter-wave Remote Sensing for Security Applications.* Norwood, MA: Artech House, 2012.

Nieto-Vesperinas, M. *Scattering and Diffraction in Physical Optics.* New York: John Wiley, 1991.

Nikolova, N. K. *Introduction to Microwave Imaging.* Cambridge University Press, 2017.

Nikolova, N. K. "Microwave biomedical imaging," In *Wiley Encyclopedia of Electrical and Electronics Engineering*, 1–22. 2014.

—. "The basics of microwave imaging in Principles of RF and Microwave Imaging Technology: From Radar to MRI," *Int. Microw. Symp.* San Francisco, May 2016.

Ostadrahimi, M., et al., "Analysis of incident field modeling and incident/scattered field calibration techniques in microwave tomography," *IEEE Antennas and Wireless Propag. Lett.* 10 (Sep. 2011): 900–903.

O'Sullivan, F., Y. Pawitan, and D. Haynor, "Reducing negativity artifacts in emission tomography: post-processing filtered backprojection solutions," *IEEE Trans. Med. Imag.* 12, no. 4 (Dec. 1993): 653–663.

Paoloni, F. J. "Implementation of microwave diffraction tomography for measurement of dielectric constant distribution," *EE Proceedings H – Microwaves, Antennas and Propagation* 134 (Feb. 1987): 25–29.

Pastorino, M. *Microwave Imaging.* Hoboken, NJ: Wiley, 2010.

Pastorino, M. "Stochastic optimization methods applied to microwave imaging: a review," *IEEE Trans. Antennas Propag.* 55, no. 3 (Mar. 2007): 538–548.

Pattichis, M. S., and A. C. Bovik, "Analyzing image structure by multidimensional frequency modulation," *IEEE Trans. Pattern Anal. Mach. Intell.* 29, no. 5 (May 2007): 753–766.

Pozar, D. M. "Microwave network analysis." In *Microwave Engineering*, 204–205. Hoboken, NJ: Wiley, 1998.

Proakis, J. G., and D. G. Manolakis. *Digital Signal Processing: Principles, Algorithms, and Applications.* Englewood Cliffs, NJ: Prentice-Hall, 1996.

Ravan, M., R. K. Amineh, and N. K. Nikolova, "Two-dimensional near-field microwave holography," *Inverse Problems* 26, no. 5 (Apr. 2010): 1–21.

Redivo-Zaglia, M., and G. Rodriguez, "SMT: a MATLAB toolbox for structured matrices," *Numer. Algor.* 59, no. 4 (Apr. 2012): 639–659.

Remis, R. F., and P. M. van den Berg, "On the equivalence of the Newton-Kantorovich and distorted Born methods," *Inverse Problems* 16, no. 1 (Feb. 2000): 1–4.

Rocca, P., M. Benedetti, M. Donelli, D. Franceschini, and A. Massa, "Evolutionary optimization as applied to inverse scattering problems," *Inverse Problems* 25, no. 12 (Nov. 2009): 1–41.

Rocca, P., M. Donelli, G. L. Gragnani, and A. Massa, "Iterative multi-resolution retrieval of non-measurable equivalent currents for the imaging of dielectric objects," *Inverse Problems* 25, no. 5 (Feb. 2009): 1–15.

Rosen, A., M. A. Stuchly, and A. V. Vorst, "Applications of RF/microwaves in medicine," *IEEE Trans. Microw. Theory Techn.* 50, no. 3 (Mar. 2002): 963–974.

Russ, J. C. *The Image Processing Handbook.* CRC Press, 2006.

Sancer, M. I., and A. D. Varvatsis, "A comparison of the Born and Rytov methods," *Proc. IEEE* 58, no. 1 (Jan. 1970): 140–141.

Savelyev, T. G., and A. G. Yarovoy, "Fast imaging by 3-D deconvolution in short-range UWB radar for concealed weapon detection," *9th Eur. Radar Conf. (EuRAD).* Amsterdam, The Netherlands, Oct./Nov. 2012.

Schatzberg, A., and A. J. Devaney, "Super-resolution in diffraction tomography," *Inverse Problems* 8, no. 1 (1992): 149–164.

Semenov, S. Y., and et al., "Spatial resolution of microwave tomography for detection of myocardial ischemia and infarction – experimental study on two-dimensional models," *IEEE Trans. Microw. Theory Techn.* 48, no. 4 (Apr. 2000): 538–544.

Sheen, D. M., D. L. McMakin, and T. E. Hall, "Near-field three-dimensional radar imaging techniques and applications," *Applied Optics* 49, no. 19 (July 2010): E83–E93.

Sheen, D. M., D. L. McMakin, and T. E. Hall, "Three-dimensional millimeter-wave imaging for concealed weapon detection," *IEEE Trans. Microw. Theory Techn.* 49, no. 9 (Sep. 2001): 1581–1592.

Shumakov, D. S. *Comparison of multi-frequency PSF normalization strategies.* CEM-R-76, Hamilton, Canada: McMaster University, Jul. 2016.

Shumakov, D. S., A. S. Beaverstone, and N. K. Nikolova, "De-noising algorithm for enhancing microwave imaging," *IET J. Eng.* Mar. 2017 (Mar. 2017): 1–5.

Shumakov, D. S., A. S. Beaverstone, and N. K. Nikolova, "Optimal illumination schemes for near-field microwave imaging," *Progress In Electromagnetics Research* 157 (2016): 93–110.

Shumakov, D. S., and N. K. Nikolova, "Fast quantitative microwave imaging with scattered-power maps," *IEEE Trans. Microw. Theory Techn.* Early Access (May 2017): 1–11.

Shumakov, D. S., D. Tajik, A. S. Beaverstone, and N. K. Nikolova, "Real-time quantitative reconstruction methods in microwave imaging," In *The World of Applied Electromagnetics*. Springer, 2017: 415–442.

Shumakov, D. S., S. Tu, and N. K. Nikolova, "Fast quantitative microwave imaging based on measured point spread functions and inversion in real space," *IEEE AP-S/URSI Int. Symp. Antennas Propag.* Vancouver, Canada, Jul. 2015.

Sibson, R. "A brief description of natural neighbor interpolation." In *Interpolating Multivariate Data*, 21–36. New York: John Wiley & Sons, 1981.

Slaney, M., A. C. Kak, and L. E. Larsen, "Limitations of imaging with first-order diffraction tomography," *IEEE Trans. Microw. Theory Techn.* 32, no. 8 (Aug. 1984): 860–874.

Smith, G. S. *An Introduction to Classical Electromagnetic Radiation.* Cambridge, U.K.: Cambridge Univ. Press, 1997.

Song, X., et al., "Automated region detection based on the contrast-to-noise ratio in near-infrared tomography," *Applied Optics* 43, no. 5 (Feb. 2004): 1053–1062.

Stathaki, T. *Image Fusion: Algorithms and Applications.* Academic Press, 2008.

Sun, C., A. Hirata, T. Ohira, and N. C. Karmakar, "Fast beamforming of electronically steerable parasitic array radiator antennas: theory and experiment," *IEEE Trans. Antennas Propag.* 52, no. 7 (Jul. 2004): 1819–1832.

Taconic CER-10 RF & Microwave Laminate, "High DK Material," USA, 2010.

Tajik, D., J. Thompson, A. S. Beaverstone, and N. K. Nikolova, "Real-time quantitative reconstruction based on microwave holography," *IEEE AP-S/URSI Int. Symp. on Antennas Propag.* Fajardo, Puerto Rico, June 2016.

Tapiovaara, M., and R. Wagner, "SNR and noise measurements for medical imaging: I. A practical approach based on statistical decision theory," *Physics in Medicine and Biology* 38, no. 1 (1993): 71.

Tijhuis, A. G., K. Belkebir, A. C. Litman, and B. P. de Hon, "Multiple-frequency distorted-wave Born approach to 2D inverse profiling," *Inverse Problems* 17, no. 6 (Nov. 2001): 1635–1644.

Torres-Verdin, C., and T. M. Habashy, "Rapid 2.5-dimensional forward modeling and inversion via a new nonlinear scattering approximation," *Radio Science* 29, no. 4 (Jul.-Aug. 1994): 1051–1079.

Traficante, D. D., and G. A. Nemeth, "A new and improved apodization function for resolution enhancement in NMR spectroscopy," *J. Magn. Reson.* 71, no. 2 (Feb. 1987): 237–245.

Tseng, C. -H., and T. -H. Chu, "Improvement of quasi-monostatic frequency-swept microwave imaging of conducting objects using illumination diversity technique," *IEEE Trans. Antennas Propag.* 53, no. 1 (Jan. 2005): pp. 305–312.

Tu, S., J. J. McCombe, D. S. Shumakov, and N. K. Nikolova, "Fast quantitative microwave imaging with resolvent kernel extracted from measurements," *Inverse Problems* 31, no. 4 (Mar. 2015): 1–33.

van Kempen, G. M. P., H. T. M. van der Voort, J. G. J. Bauman, and K. C. Strasters, "Comparing maximum likelihood estimation and constrained Tikhonov-Miller restoration," *IEEE Eng. Med. Biol. Mag.* 15, no. 1 (Jan/Feb 1996): 76–83.

Viani, F., M. Donelli, P. Rocca, R. Azaro, and A. Massa, "A multi-resolution three-dimensional approach based on SVM for breast cancer detection," *24th Int. Review Progr. Applied Computat. Electromagn.* Niagara Falls, Canada, 2008.

Vogel, C. R. "Image deblurring." In *Computational Methods for Inverse Problems*, 64–76. Philadelphia, PA: SIAM, 2002.

Vorst, A. V., A. Rosen, and Y. Kotsuka. *RF/Microwave Interaction with Biological Tissues.* Hoboken, NJ: Wiley, 2006.

Wagner, R. F., and D. G. Brown, "Unified SNR analysis of medical imaging systems," *Physics in Medicine and Biology* 30, no. 6 (1985): 489–518.

Wagner, R. F., M. F. Insana, and D. G. Brown, "Statistical properties of radio-frequency and envelope-detected signals with applications to medical ultrasound," *JOSA A* 4, no. 5 (May 1987): 910–922.

Wang, L., R. Simpkin, and A. Al-Jumaily, "Holographic microwave imaging for medical applications," *J. Biomed. Sci. Eng.* 6 (Aug. 2013): 823–833.

Wang, Y. M., and W. C. Chew, "An iterative solution of the two-dimensional electromagnetic inverse scattering problem," *Int. J. Imaging Syst. Technol.* 1, no. 1 (1989): 100–108.

Weisstein, E. W. "Apodization Function From MathWorld–A Wolfram Web." n.d. http://mathworld.wolfram.com/ApodizationFunction.html (accessed April 02, 2017).

Wilson, R. *Propagation losses through common building materials: 2.4 GHz vs. 5 GHz.* USA: E10589 Magis Networks, Inc., Aug. 2002.

Wong, A. K.-K. *Resolution Enhancement Techniques in Optical Lithography*. Bellingham, WA: SPIE, 2001.

Yano, F., and S. Nomura, "Deconvolution of scanning electron microscopy images," *Scanning* 15, no. 1 (1993): 19–24.

Zakaria, A., C. Gilmore, and J. LoVetri, "Finite-element contrast source inversion method for microwave imaging," *Inverse Problems* 26, no. 11 (Sep. 2010): 1–21.

Zhang, Y., S. Tu, R. K. Amineh, and N. K. Nikolova, "Microwave sensitivity-based imaging with data acquired on cylindrical surfaces: resolution and robustness to noise," *Inverse Problems* 28, no. 11 (Oct. 2012): 1–15.

Zhang, Y., S. Tu, R. K. Amineh, and N. K. Nikolova, "Resolution and robustness to noise of the sensitivity-based method for microwave imaging with data acquired on cylindrical surfaces," *Inverse Problems* 28, no. 11 (Oct. 2012): 1–15.

Zhao, Y., W. Shao, and G. Wang, "UWB microwave imaging for early breast cancer detection: effect of two synthetic antenna array configurations," *2004 IEEE Int. Conf. Syst., Man and Cybern.* vol. 5, pp. 4468–4473, Oct. 2004.

Zhdanov, M. S., and E. Tartaras, "Three-dimensional inversion of multitransmitter electromagnetic data based on the localized quasi-linear approximation," *Geophys. J. Int.* 148 (Mar. 2002): 506–519.

Zhdanov, M. S., and S. Fang, "Quasi-linear approximation in 3D EM modeling," *Geophysics* 61, no. 3 (Jun 1996): 646–665.

Zoughi, R. *Microwave Non-destructive Testing and Evaluation.* Dordrecht, The Netherlands: Kluwer Academic, 2000.